UNIVERSITA' DEGLI STUDI DI TRIESTE
Sede Amministrativa del Dottorato di Ricerca

XIX° CICLO DI DOTTORATO DI RICERCA

Dottorato di Ricerca in

NANOTECNOLOGIE

"Applications and limits of Raman spectroscopy in the study of colonic and pulmonary malformations"

Settore Scientifico-disciplinare: ING-IND 22

Dottoranda

Daniela Codrich

Coordinatore del Collegio dei Docenti

Chiar.mo Prof. M. Fermeglia

Università degli Studi di Trieste

Relatore

Chiar.mo Prof. V. Sergo

Università degli Studi di Trieste

Correlatore

Chiar.mo Prof. C. Krafft

University of Dresden

ANNO ACCADEMICO 2006-2007

“Applications and limits of Raman spectroscopy in the study of colonic and pulmonary malformations”

Summary

Chapter 1

Introduction and aim of the work

Presentation of the working centres, the ideas behind the project, the aim of the project, steps of the project and structure of the dissertation

1.1 Presentation of the working centres

The work presented in this dissertation originates from a collaboration between the Pediatric Surgery Department of the Hospital for Sick Children Burlo Garofolo of Trieste and the Department of Materials and Natural Resources of the University of Trieste.

1.2 The ideas behind the project

The idea behind the project was to bring together medical and basic sciences knowledge in order to apply a technology such as vibrational spectroscopy, which has mainly served for analytical chemistry and condensed matter physics, to an area of clinical relevance. Pediatric surgery's main concern is the respect of the growing organism in every situation where a surgical pathology requires an excision of a corporeal segment, therefore "sparing surgery" is the gold standard for every pediatric surgeon. This implies that a correct, complete and highly detailed diagnosis and localization of the disease is the premise to keep surgical resections to the minimum, avoiding unnecessary mutilations. Nowadays, imaging studies such as Ultrasound (US) scans, computed tomography (CT) scans and Magnetic Resonance Imaging (MRI) are used to identify and localize disease, however none of these diagnostic tools are able to yield fine chemical information on the pathology to be studied. Histology, with its conventional and immunohistochemical dyes is able to characterize disease, but of course it requires excision and preparation of samples, being widely unsuitable for in vivo studies. The interest toward Raman spectroscopy, which is based on inelastic scattering of photons, arises from the fact that this spectroscopic technique can provide details of the chemical composition and molecular structures of cells and tissues. In principle, disease and other pathological alterations lead to chemical and structural changes on the molecular level thus modifying also the vibrational spectra, which become a phenotypic marker of the disease. As these spectral changes are very specific and unique, they are also called fingerprint. The advantages of the method include that it is non-destructive and does not require extrinsic contrast-enhancing agents, therefore making it suitable for in vivo applications. When combined with the possibility of collecting multiple spectra over different points on a sample (motorized stages, optical fibers), this techniques offers the option of joining spatial and chemical information, therefore opening wide perspectives on its use in the clinical asset and even in the operatory theater, where precise recognition of resection margins in real time is the trouble of every surgeon.

1.3 Aim of the project

The aim of the work presented in this dissertation is to verify the feasibility of application of Raman vibrational spectroscopy for the study of human tissue, focusing on the chemical characterization of tissues affected by congenital malformations, in particular colonic and pulmonary malformations. As will be discussed later on in this dissertation, although many scientists are applying Raman spectroscopy for the study of neoplastic pathology, our group is the only one dealing with evaluation of congenital pathologies. The interest toward this kind of diseases is a peculiarity of our group since diagnostic workout, therapeutic management and long term follow up of congenital malformations is everyday job for the pediatric surgical members of the study group.

1.4 Steps of the project and structure of the dissertation

The project started with an initial phase of optimization of the spectroscopic equipment of the Department of Materials and Natural Resources at the University of Trieste, switching from an inorganic samples laboratory set up to an asset suitable for biological samples spectroscopic study. These changes have been done according to a review of the most recent literature on the use of Raman spectroscopy in biomedical science and will not be thoroughly reported in this dissertation: our final experimental set up will be presented in the "Experimental" section.

A review of the applications of Raman spectroscopy was done and will be reported in the "Background" section of this thesis, together with an insight of the congenital malformations studied, i.e. Hirschsprung's disease (HD), Congenital Cystic Adenomatoid Malformation (CCAM) of the lung and Bronchopulmonary Sequestration (BS). An overview of Raman spectroscopy fundamentals will be also present in the same chapter.

The second phase of the study focused on the characterization of samples of normal lung and colon tissues, whose chemical maps and average spectra will be presented and discussed in the "Results" section of the dissertation. The latter section will also report the results of the third phase of the study, during which samples from patients affected by CCAM and BS underwent Raman spectroscopic imaging. Mapping of samples of patients affected by HD is not yet completely worked out and only the normal colonic structure will be discussed. A dedicated chapter will deal with the comparison between Raman and Infrared imaging of colon and lung samples, as Infrared data have been kindly collected and granted by Prof. Christoph Krafft at Dresden Institute for Analytical Chemistry.

The last section will provide our conclusions over the feasibility and limits of Raman spectroscopy for the study of human congenital malformations.

Chapter 2

Background

Raman fundamentals, Hirschsprung's disease, Congenital Cystic Adenomatoid Malformations of the lung, Bronchopulmonary Sequestrations, state of the art of Raman spectroscopy in biomedical science

2.1 *What is Raman spectroscopy?*

Raman spectroscopy is a spectroscopic technique used in condensed matter physics and chemistry to study vibrational, rotational, and other low-frequency modes in a system. It relies on inelastic scattering, called Raman scattering, of monochromatic light after its interaction with matter.

2.2. Historical recalls

Before addressing the scientific background of this technique, a brief historical recall seems appropriate.

Although the inelastic scattering of light was predicted by Smekal in 1923, it was not until 1928 that it was observed in practice. The Raman effect was named after one of its discoverers, the Indian scientist Sir Chandrasekhra V. Raman who observed the effect by means of sunlight in 1928, together with K. S. Krishnan and independently by Grigory Landsberg and Leonid Mandelstam.(1) Raman awarded the Nobel Prize in Physics in 1930 for this discovery accomplished using sunlight, a narrow band photographic filter to create monochromatic light and a "crossed" filter to block this monochromatic light. He found that light of changed frequency passed through the "crossed" filter. Gradually, improvements in the various components of Raman instrumentation took place. Early research was focused on implementation of excitation sources and after trials with helium, lead, zinc lamps, in the 1930's the mercury arc (the Toronto arc) became the principal light source. From 1962 laser lights were introduced for Raman spectroscopy. Eventually, the Argon ion (351.1-514.5 nm) and the Krypton ion (337.4-676.4nm) lasers became available and more recently the Nd-YAG laser (1064 nm) has been used for Raman spectroscopy. Developments in the optical train of Raman instrumentation started with the use of a single monochromator, proceeding with the use of double monochromators and triple monochromators. In 1968 holographic gratings appeared, adding efficiency in collection of Raman scattering to the commercial Raman instruments. Progress occurred in the detection systems for Raman measurements, starting with photographic detection and then moving forward the development of photoelectric Raman instrumentation after World War II. In 1953, a photomultiplier tube, which converts the entering photons into an electric signal was introduced and in recent years, charge-coupled devices (CCDs) have been used increasingly in Raman spectroscopy as detectors. Nowadays Raman spectra can be obtained also by Fourier transformed spectroscopy.(2)

2.3 Basic Raman theory

When a laser is used to probe a sample, light impinges upon a molecule and interacts with the electron cloud of the bonds of that molecule. When light is scattered from a molecule most photons are elastically scattered (Rayleigh scatter), meaning that the scattered photons have the same energy (frequency) and, therefore, wavelength, as the incident photons and no change in the molecular status of the molecule is observed. However, a small fraction of light (approximately 1 in 10^7 photons) is scattered at optical frequencies different from, and usually lower than, the frequency of the incident photons. The process leading to this inelastic scatter is the termed the Raman effect. In quantum mechanics the scattering is described as an excitation to a virtual state lower in energy than a real electronic transition with nearly coincident de-excitation and a change in vibrational energy. The scattering event occurs in 10^{-14} seconds or less. The difference in the energy level between the excited and ground level are shown in fig.1. At room temperature the thermal population of vibrational excited states is low, although not zero. Therefore, the initial state is the ground state, and the scattered photon will have lower energy (longer wavelength) than the exciting photon. Since more photons undergo Stokes scatter, this Stokes shift is what is usually observed in Raman spectroscopy.

Fig.1

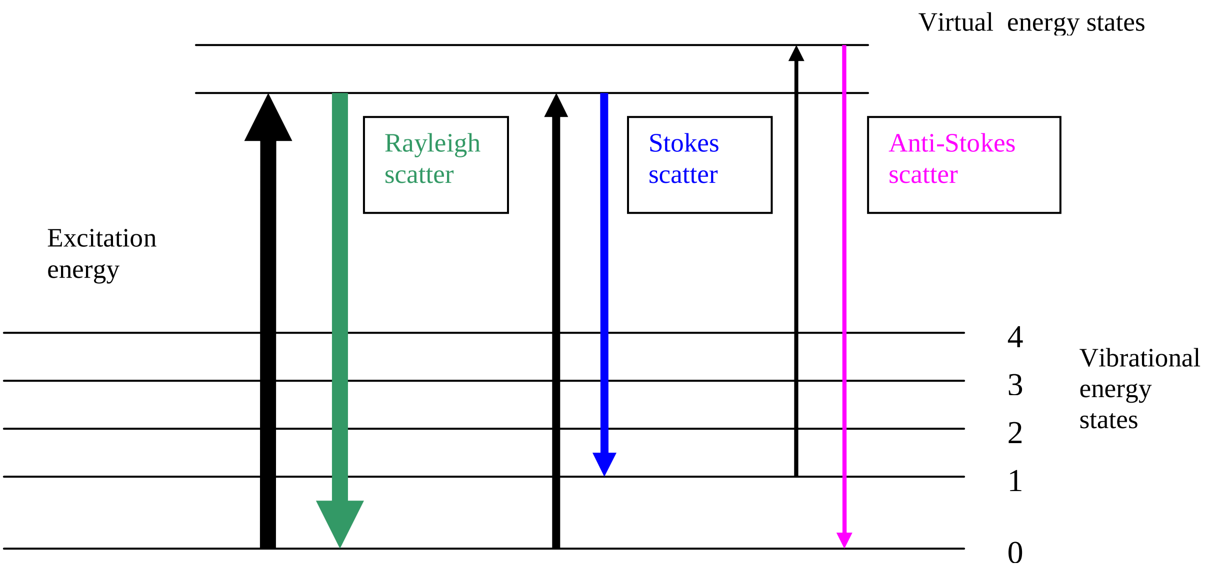

According to the law of conservation of energy, the change in energy between the incident photon (hv_0) and the scattered photon (hv_s) corresponds to the energy change of the molecule, which refers to the transition between two vibrational states, the initial (hv_i) and the final excited state (hv_f) according to the equation:

$$h\nu_0 - h\nu_s = h\nu_f - h\nu_i \quad \textbf{(1)}$$

where h is the constant of Planck and v is the frequency of the electromagnetic wave. Therefore the change in the vibrational status of the molecule (ΔE_{f-i}) can be expressed as:

$$\Delta E_{f-i} = h(\nu_o - \nu_s) \quad \textbf{(2)}$$

If in (2) we substitute the definition of frequency with the number of waves in the distance light travels in one second, where c is the velocity of light and λ is the wavelenght of the radiation, we find that

$$\Delta E_{f-i} = h\left(\frac{c}{\lambda o} - \frac{c}{\lambda s}\right) \quad \textbf{(3)}$$

and since c is constant and h is constant, the change in the difference of energy can be expressed in terms of the *reciprocal of the wavelenght*, whose dimension is cm^{-1}, and it is denominated the *wavenumber*. This is the normal unit used both in Raman and Infrared spectroscopy.

If we want to study the Raman scattering in Δ classical terms, the interaction between the electromagnetic radiation and the sample can be viewed as a perturbation of the molecule’s electric field. A simple classical electromagnetic field description of Raman spectroscopy can be used to explain many of the important features of Raman band intensities. The dipole moment, P, induced in a molecule by an external electric field, E, is proportional to the field as shown in equation 4.

$$P = \alpha E \quad \textbf{(4)}$$

The proportionality constant α is the polarizability of the molecule. The polarizability measures the ease with which the electron cloud around a molecule can be distorted.

If we substitute the equation which describes the normal fluctuation with time (t) of the electromagnetic field of the electromagnetic wave (the laser beam), where E_0 is the vibrational amplitude and v_0 is the frequency of the laser , we obtain

$$P = \alpha E = \alpha E_o \cos 2\pi v_0 t \qquad \textbf{(5)}$$

When a diatomic molecule vibrates at a frequency v_m, assuming a simple harmonic motion, its internuclear distance (q) can be written in the form:

$$q = q_o \cos 2\pi v_m t \qquad \textbf{(6)}$$

where q_0 is the amplitude of vibration. The polarizability, which in this case is a scalar quantity, can be expanded as a Taylor series as a linear function of q

$$\alpha = \alpha_0 + \left(\frac{d\alpha}{dq}\right)_0 q_0 + \ldots \qquad \textbf{(7)}$$

where α_0 is the polarizability at the equilibrium position and $(d\alpha/dq)_0$ is the rate of change of α with respect to the change in q. Combining (5) and (6) and (7), we obtain

$$P = \alpha E_0 \cos 2\pi v_0 t$$

$$= \alpha_0 E_0 \cos 2\pi v_0 t + \left(\frac{d\alpha}{dq}\right)_0 q E_0 \cos 2\pi v_0 t$$

$$= \alpha_0 E_0 \cos 2\pi\nu_0 + \left(\frac{d\alpha}{dq}\right)_0 q_0 E_0 \cos 2\pi\nu_0 t \cos 2\pi\nu_m t$$

$$= \alpha_0 E_0 \cos 2\pi\nu_0 t + \frac{1}{2}\left(\frac{d\alpha}{dq}\right)_0 q_0 E_0 \{\cos[2\pi(\nu_0 + \nu_m)t\ ] + \cos[2\pi(\nu_0 - \nu_m)\ ]\ \} \qquad \textbf{(8)}$$

The first term of equation (8) represents an oscillating dipole that radiates light of frequency v_0 (Rayleigh scatter), that is the same of the incident laser, while the second term correspond to the Raman scattering of frequency v_0+v_m (anti-Stokes) and v_0-v_m (Stokes), as shown in Fig.1. It is important to note that the second term of the equation contains the factor $(d\alpha/dq)_0$, which, if zero, yields no Raman scattering. Therefore, the selection rule for a molecule to be Raman active is that the rate of change in polarizability with vibration must non be zero. If a vibration does not greatly change the polarizability of the molecule, then the polarizability derivative will be near zero, and the intensity of the Raman band will be low. The vibrations of a highly polar moiety, such as the O-H bond, are usually weak. An external electric field can not induce a large change in the dipole moment and stretching or bending the bond does not change this. For this reason, water is only weakly Raman active and therefore does not interfere with Raman spectroscopy of biological samples.

Typical strong Raman scatterers are moieties with distributed electron clouds, such as carbon-carbon double bonds. The pi-electron cloud of the double bond is easily distorted in an external electric field. Bending or stretching the bond changes the distribution of electron density substantially, and causes a large change in induced dipole moment [2,3].

2.4 Raman instrumentation: major components

Commercially available Raman spectrometers consists of four major components:

1. Excitation source, usually a laser
2. Sample illumination and collection system
3. Wavelength selectors

4. Detection and computer control system.

Lasers became the excitation source in Raman instrumentation set-ups after the 1960s. The main advantages of using lasers are that their beams are highly monochromatic, usually with a small diameter that can be further reduced by using lens systems and thus focused on small samples (~ 1 mm^3), which in case of Raman microscopy can be regions as small as 2 µm in diameter. Different kinds of lasers are available: gas lasers such as Ar^+, Kr^+, He-Ne or solid state lasers such as Neodymiun -YAG, the latter having its primary lasing wavelength at 1064nm which is especially suitable for FT-Raman system operating in the infrared region. Diode lasers can be obtained at specific wavelength in the blue or the infrared regions. Other devices such as dye lasers, excimer and nitrogen laser have been used for Raman spectroscopy.

Since Raman scattering is weak, the laser beam must be properly focused onto the sample and the scatter radiation collected efficiently. In principle, excitation and collection from the sample can be accomplished in any geometry. More frequently, the 90° or the 180° (the back scattered) configuration are used, the latter being the one depicted in Fig.2 and used in our instrument.

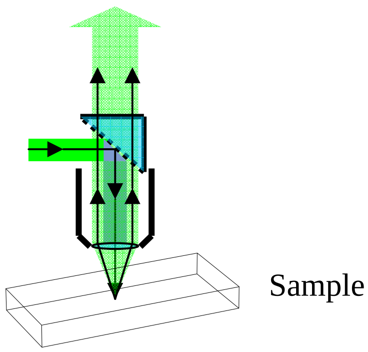

Fig.2

Wavelenght selectors can be classified in different categories, the simplest one being the dichroitic filter. Prisms, grating monochromators and spectrographs have been used in Raman instrumentation. Coupling of two or three monochromators put in series was developed to reduce stray or extraneous light that can overlap the weak Raman light. Recently holographic notch filters (filters that pass all frequencies except those in a stop band centred on a selected frequency) have been used to suppress the Rayleigh light, before grating diffraction.

Early on, detection of Raman light was done with photographic films, using long time exposures. Subsequently, in Raman spectrometer equipped with monochromators, the light exiting through the slits was focused onto a photomultiplier tube, which converts photons into an electrical signal. In the former Raman spectrometers, the detection of the Raman signal was done for each frequency, but this time consuming single-channel technique was substituted by multiple channel detection and recently by Charge-Coupled Devices (CCDs) which are silicon-based semiconductors arranged as an array of photosensitive elements, each one generating photoelectrons and storing them as an electrical charge. Charges are stored on each individual pixel as a function of the number of photons striking that pixel and then read by an analogue-to-digital converter.

A schematic representation of a modern Raman spectrometer is shown in Fig.3 and can be assimilated to the instrumentation used in our laboratory setting [(2)].

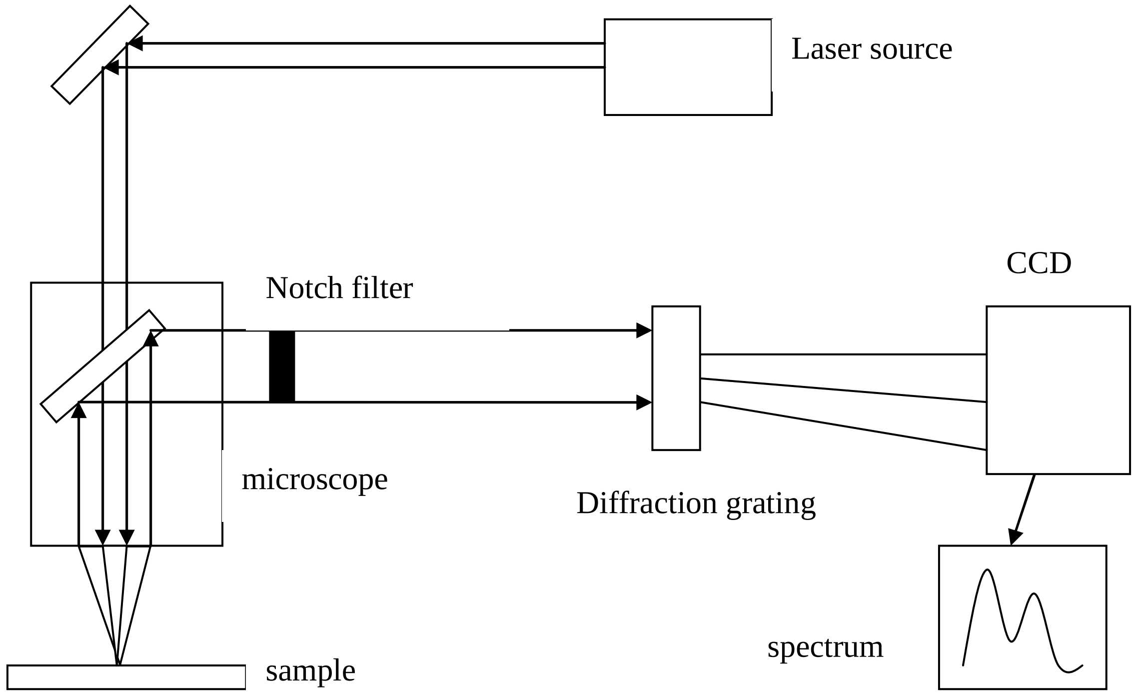

Fig. 3

2.5 What is Hirschsprung's disease (HD)?

This disease is named for Harald Hirschsprung, the Danish physician who first reported the disease in 1886, describing two infants who had died with swollen bellies.

HD results from the absence of parasympathetic ganglion cells in the myenteric and submucosal plexus of the rectum and/or colon. Ganglion cells, which are derived from the neural crest, migrate caudally with the vagal nerve fibres along the intestine. These ganglion cells arrive in the proximal colon by 8 weeks of gestational age and in the rectum by 12 weeks of gestational age. Arrest in migration, or a failure in survival of the neural cells leads to an aganglionic segment. This results in clinical HD. Aganglionosis therefore begins at the anus, which is always involved, and continues proximally for a variable distance. Normal colonic motility is primarily under the control of intrinsic neurons. Bowel function remains adequate, despite a loss of extrinsic innervation. These ganglia control both contraction and relaxation of smooth muscle, with relaxation predominating. Extrinsic control is mainly through the cholinergic and adrenergic fibres. The cholinergic fibres cause contraction, and the adrenergic fibres mainly cause inhibition. In patients affected by HD, the absence of ganglion cells leads to a marked increase in extrinsic intestinal innervation. The innervation of both the cholinergic and adrenergic systems is 2-3 times that of normal innervation. The adrenergic (excitatory) system is thought to predominate over the cholinergic (inhibitory) system, leading to an increase in smooth muscle tone. With the loss of the intrinsic enteric inhibitory nerves, the increased tone is unopposed and leads to an imbalance of smooth muscle contractility, uncoordinated peristalsis, and a functional obstruction(4). Other cellular elements, the interstitial cells of Cajal, which are pacemakers cells generating slow waves and facilitating active propagation of electrical events and neurotransmission through the intestinal wall, are less represented and have an altered distribution in HD (5). Fig.4 shows a schema of the normal anatomy of colonic wall, with its submucosal and myenteric plexi, named respectively Meissner's plexus and Auerbach' plexus

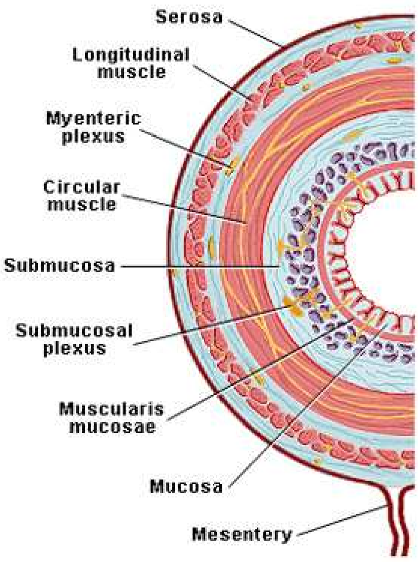

Fig. 4: Scheme of the multi-layers structure of colon.(Picture from www.lib.mcg.edu)

Histological appearance of the plexi are shown in Fig.5

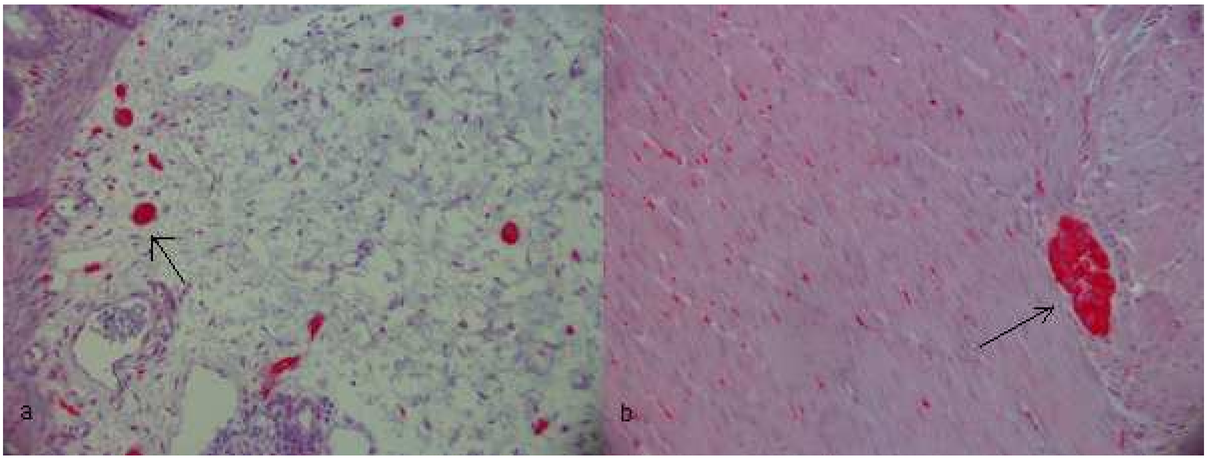

Fig. 5 *: Immunohistochemical staining for NSE (Neuron Specific Enolase). Red spots evidence gangliar structures in the submucosal (Meissner's)plexus (a) and in the myenteric (Auerbach's) plexus (b).* (*Picture from the archives of University of Trieste Institute of Pathology).*

Estimated incidence of the pathology is 1:5000 newborns. Diagnosis is based on clinical findings, plain abdominal X-ray and contrast enema, showing a narrowed distal colon with proximal dilation of the non affected bowel. However, findings in neonates (i.e. babies aged <1 month) are difficult to interpret and will fail to demonstrate this transition zone approximately 25% of the time. Anorectal manometry detects the relaxation reflex of the internal sphincter after distension of the rectal lumen. This normal inhibitory reflex is thought to be absent in patients with HD. However, the gold standard for the diagnosis is the histological diagnosis on rectal suction biopsies, where hypertrophy of cholinergic nervous fibres throughout the lamina propria and muscularis propria is demonstrated with the use of acetylcholinesterase staining, as shown in Fig.6. This histological finding, associated with the absence of ganglia in the myenteric and submucosal plexi on full thickness biopsies, confirms the diagnosis of HD [6].

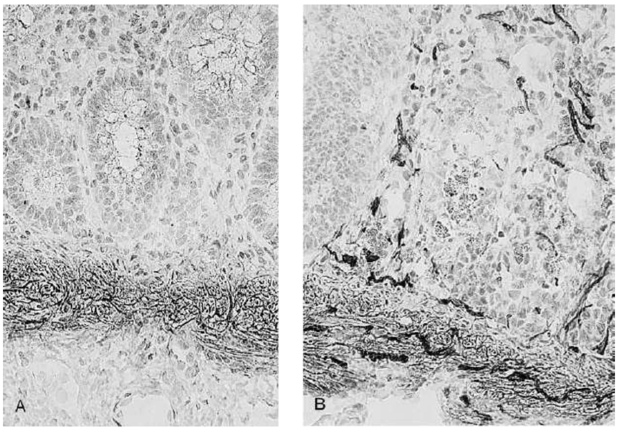

Fig. 6 *Achetylcholinesterase staining. A: normal colon, showing thin threads network in the muscularis mucosae and no hypertrophy of nerve bundles in the lamina propria. B: Increased acetylcholinesterase stained nerve twigs in muscularis mucosae and lamina propria in HD patient.*[6]

As Moore and Johnson pointed out, a peculiar feature of HD is that a particular isoform of Acetylcholinesterase is over expressed, the G4 (AchE-G4). This isoform consists of a tetramer (four catalytic units) linked to a hydrophobic protein and seems to be expressed in the embryo especially during migration of neural crest cells [7].

The goals of surgical treatment of HD are to remove the aganglionic bowel and reconstruct the intestinal tract by bringing the normally innervated intestine to the anus, while preserving sphincter function. Reliable intraoperative biopsies to evaluate aganglionosis extension are crucial for good surgical results, since one of the causes of persistence of obstructive symptoms after a pull-through operation is retention of an aganglionic segment, due to imprecise pathological evaluation. This will require the child to undergo a second surgical resection [4,6].

2.6 What are Bronchopulmonary Sequestrations (BS) and Congenital Cystic Adenomatoid Malformations (CCAM)?

A broad spectrum of bronchopulmonary malformations may arise during the development of the lungs. As their presentation may be life threatening and may require urgent surgical intervention, their clinical recognition is of crucial importance.

Lungs start their development in the third week of gestation as a ventral out pouching of the primitive gut. From 26th days to 6th weeks of gestation, 2 lung buds give rise to 5 lobar bronchi that develop associate with their arteries and veins. From the 6th to the 16th weeks, development of the conducting airways begins, while the acini, the basic structure of gas exchanges, form from the 16th to the 28th week. The distal air spaces continue to multiply until birth, while the alveolar differentiation keeps going on after birth until two years of age: after this period lung growth occurs more in terms of volume and alveolar size, rather than formation of new gas exchanging units, continuing up to 8 years. The final surface area for ventilation increases from 3-4 m^2 in the neonate, to 75m^2 in the adult. Multiple publications suggest a common embryological pathogenesis of pulmonary malformations, since different types of lesion may coexist in the same patient [8].

Bronchopulmonary Sequestrations

They are defined as a portion of the lung isolated from the rest of the lung, non functioning, without any continuity with the upper tracheo-bronchial tree and with an independent vascularisation arising directly from the aorta rather than a pulmonary artery. BS are further divided into Extralobar sequestrations (ELS) and Intralobar sequestrations (ILS) [8]. ELS is an isolated mass of pulmonary tissue with its own pleural investment, separate from the normal lung. Its common location is the thoracic cavity, usually below the normally formed lung, more frequently in the left hemithorax, but it can be found anywhere from the neck to below the diaphragm and they often receive vascularisation from the thoracic descending aorta [9]. It is supposed that this develops when independent collections of cells with respiratory potential arise from the primitive foregut caudal to the normal bud lung. ELS usually show parenchymal maldevelopment, with about half having microcystic maldevelopment as in small cystic Stocker type 2 CCAM, as will be later on explained in this chapter [9]. ILS differ from ELS in that they rest within a lobe of normal parenchyma, usually the lower lobes, and that they have not their own pleural investment. The arterial supply arises from systemic circulation but, unlike the ELS which drain 80% of the times toward the azygous or hemiazygous system, the venous drainage is uniformly via the pulmonary veins [8].

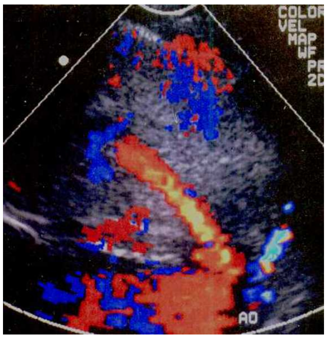

Fig.7: Doppler Ultra Sound (US) of an ELS. The red transverse image represents the aberrant vessel arising from the aorta.(Picture from www.emedicine.com)

Congenital Cystic Adenomatoid Malformations

They are usually considered as hamartomatous lesions of the bronchial tree. It is hypothesised that they are due to a derangement of the alveolar phase of lung development, when an abnormal signalling between the developing terminal bronchioles and the alveolar mesenchyma results in an uncontrolled overgrowth of the terminal bronchioles. Because some types are not cystic and only one type has the adenomatoid appearance, the term "Congenital Pulmonary Airway Malformations" (CPAM) has been introduced [10]. In 1977, these lesions have been classified into 3 forms by Stocker, who later on added two other rarer classes. Type 0, or acinar dysplasia, is an extremely rare form, incompatible with life. Type 1 (or macrocystic type) is the commonest form and is composed of cyst that range in size from 1 to 10 cm. Type 2 (microcystic type) lesions consists of multiple small cysts, usually less than 1 cm in diameter which microscopically appear as dilated bronchioles separated by normal alveoli. This type of lesions may be present in up to 50% of ELS. Type 3 (solid type) lesions are rare (8-10%) and have a bulky appearance, with thin walled cysts of few millimetres. They are airless masses of bronchiolar elements, lined by patchy ciliated cuboidal epithelium mixed with alveolar elements. Some describe Type IV as a large cystic lesion in the periphery of the lung, believed to be of acinar origin. Others do not describe this subtype and incorporate it into the others. These cysts are lined by flattened pneumocytes (11). CCAMs are usually unilateral and involve only one lobe of the lung. They are detected in chest and CT scan images as abnormal air, air/fluid-filled cysts, or fluid-filled/solid-appearing cysts, and large masses may cause mediastinal shift.

In recent years, both BS and CCAM are more frequently diagnosed by routine prenatal ultrasound examination. Usually, fetuses with lung malformations are closely monitored during pregnancy because of variable fetal course of these entities. This is true in particular for cystic lesions which can enlarge until fetal hydrops may develop or they can shrink toward the end of the pregnancy (10,12). All prenatally detected congenitally lung malformations require clinical and radiological evaluation. Some patients may present at birth with severe respiratory distress and mediastinal shift, so that urgent lobectomy or atypical lung resection can be required. Asymptomatic cases can be studied by CT scans in the first few months of life (10). Controversies in literature are still going on over the management of these asymptomatic cases: surgical removal is generally recommended even in absence of respiratory symptoms to avoid future infective episodes and possible development of neoplastic pathologies such as pneumoblastoma(10,12,13). In the light of the already described phases of lung development, early surgical resection within the first year of age can maximize compensatory growth of the residual pulmonary parenchyma (10,12,13). One of the problems of early surgery is that macroscopic gross recognition of the lesions, especially in the case of CCAMs, may be difficult and sparing surgery can be a challenging surgical issue.

2.7 The state of the art of Raman spectroscopy in biomedical science, with a focus on lung and colon investigations

Although the Raman effect was first observed in 1928, it was not until the early 1990s that Raman spectroscopy was applied in the successful analysis of living cells and tissues. In recent years there has been a remarkable increase in the application of this vibrational spectroscopy to the field of medicine. As disease leads to changes in the molecular composition of affected tissues, these changes should be reflected in the spectra. Furthermore, if the spectral changes are specific enough for a particular disease state, they can, in principle, be used as phenotypic markers of the disease [(14)]. There are several key advantages of Raman spectroscopy over other analytical techniques for studying living systems: it is non invasive and non destructive (no fixation or no probe-containing antibodies are required), spectra can be collected in few minutes and automated chemical analysis can be performed. Moreover, in Raman spectroscopy, water does not affect the relevant area of the spectrum, allowing living cells and tissues to be analyzed in near-physiological conditions [(15)]. This potential for in vivo application and its ability to therefore direct real-time therapeutic intervention give Raman spectroscopy its great appeal for basic and clinical research. In vivo diagnostic tools are much needed in many fields of medicine to take the sometimes unavoidable guesswork out of current clinical procedures, to avoid long delays caused by ex vivo evaluation of patient material, or to simply replace current invasive methods by noninvasive or less invasive techniques [(14)]. An early obstacle encountered in the biomedical application of Raman spectroscopy was tissue fluorescence and the lack of appropriate, sensitive instrumentation. The problem of fluorescence, which overwhelms the Raman signal of most natural biological samples including tissue upon excitation in the visible region, has been largely overcome by the availability of instruments working in the NIR region of the spectrum [14-16]. Early reports in the literature regarding the utility of Raman spectroscopy to biomedical problems were based on macroscopic acquisition of spectra at single points which required an a priori knowledge of the location or a pre-selection of the probed position. Since the inhomogeneous nature of tissue were not considered in these early studies, an accurate correlation between the histopathology of the sampled area and the corresponding spectra was not possible. In the past ten years high throughput and more sensitive instruments became available for Raman microspectroscopic imaging. They enable to microscopically collect larger number of spectra from larger sample populations in less time improving statistical significance and spatial specificity. Simultaneously, fiber-optical probes have been developed for in vivo applications [16]. The two main problems in applying fiber optics in Raman spectroscopy were the large signal background due to the Raman signal generated in the fiber materials itself and poor signal collection efficiency. To resolve these problems, filtering of the laser light and scattered light was made in the probe tip. Thus, these probes consisted of one central excitation fiber, six surrounding collection fibers, internal “in-the-tip” filters and beveled fiber ends for optimized light collecting efficiency. Unfortunately, the production of these probes has stopped. Other filtered probes are commercially available (InPhotonics Inc. Norwood, MA) but their dimensions are too large for many clinical applications, particularly endoscopy. To overcome the problem of the optical system’s Raman signal interference with the tissue Raman signal, Koljenovic et al. proposed in 2005 to use miniaturized unfiltered probes and to collect spectra in the high wavenumber region (2400-3800 cm^{-1}), where there is almost no contribution of the optical system and where tissue spectra yield as much information as they would in the conventional 600-2000 cm^{-1} fingerprint region [17]. Few paper report the use of dedicated fiber optics to collect in vivo Raman spectra of tissues of the gastrointestinal tract through the working channel of an endoscope or spectra of the wall of blood vessels [17-20]. For the purpose of this dissertation, only the most recent literature concerning studies on intestinal and pulmonary tissues will be reviewed.

2.7.1 Colon

The most studied pathologies of the colon are neoplastic diseases: the benign adenomas and malignant adenocarcinomas. Raman spectroscopy is not the only suggested technique to realize an optical biopsy device, suitable to be use in vivo during endoscopical procedures in the gastrointestinal tract: fluorescence endoscopy, optical coherent tomography, confocal microendoscopy, light-scattering spectroscopy, IR spectroscopy have all been tested [21]. Thin sections of normal and malignant colon tissue have been mapped by IR microspectroscopy, without the use of fiber optic devices [22], however no microscopic mapping of normal colon has been done by Raman spectroscopy but in our present dissertation. Normal colon has been studied by Andrade and coworkers in 2007 but only 144 single point spectra were acquired and submitted to statistical evaluation, without mapping [23]. The feasibility of fiber-optic coupled Raman spectroscopy for disease classification was demonstrated during in vivo clinical gastrointestinal endoscopy by Shim in 2000 [24]. The fiber-optic probe was passed through the endoscope instrument channel, placed in contact with the tissue surface and spectra could be obtained in 5 sec. The same group also differentiated adenomatous from hyperplastic polyps in the colon using the same fiber-optic Raman system three years later [25]. Stone reported in 2004 a 92% sensitivity and 93% specificity for single random-sampled Raman spectra collected from ex vivo colorectal biopsies to distinguish between normal and malignant tissue [26].

2.7.2 Lung

Huang studied 28 specimens of non fixed bronchial specimens by Raman spectroscopy in 2003 using a spectrometer with 785 nm excitation coupled to a fiber-optic probe which was developed earlier for skin studies. Raman spectra were collected with 5 sec exposure time and the spectral differences between normal and tumor tissues were analyzed. They found that malignancies seemed to be associated with an increased percentage amount of protein and a decreased percentage amount of phospholipids over the total amount of Raman active components [27]. In the same year, Yamazaki collected 210 spectra from cancerous and non cancerous lung tissue with a Raman spectrometer emitting at 1064 nm and was able to predict malignancy with a sensitivity of 91% and a specificity of 97% [28]. Koljenovic studied frozen sections of normal bronchial tissue by Raman imaging: subsequent comparison of Raman images with histological evaluation of stained sections enabled to identify the spectral features of bronchial mucus, epithelium, fibrocollagenous stroma, smooth muscle, glandular tissue and cartilage [29]. However, neither mapping of the normal lung parenchyma can be found up to now in literature, nor experimental work on lung malformations has been ever tried before this thesis.

Chapter 3
Methods

Collection of samples and their preparation, the instrumentation, acquisition of spectra and maps, data processing

3.1 Collection of samples

Specimens were collected during surgical intervention in the operating rooms at the Surgical Department of Burlo Garofolo’s Children Hospital. Prior to operations, parents were informed on our study and their permission to reserve some of the resected tissue for spectroscopic studies was obtained. The remainder of the tissue was sent as usual for normal histopathological examination.

Sample of normal colon was collected during closure of a colostomy from normally appearing and functioning descending colon in a 4 months old boy operated on for anorectal malformation. Previous samples used to optimize spectrometer’s performances on biological sample were collected from appendectomies performed during correction of malrotations and therefore without inflammatory changes.

As far as lung samples are concerned, the single healthy sample which will be presented and separately discussed in the first part of the lung results, was collected from a 4 days old child who was urgently operated on for respiratory distress due to extended CCAM of the upper and middle right lobe and the specimen represent a small fragment of the healthy lower lobe. The specimens discussed in the CCAM section of the results, came from the macroscopically healthy and macroscopically affected lung parenchyma removed during lobectomies of two infants affected by CCAM. Both CCAM specimens were of the solid type 3 malformation. Samples were obtained from other two patients affected by bronchopulmonary sequestrations. In the first case the patient was a 1 year old infant affected by an Intralobar Sequestration and we obtained a sample from the resection margin which was macroscopically free from disease and a sample from the lesion. The second patient was an 11 years old boy, affected by an Intralobar Sequestration which involved the whole right lower lobe and it was not possible to obtain a healthy specimen for comparison.

3.2 Sample preparation

Samples of about 0.5-1 cm^3 were collected and snap frozen in liquid nitrogen and stored at -80° until further use. No fixation was used. The reminder of the tissue was fixed in formalin for conventional histopathology. There are discussions in literature concerning the best handling of ex vivo samples. Formalin fixation preserves tissue by preventing autolysis and stabilizing tissue structure but, on the other hand, fresh ex vivo tissues are ideal as they are the best way for simulating in vivo conditions. However, this often causes major constraints in sample harvesting and handling because of paucity and rapid decay of samples, while formalin-fixed and formalin-fixed-paraffin-embedded specimens are abundant and more stable with time. In 2005 Krishna evaluated samples of ovarian tissue submitted to formalin fixation, formalin fixation + paraffin embedding, formalin fixation + paraffin embedding + deparaffinization and found that the best sample for discrimination of malignant and normal ovarian tissue were the formalin fixed ones [(30)]. However, no fresh samples were analyzed as controls in the study. The same group confirmed the suitability of formalin fixed sample to discriminate between malignant and normal cervix tissue, but, again, non-fixed control samples were not evaluated [(31)]. However, when Huang compared formalin fixed versus fresh malignant and benign bronchial tissue, he observed several formalin Raman peaks or shoulders at 907, 1041 and 1492 cm^{-1} in the fixed but not in the fresh tissue. Moreover, tissue Raman intensities in the 1500-1650 cm^{-1} region as well as intensities in the protein and lipid bands at 1302, 1335, 1445 and 1655 cm^{-1} were reduced in the fixed samples spectra: this finding suggests that any diagnostic algorithm in these regions could not be applicable for in vivo diagnosis [(32)]. Since we were particularly interested in the evaluation of bronchopulmonary tissue in this thesis and we believe that the ultimate goal of Raman spectroscopic diagnostic potential should be its application in vivo, we decided not to use formalin-fixed samples. For the sake of uniform evaluations, also colon samples were not fixed.

At the time programmed for Raman spectroscopy, samples were slowly acclimatized to the optimum cutting temperature for our cryotome which was around -14 °C and 20 µm thick sections of tissue were cut and transferred on slides, where the samples passively dried and no further preparation was performed. Using near infrared (NIR) light at 785 nm for excitation, CaF_2 or BaF_2 slides have a particular low background and they allow also IR spectroscopy [(16)]. The choice of these supports for Raman samples is that Raman signal of glass in standard quality is so intense that it covers completely the fingerprint region of tissue. Fig.8A and 8B show the spectra from a glass slide and a CaF_2 slide compared to the normal spectra of the muscular layer of colon.

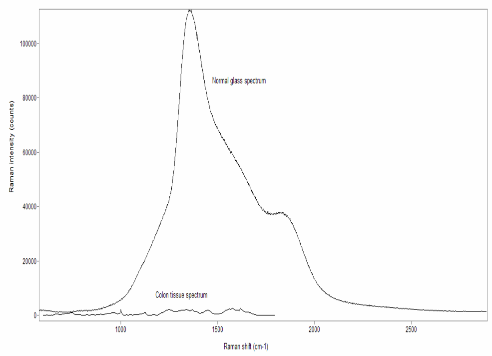

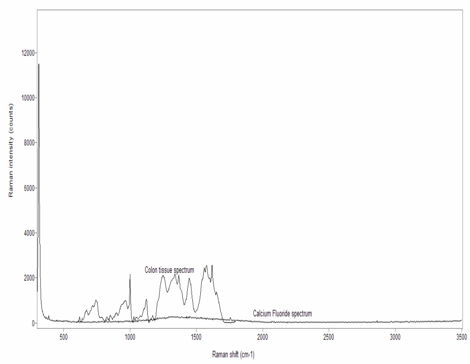

Fig. 8A Fig. 8B

Fig 8A: The Raman spectrum from a normal glass slide shows broad bands in the fingerprint region (600-1800 cm^{-1}) that cover the normal spectrum from a tissue sample. Fig. 8B: The spectrum from a CaF_2 slide has an intense, sharp band around 320 cm^{-1} but it does not *interfere with the tissue signal in the fingerprint region.*

3.3 Instrumentation

The Raman spectrometer we used is a Ranishaw In Via system (Renishaw plc, Wotton-under-Edge, UK) which is coupled with a Leica DMLM microscope (Leica Microsystems Gmbh, Wetzlar, Germany). The microscope is equipped with objectives of low-magnification (1.6x/NA 0.05) or higher-magnification (20x/N.A. 0.5) and a digital camera accessory, which was used to take pictures of unstained native sections. The excitation source is a 785 nm emitting diode laser, which was focused on samples with an average power of 25 mW using different objectives: usually 50x/N.A.0.75 or 100x/N.A.0.85. The different experimental settings will be explained individually for each sample in the results section. A holographic notch filter rejects the Rayleigh scattering; a single-grating spectrograph with a 1200 lines/mm grating is used for dispersing the useful radiation and a Renishaw RenCam thermoelectrically cooled charge coupled device (CCD) camera is used for the final photons/electrons conversion.

3.4 Acquisition of spectra and maps

For acquisition of Raman maps, samples were moved by a ProScan^{TM}II motorized stage (Prior Ltd., Cambridge, UK) coupled to the microscope in order to sequentially illuminate with the laser a grid of points and subsequently collect a Raman spectrum for each point. The step size of the grid was varied for each map acquisition, according to the dimensions of the studied sample and the objective used.

Spectra were collected in the reflection mode, with a 180° back scattering configuration. We usually collected the spectra in the fingerprint region, that is from 600 to 1800 cm^{-1}, using the synchro mode of the instrument software WiRE™ 2.0 (Renishaw). In the synchro mode, the grating with 1200 lines per mm is continuously moved to obtain Raman spectra of extended spectral regions at a spectral resolution of 4 cm^{-1}. Collection of each spectrum took on an average of 36 seconds. According to the dimensions of the sample studied, entire map collection took 10-16 hours. Before acquisition, the instrumentation was calibrated using the well documented Raman bands of 4-acetamidophenol.

3.5 Data processing

The data sets of the acquired spectra and maps were imported for processing in the software package Cytospec [(33)] or in a in-house developed program, built under a Matlab platform (The Mathworks Inc., USA). The Cytospec software, written in 2000 as a specialized software package for Fourier transform infrared (FT-IR) spectroscopic imaging, was subsequently developed to be applied on the whole area of vibrational spectroscopic (IR- and Raman) imaging. It differs from other software products available from instrument manufacturers in that it is designed and written to operate on entire spectral data sets, rather than individual spectra: it permits to perform the standard spectral manipulations found in single spectra analysis software, such as expansion, smoothing, scaling, normalization, etc on the whole data set, thus all operations carried out on the data affect every spectrum, with the number of spectra in the data set limited by the available memory. Due to the fact that data sets often contain hundreds or thousands of spectra, a number of statistical approaches to the data are built in the software. These can be classified as uni- and multivariate statistical methods. Univariate methods of analysis, included in the software, consist of various mapping displays of hyperspectral data. In these, the user may select band intensities, integrated intensities, intensity ratios, etc., to construct false colour maps of the spectral data, which may be considered to be slices through the hyperspectral data cube. The multivariate methods of data analysis create spectral correlations and maps by including not just one intensity or frequency point of a spectrum, but by utilizing the entire spectral information. These methods include Principal Component Analysis (PCA), and different methods of Cluster Analysis (hierarchical cluster analysis, fuzzy c-means cluster analysis and k-means cluster analysis).

The Cytospec software was used to import and partially pre process data, while the in-house MathLab developed routines were mainly used for completing preprocessing and multivariate analysis application.

Spectral variances due to elastic light scattering were reduced by subtracting a multi-point baseline from each spectrum, with minima points set at 600, 1020, 1190, 1720 and 1800 cm^{-1}.

Cosmic spikes, which are high and narrow bands generated by high energy particles hitting accidentally the CCD detector, were detected in the data set and corrected by an average value of three preceding data points. As cosmic spikes are generally narrow, the correction procedure changed the spectral information only marginally. This correction was done either using a in house made MathLab subroutine, or a cosmic ray correction procedure available in Cytospec as well.

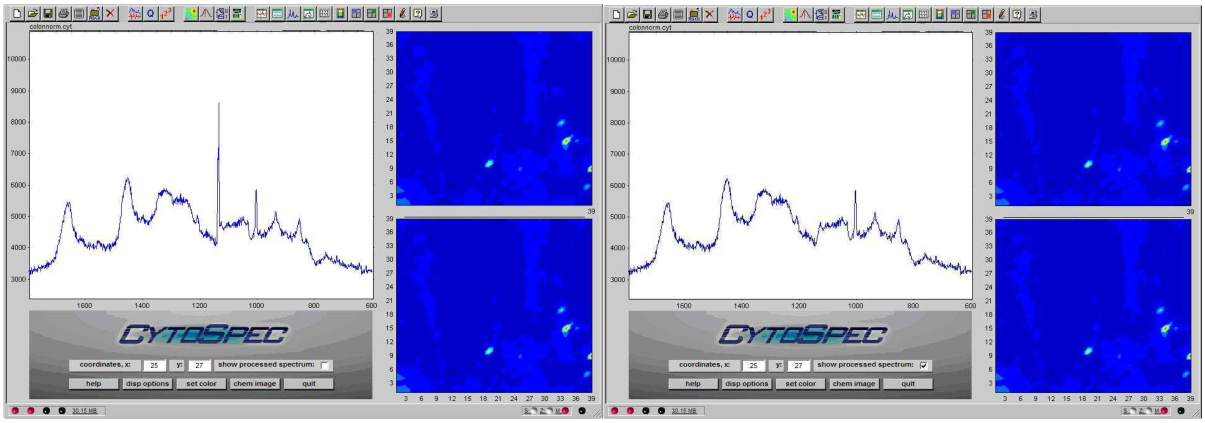

Fig. 9: A spectrum taken from the data set of a colon Raman map, shows the typical appearance of a cosmic ray artifact (on the left) and the same spectrum after the cosmic ray

removal (on the right).

After cosmic ray removal, a Raman spectrum of the background was subtracted from each spectrum in order to compensate interfering signals originating from the optical elements in the laser light delivery pathway. Subsequently, spectra with maximum intensities below a threshold were removed from the data set: those spectra corresponded to areas of the sample without tissue. It is important to follow the correct order of the preprocessing procedures. Otherwise, the threshold criterion would be distorted by the background or cosmic spikes.

Since the heterogeneity of solid samples in terms of thickness or sample surface generates variations of the optical path length that may result in multiplicative light scattering effects masking the spectral variations due to the differences between chemical composition within the sample, before initiation of a multivariate analysis, a Multiplicative Signal Correction was applied to the data set, in order to separate the spectral variances due to real chemical differences from spectral variances due to physical effects such as thickness of samples.

Multiplicative Signal Correction (MSC)

In the basic form of an extended MSC every spectrum $z(v)$ is a function of the wavenumber v which can be expressed as a linear combination of a baseline shift a, a multiplicative effect b times a reference spectrum $m(v)$, linear and quadratic wavenumber dependent effects $d\,v$ and $e\,v^2$, respectively:

$$z(v)=a + b \cdot m(v) + d \cdot v + e \cdot v^2 + \varepsilon(v)$$

The term $\varepsilon(v)$ contains the unmodeled residues. The reference spectrum $m(v)$ is calculated by taking the sample mean of the data set. In the simple form of MSC, only the baseline shift and the multiplicative effect are considered. The parameters a and b can be estimated by ordinary least squares, and finally the spectra can be corrected according to

$z_{corr}(v) = (z-a) / b.$

The strength of MSC lies in the fact that the model is defined around a reference spectrum. This makes MSC modelling very stable even in the case where there are strong spectral changes arising from differences in sample thickness (34,35).

After preprocessing, a multivariate analysis was applied to the data set: we used the k-means cluster analysis. Lasch in 2004 already discussed the use of different unsupervised multivariate imaging approaches (hierarchical clustering, k-means cluster analysis and fuzzy-c-means cluster analysis) for the creation of pseudocolor microspectroscopic Infrared images of colorectal adenocacinoma and the same principles can be transferred to Raman mapping (36). Lasch concluded that the clustering method which yields color maps better resembling the histological tissue appearance is the hierarchical cluster analysis, but the computational memory requirements are very high. This could be a problem particularly in our case, where up to four data sets of around 2000 spectra each are analyzed together. k-means clustering offers the advantage of dealing with large data set with lower computational and memory requirements and this is the major reason for us to choose this method.

Cluster analysis and k-means cluster analysis

Clustering is the classification of objects into different groups, or more precisely, the partitioning of a data set into subsets (clusters), so that the data in each subset (ideally) share some common trait - often proximity according to some defined distance measure. Data clustering is a common technique for statistical data analysis, which is used in many fields, including machine learning, data mining, pattern recognition, image analysis and bioinformatics. Data clustering algorithms can be hierarchical or partitional. Hierarchical algorithms find successive clusters using previously established clusters, whereas partitional algorithms determine all clusters at once. An important step in any clustering is to select a distance measure, which will determine how the similarity of two elements is calculated. **Euclidean distance** is probably the most commonly chosen type of distance. It simply is the geometric distance in the multidimensional space. It is computed as:

$$\text{distance}(x,y) = \{\sum_i (x_i - y_i)^2\}^{½}$$

Other distances that can be chosen are: the Manhattan distance (also called taxicab norm or 1-norm), the maximum norm, the Mahalanobis distance that corrects data for different scales and correlations in the variables, the Hamming distance (sometimes edit distance) that measures the minimum number of substitutions required to change one member into another.

k-mean clustering (KMC) is a partitional clustering method, which obtains a "hard" (crisp) class membership for each statistical unit, i.e. the class membership of an individual statistical unit can take only the values of 0 or 1, starting from a predefined number of clusters. In general, the *k*-means method will produce exactly *k* different clusters of greatest possible distinction. If we apply this to our spectra data set, the KMC firstly divides the data set in a predefined number k of clusters and k spectra are initially randomly chosen to be the centers of each cluster. Then the Euclidean metric distance for each spectrum *x* from these centres is calculated for each wavenumber *i* and sums up according to the expression of the Euclidean distance

$$[\sum_i (x_i - \text{center}_i)^2]^{1/2}$$

The spectrum x is assigned to the nearest cluster centre on the basis of a minimal distance value. Next, according to the Mc Queen algorithm, new centres of the so formed clusters are calculated and distance values between the centres and each of the spectra are recalculated. If the closest centre is not associated with the cluster to which the spectrum currently belongs, the spectrum will switch its cluster membership to the cluster with the closest centre. The centre positions are recalculated every time a component has changed its cluster membership. This process continues until none of the spectra has been reassigned [36,37]. After all these procedures, clustered pseudo-color maps are produced and average spectra from all the clusters are imported to the program GRAMS (Thermo Fisher, USA) for analysis.

Chapter 4
Results and discussion

4.1 Normal colon [1]

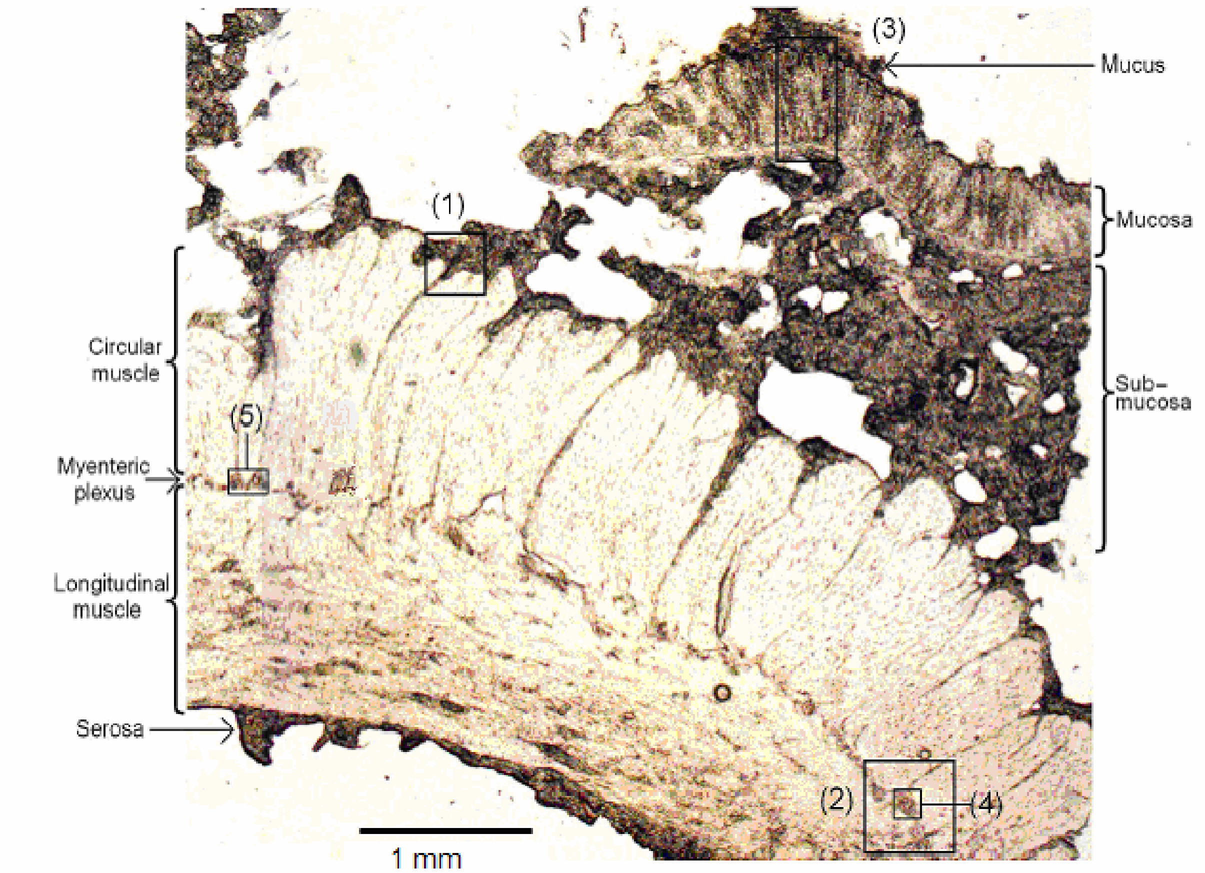

Fig. *10 : unstained normal colon tissue, with 5x magnification objective.*

Fig. 10 shows a 4.4×4.8 mm section of unfixed, unstained normal colon tissue, collected during closure of a colostomy from normally appearing and functioning descending colon in a 4 months old boy operated on for anorectal malformation. The gross architectural division into the main compartments is visible: mucosa, submucosa, circular muscle, longitudinal

[1] Results and pictures of normal colon Raman mapping have been accepted for publication in The Journal of Biophotonics: *Raman and FTIR microscopic imaging of colon tissue: a comparative study*. Krafft C, Codrich D, Pelizzo G, Sergo V. **DOI:10.1002/jbio.200710005**.

muscle and serosa. Since the tissue has not been fixed, the least compact tissue such as mucosa and submucosa show a fragmented appearance. The mucosa is the innermost, highly specialized layer of the gastrointestinal tract which is responsible for absorption and secretion. The submucosa consists of an irregular layer of connective tissue. Nerves and ganglia are the neurons of the enteric nervous system that controls the gastrointestinal tract. Ganglia are often connected with each other to form a complex system known as plexus. The myenteric plexus (or Auerbach's plexus) exists between the longitudinal and circular muscle layers and coordinates contractions of these layers. From this a secondary plexus, the submucosal plexus or Meissner's plexus, is derived and is formed by branches which perforates the circular muscle fibers: because of fragmentation of tissue, this plexus is scarcely visible. Three areas of interest were selected for Raman analyses encompassing the transitions between compartments. Area (1) corresponds to the transition from submucosa to circular muscle. A Raman image of 38×38 spectra was recorded. Area (2) represents the transition from circular muscle to longitudinal muscle. A ganglion cell in the center belongs to the myenteric plexus (4). A Raman image of 53×52 spectra was recorded. Area (3) corresponds to the transition from submucosa to mucosa. Lamina propria, a thin layer of connective tissue, and muscularis mucosae, a thin layer of smooth muscle, are located between these compartments. Epithelium is found within the mucosa and mucus as glandular secretion products above the mucosa. A Raman image of 39×71 spectra was recorded. Two Raman microscopic images of ganglions consisted of 59×59 spectra (4) and 85×49 spectra (5). The vibrational spectroscopic images were segmented by unsupervised k-means cluster analysis. Raman spectra with intensities below 500 relative units in the interval 1440-1460 cm^{-1} were removed from the data sets and these removals correspond to the white area of Fig.11 B; the interval used for clustering is the 750-1750 cm^{-1}, since bands outside this wavenumbers are weak and added no further information for spectra discrimination; when other clustering intervals are used, it is stated throughout the text.

4.1.1 Pseudo-color Raman maps

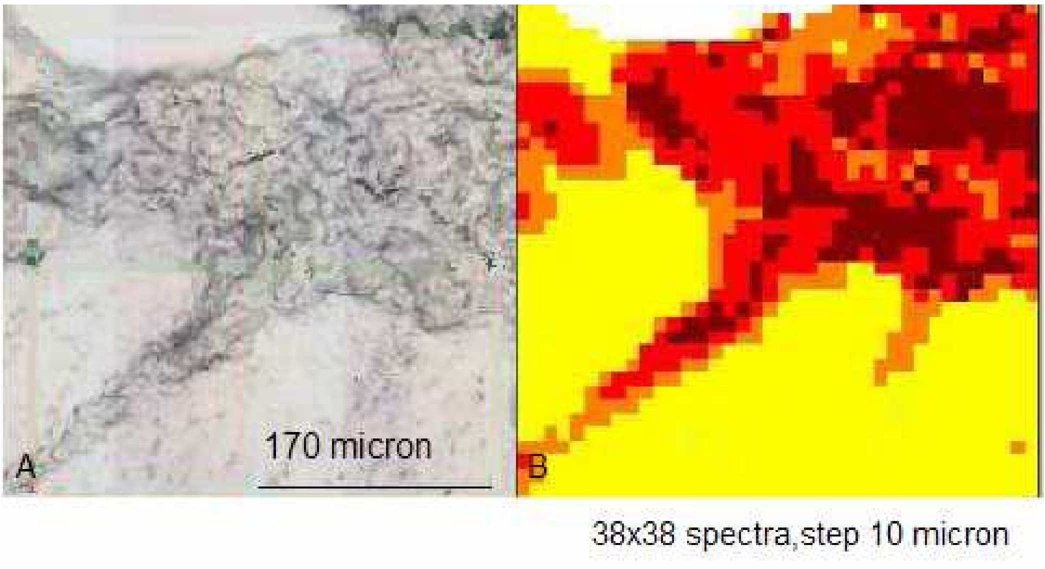

Fig. 11 A: unstained native tissue, magnification from area 1. B: pseudo-color Raman image of 38x38 spectra, collected with 50x magnification objective and a step size of 10 μm. Yellow color is assigned to the circular muscular layer; brown, red and orange are assigned to fibrous septa and connective tissue.

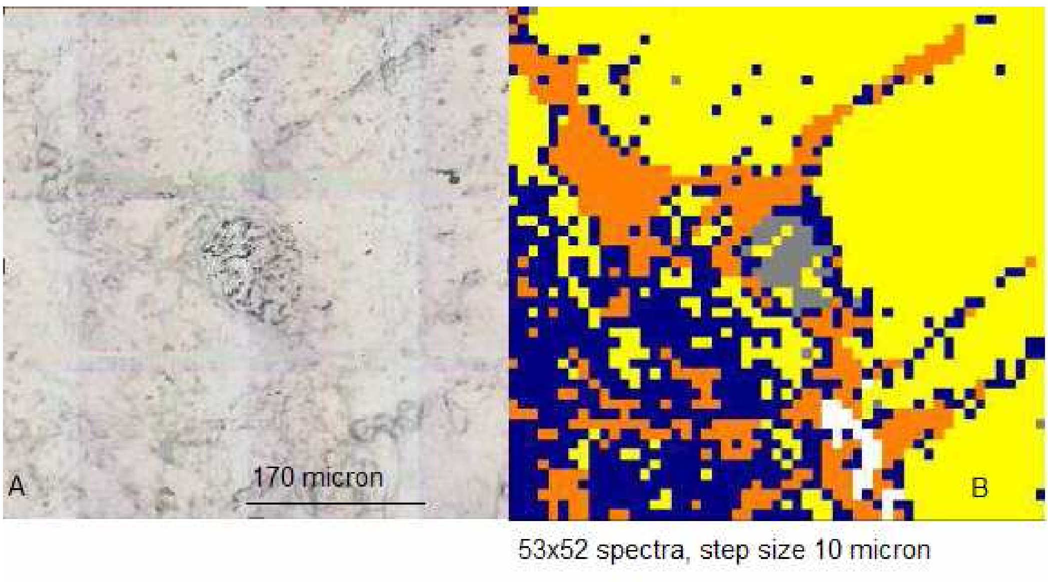

Fig. 12 A: native unstained photomicrograph of a magnification of area 2. B: pseudo-color Raman map from the same area, collected using a 50x magnification objective and a step size of 10 µm. Yellow cluster represents the circular muscular layer, the blue cluster represents the longitudinal muscular layer and the grey cluster represents a ganglion from the myenteric plexus. Orange cluster is assigned to connective fibrous tissue.

Two consecutive cluster analyses were performed for map of Fig. 12. The first analysis, that took into account the region between 750 and 1750 cm^{-1}, recognized the ganglion (grey), the fibrous septa (orange) and the muscular layers: these were subsequently separated by a further clustering in the interval 1190-1500 cm^{-1} into the circular (yellow) and the longitudinal (navy) muscular layer.

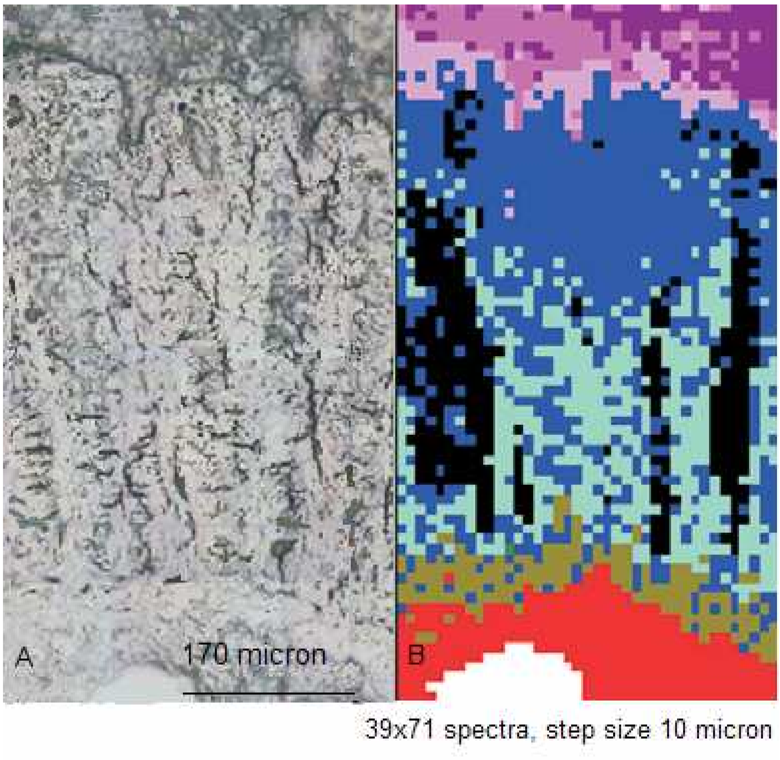

Fig. 13 A: native unstained photomicrograph of a magnification of area 3. B: pseudo-color Raman map from the same area, collected using a 50x magnification objective and a step size

of 10 μm. Blue and cyan clusters correspond to epithelial tissue; glandular crypts are depicted in black. Pink, magenta and violet clusters correspond to mucus; green cluster can be assigned to muscularis mucosa and red cluster is assigned to submucosa.

As for Fig. 12, also for the pseudo-color Raman map of Fig. 13 two cluster analyses were applied: the first clustering in the interval 750-1750 cm^{-1} separated the clusters of mucus (pink, magenta and violet) and submucosa (red) from epithelial tissue. A second cluster analysis in the interval 750-1020 cm^{-1} fractioned the epithelial area into three clusters (cyan, blue, black) and a fourth cluster (olive green) was observed and assigned to muscularis mucosae.

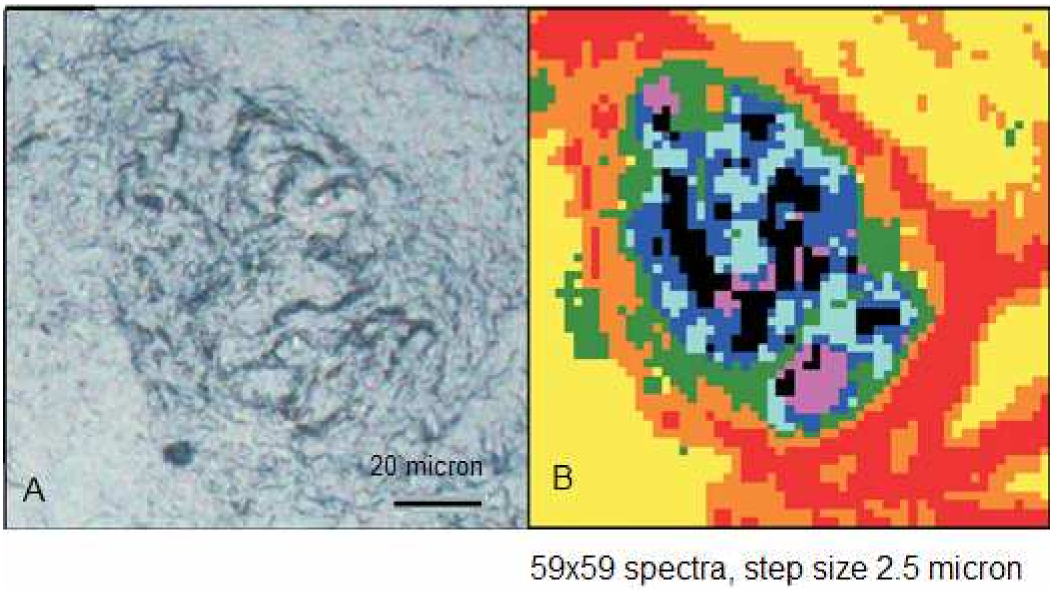

Fig. 14 A: native unstained photomicrograph of a ganglion in area 4. B: pseudo-color Raman map of the same area, collected with a 100x magnification objective and a step size of 2.5 μm. Red and orange clusters represent fibrous septa, yellow cluster is assigned to circular muscular layer; black, magenta, blue and cyan clusters represent sub-cellular features of ganglion. Green cluster is assigned to a transitional area.

A higher lateral resolution was used to collect this map to resolve sub-cellular features. Two subsequent cluster analyses were applied to obtain the map. The first clustering using the interval 1190-1750 cm^{-1} resolved five clusters (yellow, orange, red, green and the ganglion cluster). A second cluster analysis in the interval 690-815 cm^{-1}, segmented the ganglion cluster into black, magenta, cyan and blue clusters.

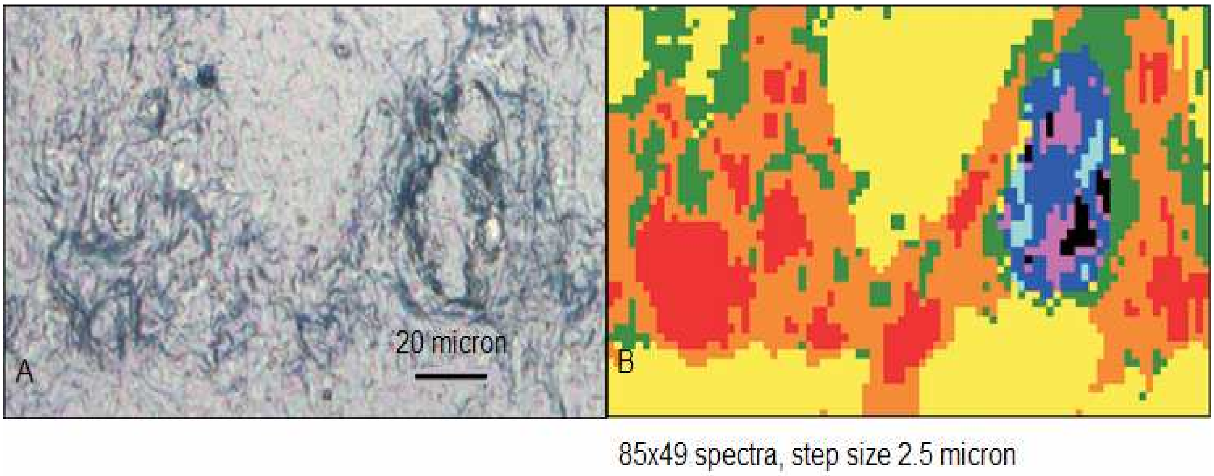

Fig. 15 A: native unstained photomicrograph of area 5. B: pseudo-color Raman map of the same area, collected with a 100x magnification objective and a step size of 2.5 μm. Cluster colors have been maintained as in Fig.14.

As can be seen from the pseudo-color map, the spot that on the left half of the unstained picture could be interpreted as a ganglion, is indeed characterized only by red and orange clusters, which represent collagen-rich tissue, without the typical ganglion clusters.

4.1.2 Raman spectra

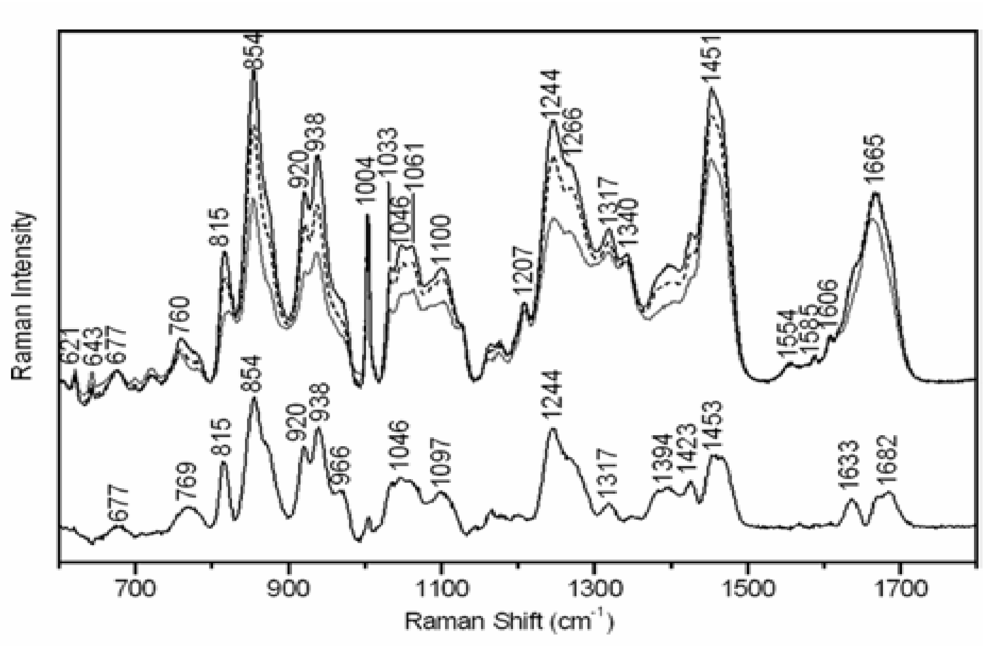

Fig. 16. Raman spectra from 600 to 1800 cm^{-1} of clusters of connective tissue. Solid black trace represents brown cluster, dashed trace represents the red cluster and solid gray trace represents orange cluster. Difference cluster (solid black minus solid grey) is displayed at the same scale.

Maximum intensity is seen in the spectrum of brown cluster, with decreasing intensities in red and orange spectra. The difference spectrum, obtained from the subtraction of spectrum of red cluster from the spectrum of brown cluster, is characterized by differences correlated to the coiled triple helix secondary structure and the unusual amino acid composition of collagen. The amino acid composition and secondary structure of collagen differ significantly from standard proteins. The rich content in glycine, proline and hydroxyproline restricts the conformational freedom of the backbone. The fibrous protein collagen adopts the three stranded coiled helical secondary structure. These properties distinguish collagen from other proteins and enables its identification by the following bands: positive peaks assigned to Amide I vibrations at 1682-1633 cm^{-1}, to Amide III at 1244 cm^{-1} and to CH_2/CH_3 deformation vibrations of proteins at 1453 cm^{-1}. Collagen high content of amino acids such as proline is showed by the positive band at 854 cm^{-1}.

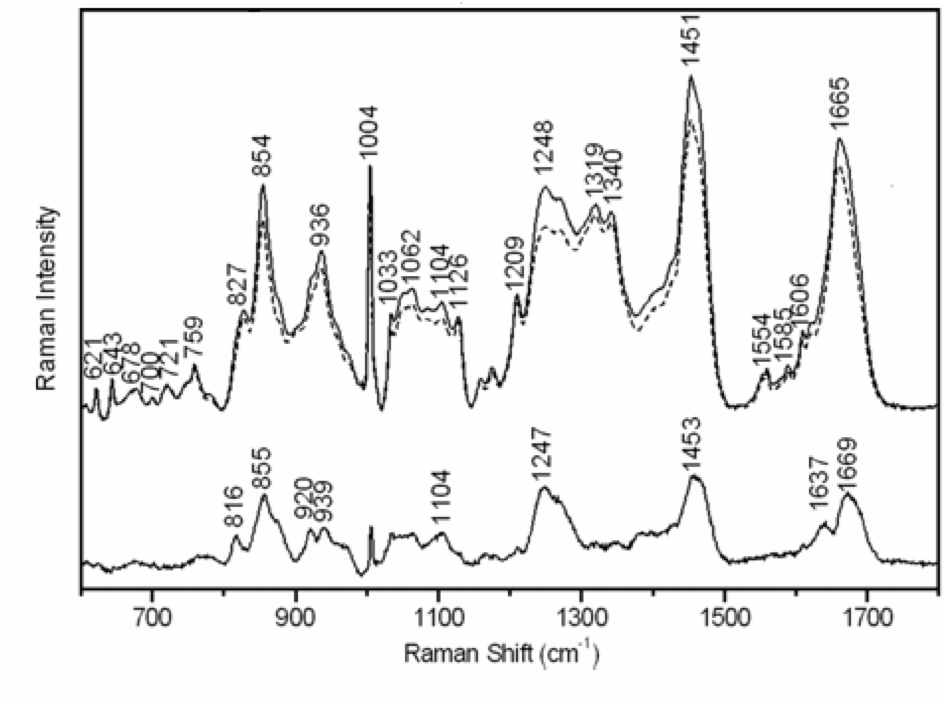

Fig. 17 Raman spectrum from 600 to 1800 cm^{-1} of muscle layers. Solid trace represents the blue cluster (longitudinal muscular layer) and dashed trace the yellow one (circular muscular layer). Difference spectrum (solid minus dashed) is displayed at two-fold magnified scale.

The difference spectrum is qualitatively similar to the difference spectrum for connective tissue (Fig. 16). It indicates higher collagen content in longitudinal muscle than in circular muscle. Due to the lower quantity of the variances, the difference spectrum is displayed at magnified scale. Because the collagen content in muscle tissue was lower than in connective tissues as evident from the less intense collagen associated bands, spectral contributions of other proteins, of lipids (721 cm^{-1}) and of cholesterol (700 cm^{-1}) were better resolved. In particular, numerous Raman bands are assigned to aromatic amino acids phenylalanine (621, 1004, 1031, 1209, 1585 cm^{-1}), tyrosine (643, 827, 854, 1605 cm^{-1}) and tryptophan (759, 1554 cm^{-1}).

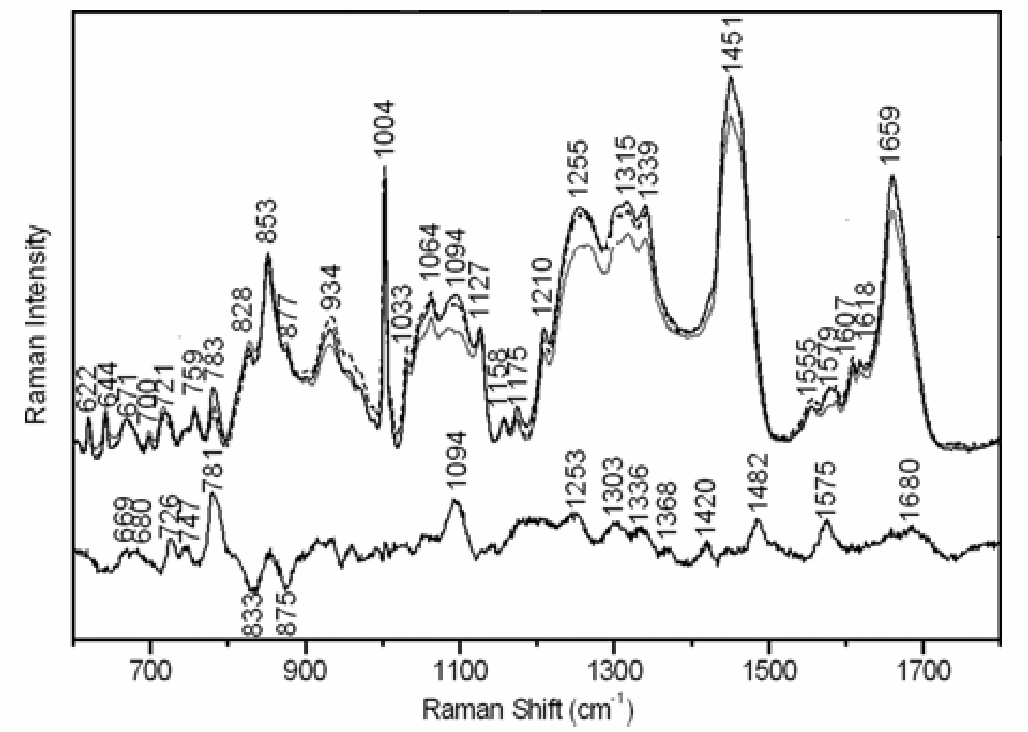

Fig. 18 Raman spectrum from 600 to 1800 cm^{-1} of epithelial tissue representing the cyan (solid black), blue (dashed) and black (solid gray) clusters. Difference spectrum (solid black minus solid gray) is displayed at two-fold magnified scale.

Before calculating the Raman difference spectrum, the spectra of the cyan and black clusters were scaled in order to minimize differences near the most intense protein bands (1004, 1451, 1659 cm^{-1}). Positive difference bands are assigned to nucleotides (thymine: 669, 747, 1368, 1680 cm^{-1}, guanine: 680, 1482, 1575 cm^{-1}, adenine: 726, 1303, 1336 cm^{-1}, cytosine: 781, 1253 cm^{-1}) and to the backbone (1094, 1420 cm^{-1}) of DNA. Negative difference bands (833, 875 cm^{-1}) are associated with the production of mucus in glands. The spectra of the blue clusters were similar to the spectra of the cyan clusters, however with lower spectral contributions of DNA. The intensity of the DNA bands can be correlated with the grade of divisional activity. The mucosal epithelium of the gastrointestinal tract contains epithelial cells which undergo a continual turnover and renewal and which have a higher proliferation rate than other colonic cells. Beside the elevated levels of DNA and mucus, spectral contributions of collagen are further reduced in the spectra of epithelial tissue (Fig. 18) compared with the spectra of connective tissue (Fig. 16) and muscle tissue (Fig. 17).

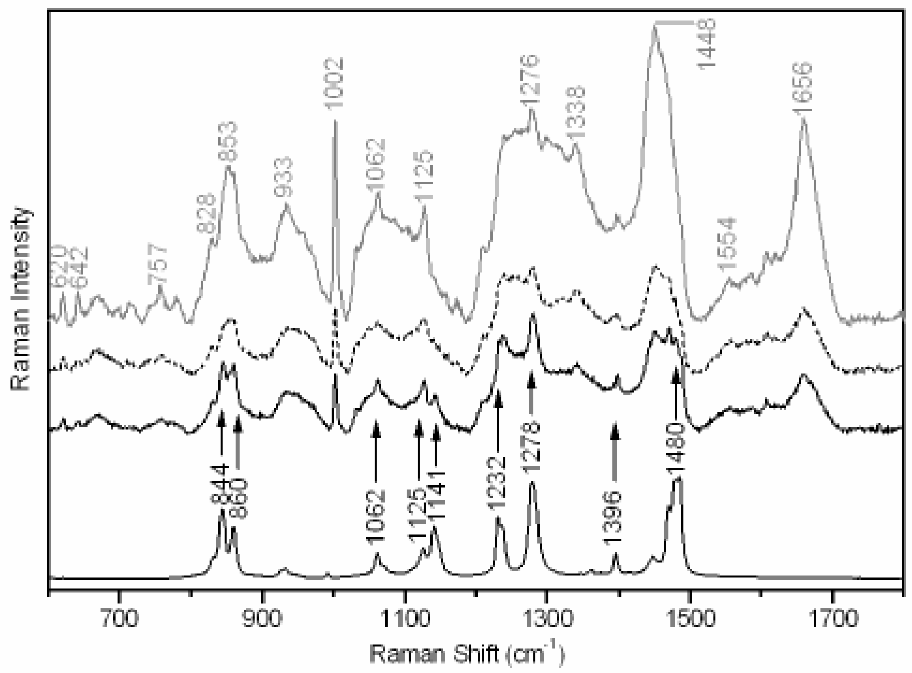

Fig. 19. Raman spectra from 600 to 1800 cm^{-1} of secretion products representing the pink (solid grey), magenta (dashed) and violet (solid black) clusters in Fig. 13. A Raman spectrum of PEG 4000 is included at the bottom.

The Raman spectra indicate that the intensities of protein bands (e.g. 1004, 1450, 1660 cm^{-1}) decrease and the bands of the carbohydrate moiety of mucus increase in the order pink (gray trace) > magenta (dashed trace) > violet clusters (black trace). Since the spectra contained few bands that were difficult to assign and which were not reported as mucus-peculiar in literature, we thought about contamination by other compounds. It is common practice in abdominal surgery to flush the intestinal tract before operation and in our department, a solution called Isocolan [Bracco, Italy] is used for bowel preparation. Comparison with a Raman spectrum of polyethyleneglycol (PEG) 4000 (main constituent of Isocolan) revealed that the spectral contributions at 844, 860, 1062, 1125, 1141, 1232, 1278, 1396 and 1480 cm^{-1}

which have maximum intensities in the spectrum of the violet cluster can be assigned to this compound.

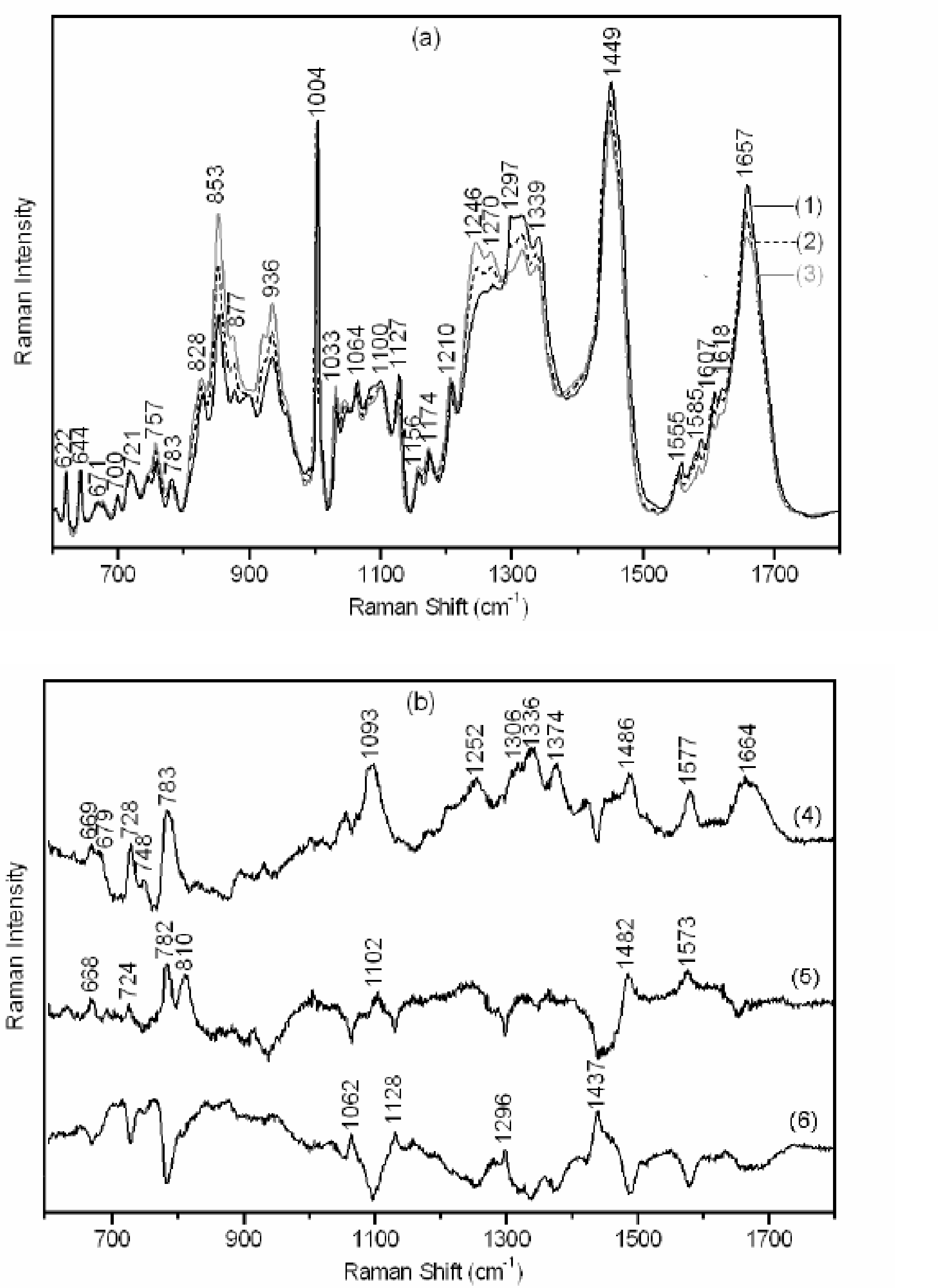

Fig. 20 ***(a)****: Raman spectra from 600 to 1800 cm-1 of the ganglion (trace 1, solid black), the transition (trace 2, dashed) and fibrous septa (trace 3, solid gray).* **(b)**: *Raman difference*

spectra: trace 4= black cluster minus trace 1; trace 5 = magenta cluster minus trace 1 and trace 6= cyan cluster minus trace 1.

The mean spectra of fibrous septa (orange cluster), the inner ring (green cluster) and the ganglion are overlaid in Fig. 20a. The spectra are composed of contributions of proteins, nucleic acids and lipids which are indicated by the labeled bands. The Raman spectrum of fibrous septa is characterized by intense collagen bands at 853, 936 and 1246 cm^{-1} which is typical for connective tissue. In the Raman spectrum and the ganglion lipid bands at 1064, 1127, 1297, 1449 and 1657 cm^{-1} and nucleic acid bands at 783 and 1100 cm^{-1} are more intense. However, some of the differences require a magnification of the spectra to be resolved. The properties of the Raman spectrum of the inner ring lie between the spectra of the fibrous septa and the ganglion. Spectral contributions of lipids and nucleic acids are less intense and spectral contributions of collagen are more intense than in the ganglion. For inspection of the small spectral changes between the subcellular clusters, difference spectra were calculated between the black, magenta and cyan clusters minus the mean spectrum of the ganglion (Fig. 20b). Positive bands in the difference spectrum (black minus ganglion) agree with difference bands in Fig. 18 which were assigned to nucleotides and the backbone of DNA. Positive bands in the difference spectrum (magenta minus ganglion) were assigned to RNA because of the A-form backbone marker bands at 810 and 1102 cm^{-1} and the absence of thymine bands at 748, 1374 and 1664 cm^{-1}. Other nucleotide bands due to adenine, guanine and cytosine are shifted as a consequence of the different sugar pucker conformation. Positive bands at 1062, 1128, 1296 and 1437 cm^{-1} in the difference spectrum (cyan minus ganglion) are assigned to fatty acid side chains of lipids. As the Raman spectrum representing the blue cluster is very similar to the mean spectrum of the ganglion, the difference spectrum is not shown. Negative difference bands were not discussed because they solely reflect the complementary information of the positive bands in this case. Based on the Raman spectra, the black cluster is associated with the nucleus, the magenta cluster with high RNA content in the cytoplasm, the cyan cluster with high lipid content in the cytoplasm and the blue cluster with the normal cytoplasm of ganglion. Altogether, the Raman images point to several cell nuclei which are consistent that ganglions are formed by coalescence of multiple neural cells. Higher lateral resolutions are required to identify more details.

4.2 Normal lung[2]

These results describe a Raman image of normal lung tissue of an infant patient that was collected and examined, before studying the biochemical changes that accompany pediatric lung pathologies and malformations. Lung tissue was obtained from a newborn male, four days old patient submitted to upper right and middle lobectomy because of respiratory distress due to extended congenital cystic adenomatoid malformation. The specimen which was studied here represents the healthy, lower right lobe. A Raman image of 3420 spectra was recorded from a 5.6 mm by 5.9 mm tissue section in mapping mode using 785 nm excitation laser and a step size of 100 micrometer.

4.2.1 Pseudo-color Raman maps

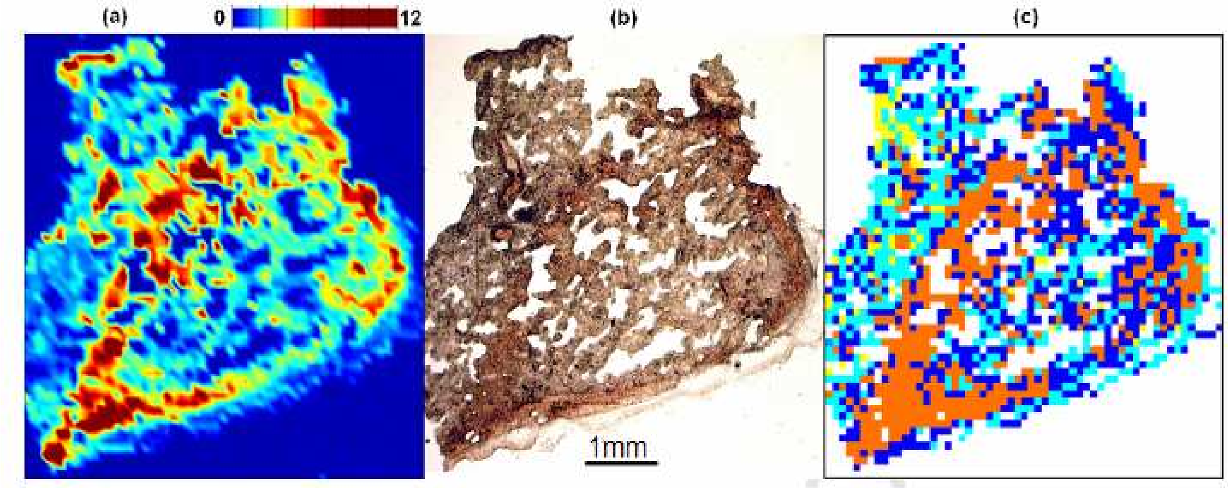

Fig. 21: Chemical map at 1576 cm^{-1} (a), photograph (b) and color coded segmentation by cluster analysis (c) of a 57×60 Raman image obtained from a 5.6×5.9 mm^2 lung tissue section, with a step size of 100 μm. Color code in (c): Lung tissue of high (orange), medium (blue) and low (cyan) content of red blood cells and blood vessels (yellow). Bar = 1 mm.

[2] Results and pictures of normal lung Raman mapping have been published in Vibrational Spectroscopy. *Raman and FTIR imaging of lung tissue: methodology for control samples.* C Krafft, D Codrich, G Pelizzo,V Sergo. **46 (2008) 141-149**

Vibrational spectroscopic images can be constructed in a univariate mode where chemical maps (also called functional group maps) based on peak intensities, peak areas or peak ratios are generated (Fig. 21(a)). While these methods provide information on the distribution and relative concentration of a particular functional group and hence a specific major biomolecule, they are not very useful in terms of classifying anatomical and histopathological features within tissue sections with strongly overlapping spectral contribution from various biomolecules. To utilize a larger extent of spectral information, which is usually distributed over a broad spectral region, multivariate image reconstruction is required (Fig. 21(c)).

After preprocessing including removal of spectra with intensities near 1450 cm^{-1} below a threshold of 1 relative units, KMC segmented the Raman spectra into four groups using the interval 1190-1750 cm^{-1}. The results did not change significantly using other spectral ranges. Clusters were present in different amount within the map: the orange constituted 32% of the total pixels, blue 37%, cyan 27% and yellow 4%. Comparison of Figs. 21(a) and (c) reveals that the orange cluster represents the most intense Raman spectra.

4.2.2 Raman spectra

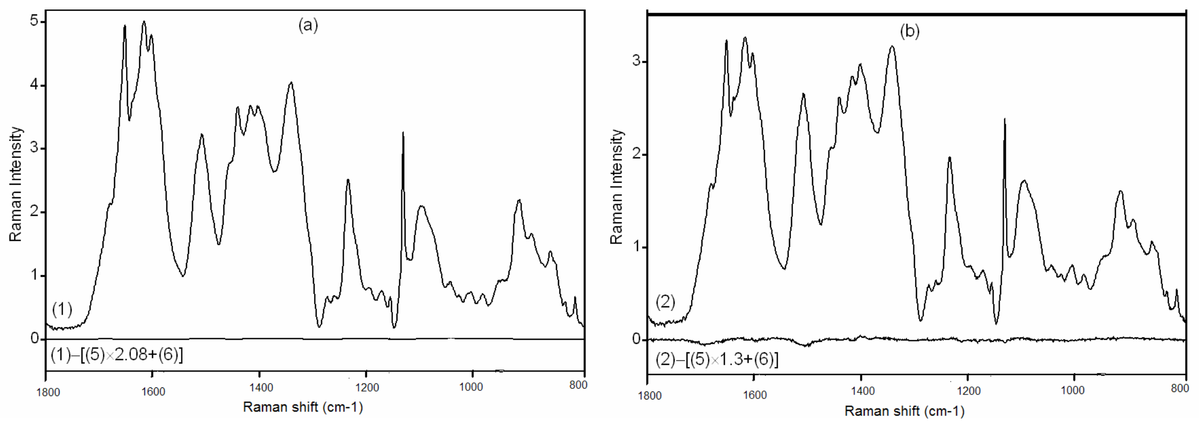

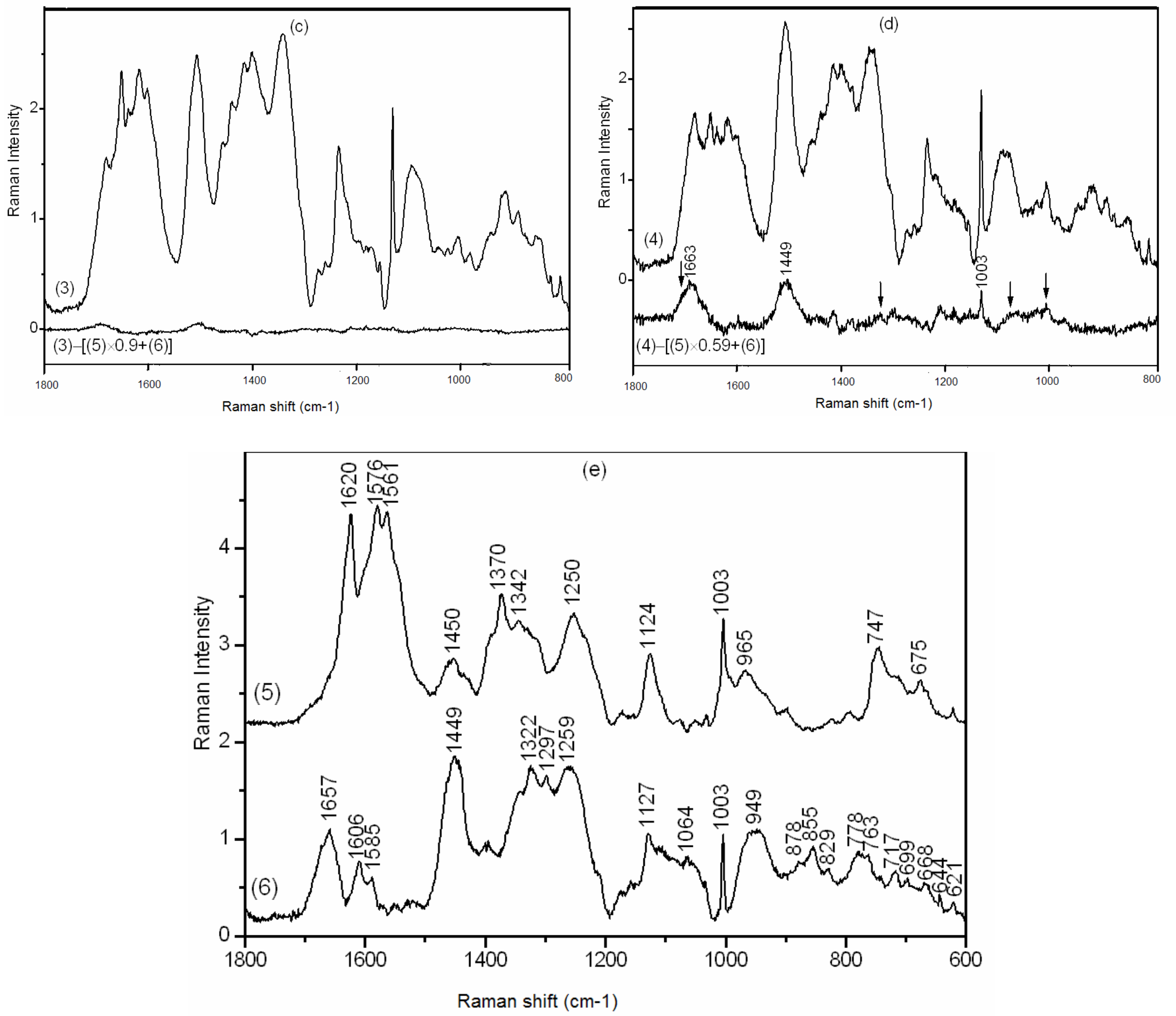

Fig. 22 (a): Average Raman spectrum from 600 to 1800 cm^{-1} of cluster orange in Fig. 21(c) (trace 1). (b): Average Raman spectrum from 600 to 1800 cm^{-1} of cluster blue in Fig. 21(c) (trace 2). (c): Average Raman spectrum from 600 to 1800 cm^{-1} of cluster cyan in Fig. 21(c) (trace 3). (d): Average Raman spectrum from 600 to 1800 cm^{-1} of cluster yellow in Fig. 21(c) (trace 4). (e): Spectrum (5) represents spectral contributions of red blood cells in lung tissue. Spectrum (6) represents lung tissue without the contributions of red blood cells. Difference spectra between average Raman cluster spectra and a linear combination of (5) and (6) were calculated and shown.

The averaged Raman spectra of the orange, blue, cyan and yellow clusters are shown in traces (1), (2), (3) and (4) of Fig. 22. The different scales indicate that the intensities decrease in the order (1)>(2)>(3)>(4). In particular, the spectra differ in the interval 1500-1700 cm^{-1}. The typical amide I band of proteins near 1660 cm^{-1} strongly overlaps with intense bands near 1561, 1576 and 1620 cm^{-1} which are assigned to hemoglobin in red blood cells [38]. Contributions of hemoglobin are enhanced in Raman spectra upon excitation at 785 nm due to the presence of the heme group. Difference spectra (1)-(2), (1)-(3) and (2)-(3) reveal that the spectral changes are qualitatively similar. The average of these difference spectra is included in trace (5) of Fig. 22. According to the literature [38], all bands in (5) are associated with red blood cells which are, however, in an aggregated, denatured state as evident from the band at 1250 cm^{-1}. Spectrum (5) was subtracted from spectra (1), (2) and (3) in order to obtain the Raman signature of lung tissue without red blood cells. Criterion for the subtraction factor was the compensation of hemoglobin bands in the interval 1500-1550 where most biological macromolecules such as proteins, lipids and nucleic acids show no intense bands. The average of the subtraction procedure is included in trace (6) of Fig. 22. Protein bands dominate in (6) which are assigned according to the literature [39,40] to aromatic amino acid side groups of phenylalanine (621, 1003, 1585 cm^{-1}), tyrosine (644, 829, 855, 1606 cm^{-1}), tryptophan (763, 878, 1585 cm^{-1}), to aliphatic amino acid side groups (1127, 1322, 1449 cm^{-1}) and to the peptide backbone (949, 1259, 1657 cm^{-1}). Further bands of lipids (699, 717, 1064, 1297 cm^{-1}) and nucleic acids (668, 778 cm^{-1}) are also resolved in (6). The absence of significant bands in difference spectra in Figs. 22(a), (b) and (c) demonstrate that Raman spectra (1), (2) and (3) can be reasonably reconstructed by linear combinations of traces (5) and (6). The fit coefficients confirm that variations of the hemoglobin component (5) constitute the main difference, whereas the remaining components (6) are constant. Raman spectrum (4) is an exception in that the hemoglobin component (5) has a minimum value of 0.59 and positive difference bands in Fig. 22(d) indicate an increase of the protein content. The arrows in (4) point to the tendency that bands near 855, 940, 1245 and 1680 cm^{-1} increase which belong to typical bands of collagen in smooth muscle of blood vessels [(41)].

On the macroscopic scale, the main Raman spectroscopic variations in lung tissue were assigned to the red blood cells content. In particular, the Raman spectra in Fig. 22 showed that other components such as proteins and lipids are homogenously distributed in lung tissue. The Raman spectra of lung tissue strongly differed from Raman spectra of bronchial tissue which have been presented previously [(29)]. Since a high blood perfusion rate is a typical property of lung tissue and the heme group of hemoglobin gives enhanced Raman bands due to a resonance effect [(38)] at 675, 747, 965, 1003, 1124, 1250, 1324, 1370, 1561, 1576 and 1620 cm^{-1} upon 785 nm excitation, changes in the blood perfusion or in the red blood cells content can be easily detected by Raman spectroscopy. Because red blood cells absorb near infrared radiation which is utilized in numerous applications of near infrared spectroscopy (NIRS) [(42,43)], laser intensity must be kept below the damage threshold during Raman data acquisition.

Beyond red blood cells, in the respiratory tract other tissue components are present such as smooth muscles, which exist in blood vessels and bronchioles. Spectral contributions of collagen were detected in the protein component of the yellow cluster by Raman bands near 855, 940, 1245 and 1680 cm^{-1} (Fig. 22). Due to their low intensities relative to the protein bands of lung tissue, these bands could only be identified after subtraction of the hemoglobin component (Fig. 22(d)).

4.3 Lung malformations: CCAM[3]

The biochemical composition of CCAM has not been studied in detail in literature so far. Therefore, the scope of this part of the project was to investigate the changes in the biochemical composition between normal lung tissue and CCAM. The methods and results of the preliminary study on normal lung tissue of section 4.2 are transferred to collect and analyze macroscopic images with lateral resolutions of 100 µm. Furthermore, microscopic images with lateral resolutions near 10 µm are presented in order to identify more details. Lung tissue specimens were obtained from two infant patients undergoing lobectomy because of respiratory distress due to extended solid-type CCAM. The excised lobes contained also a fraction of normal tissue which served as controls.

4.3.1.i Pseudo color Raman maps of macroscopic features

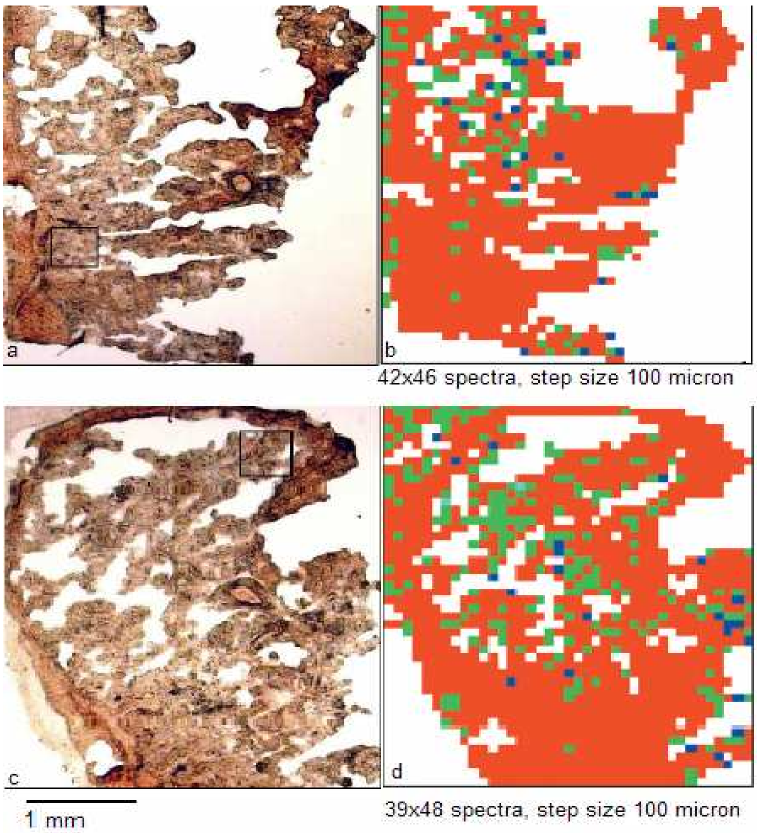

---

[3] Results and pictures of CCAM mapping have been published in The Analyst. *Raman mapping and FTIR imaging of lung tissue: congenital cystic adenomatoid malformation*. Krafft C, Codrich D, Pelizzo G, Sergo V. **(2008) 133: 361-371**

Fig. 23 ***(a), (c)****: Photographs of lung tissue obtained from the macroscopically normal parenchyma of patient 1 (a) and of patient 2 (c). Black boxes show the area of microspectroscopic analyses presented later on in Fig. 25****. (b), (d)****: Raman maps of the same areas. The color code represent segmentation into three groups based on cluster analysis of spectra.*

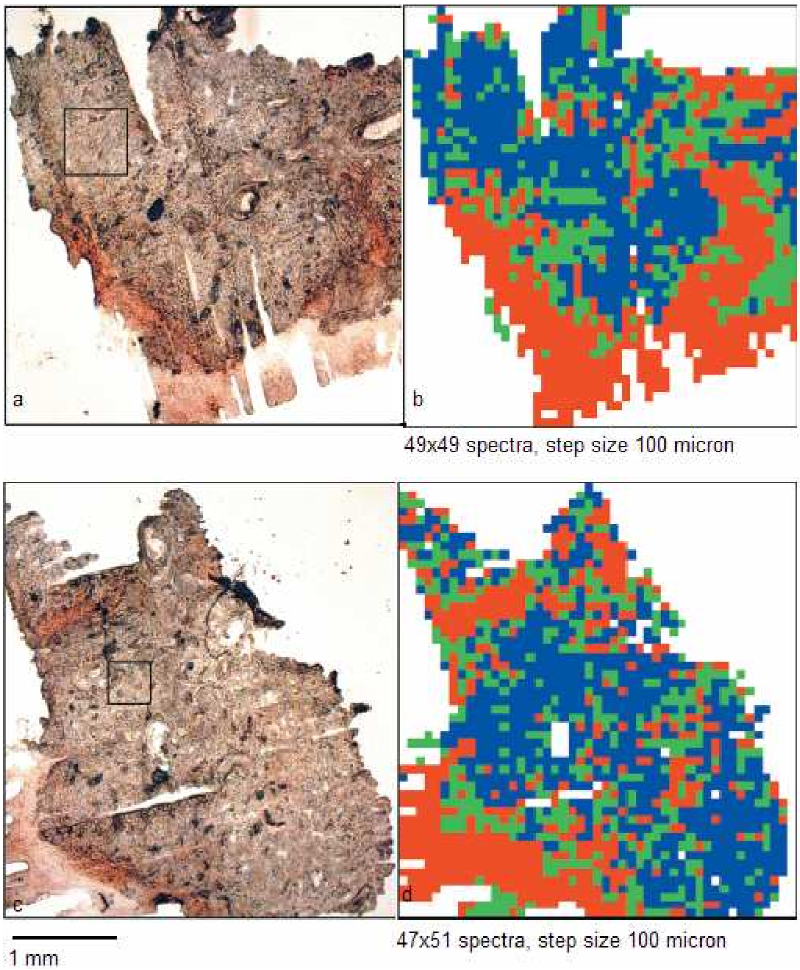

Fig. 24 ***(a),(c)****: Photographs of lung tissue obtained from the macroscopically affected lobe of patient 1 (a) and of patient 2 (c). Black boxes show the area of microspectroscopic analyses presented later on in Fig. 25.* ***(b), (d)****: Raman maps of the same areas. The color code represent segmentation into three groups based on cluster analysis of spectra.*

After pooling the four Raman maps (Fig. 23 b,d and Fig. 24 b,d) a cluster analysis was performed in the spectral interval 1190-1750 cm^{-1}. In Fig. 23(b) and (d) most spectra were assigned to the red cluster (85% and 81%, respectively), followed by the green cluster (12% and 17%) and the blue cluster (3% and 2%). In Fig. 24(b) and (d) spectra of the red cluster (38% and 31%) are mainly located near the outer regions, and spectra of the blue cluster (38% and 43%) and of the green cluster (24% and 25%) are found in the core regions.

4.3.1.ii Pseudo-color Raman maps of microscopic features of CCAM

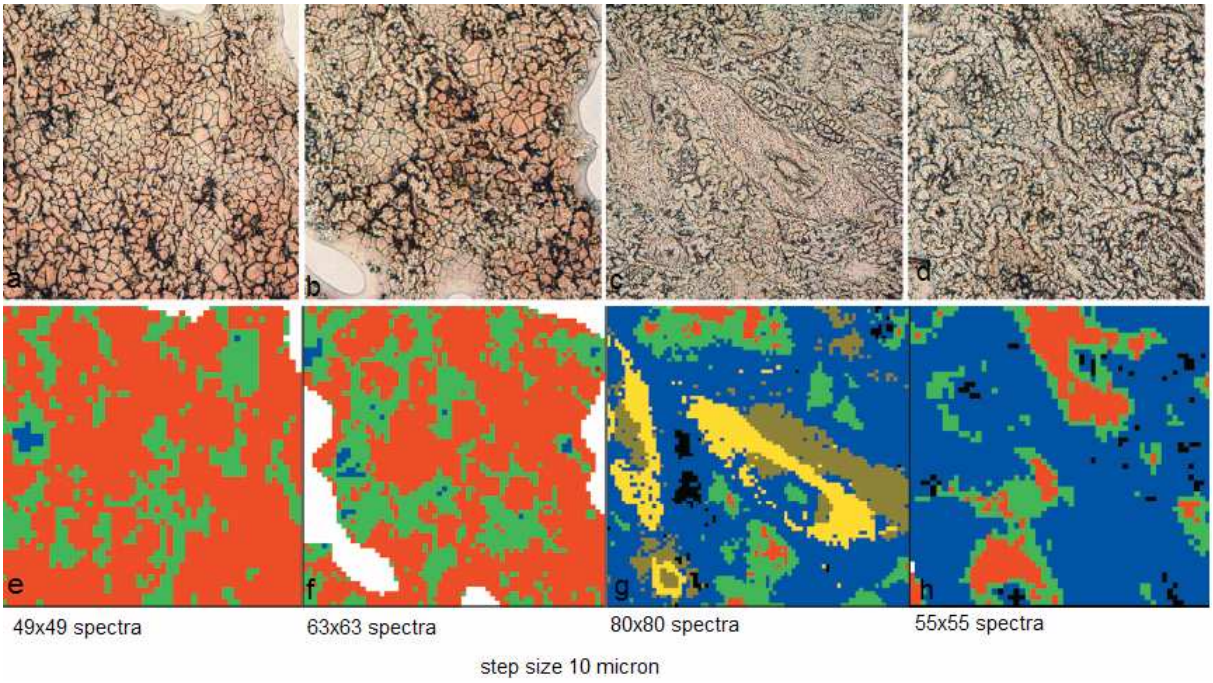

Fig. 25 ***(a, b, c, d)****: photographs of unstained lung tissue from boxes showed in Figs. 23-24.* ***(e, f, g, h)****. Pseudo color Raman maps of the same areas. First and second columns show unaffected lung parenchyma of patients 1 and 2, respectively. Third and fourth columns show CCAM of patients 1 and 2, respectively.*

A cluster analysis of the combined Raman data sets containing 15795 spectra was performed in the wavenumber interval 1190-1750 cm^{-1}. Compared with Figs. 23-24, the number of clusters was increased by three and the additional clusters were colored by yellow, olive and black. The cluster memberships which coincide with the clusters in Figs. 23-24 are coded in the same colors as before.

In normal lung tissue of patient 1 (first column) and of patient 2 (second column), most spectra were assigned to the red clusters (74%-65%), followed by the green clusters (25%-34%) and the blue clusters (1%-1%). In CCAM of patient 1 (third column) and of patient 2 (forth column), most spectra were assigned to the blue clusters (56%-71%). Additional clusters form the second largest groups (28%-1.7%), and only few spectra were assigned to the green (13.4%-16%) and red (2.6%-11.3%) clusters. Whereas the red, green and blue clusters were already identified in FTIR images and Raman maps in Figs. 23-24, additional clusters were assigned to new features in microscopic images of CCAM.

4.3.2.i Raman spectra from macroscopic maps of CCAM

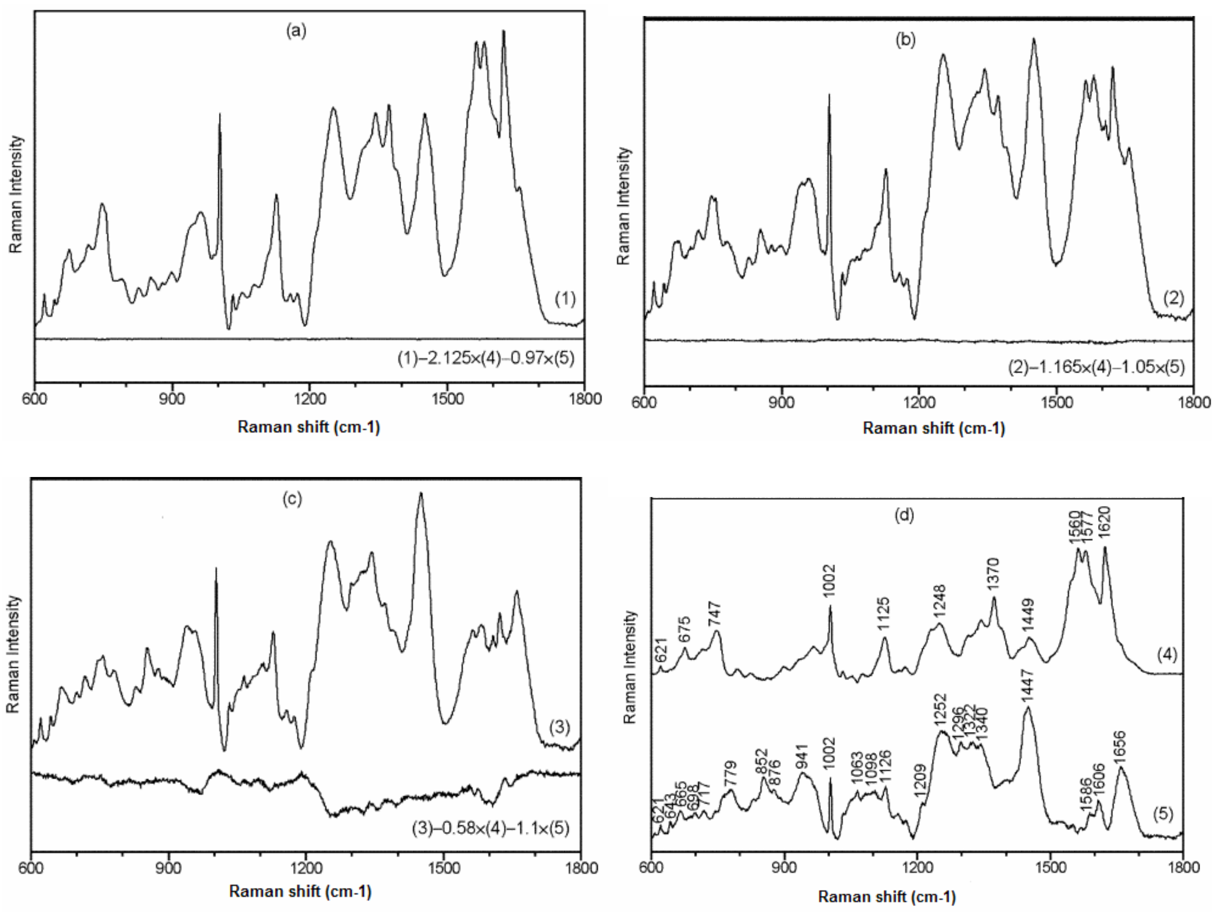

Fig. 26 (a): Average Raman spectrum from 600 to 1800 cm^{-1} from the red cluster (trace 1). (b): Average Raman spectrum from 600 to 1800 cm^{-1} from the green cluster (trace 2). (c): Average Raman spectrum from 600 to 1800 cm^{-1} from the blue cluster (trace 3). (d): Spectral *contribution of red blood cells (trace 4) and of lung tissue without red blood cells (trace 5) were calculated from the red and green clusters.*

Difference spectra between Raman spectra and linear combination of (4) and (5) are displayed at the bottom of Figs. 25 (a), (b), (c).

Spectral variations are observed in particular in the interval 1500-1700 cm^{-1}. Spectral contributions in this interval are assigned to hemoglobin which is a major constituent of red blood cells [38, 41]. Upon excitation of Raman spectra with 785 nm radiation, bands of red blood cells were enhanced and partly masked the weaker bands of other proteins, lipids, carbohydrates and nucleic acids. Therefore, the same procedure used in section 4.2 was applied to CCAM to separate the spectral contributions of red blood cells from the remaining components. Spectrum (4) was calculated from the differences between the spectra of the red and the green clusters in Raman maps of Fig. 23(b,d) and Fig. 24(b,d). Spectrum (5) was obtained by subtracting spectrum (4) from the spectra of the red and the green clusters in Raman maps of Fig. 23(b,d) and Fig. 24(b,d). All bands in spectrum (4) are assigned to hemoglobin in an aggregated, denatured state [38,41]. Bands in spectrum (5) are assigned to proteins (621, 643, 852, 941, 1002, 1209, 1252, 1322, 1340, 1447, 1586, 1606 and 1656 cm^{-1}), lipids (698, 717, 1063, 1126 and 1296 cm^{-1}) and nucleic acids (665, 779 and 1098 cm^{-1}). The absence of significant bands in difference spectra of Figs. 25(a) and (b) indicates that linear combinations of spectra (4) and (5) closely approximate spectra (1) and (2). Whereas the coefficients for spectrum (4) decrease from 2.125 in spectrum (1) to 1.165 in spectrum (2), the fit coefficients for spectrum (5) are close to 1. This result confirms that the main variations are differences in the red blood cells content. The fit coefficients in Fig. 25(c) decrease to 0.58 for spectrum (4) and increase to 1.1 for spectrum (5). The difference spectrum shows broad positive and negative bands which coincide with the positions of hemoglobin bands, e.g. near

1250 and 1600 cm^{-1}. No difference bands can clearly be assigned to proteins, lipids or other constituents. The Raman data show that the hemoglobin content is lower in CCAM than in normal lung tissue because the red and green clusters which are represented by traces (1) and (2) are more abundant in normal lung tissue and the blue cluster which is represented by trace (3) is more abundant in CCAM.

4.3.2.ii Raman spectra from microscopic maps

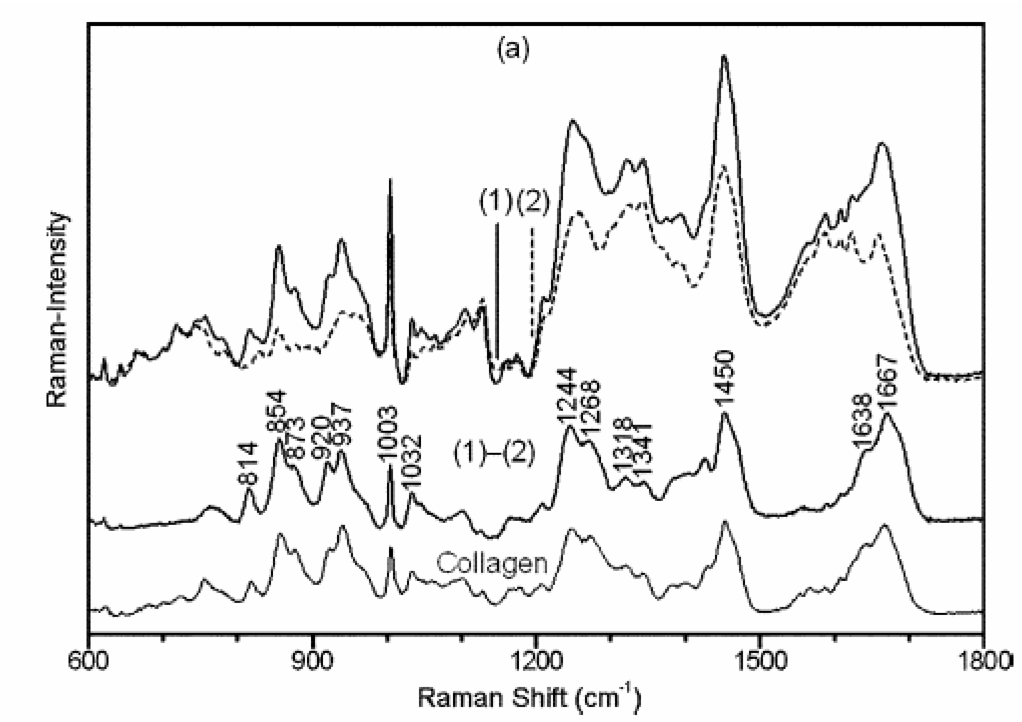

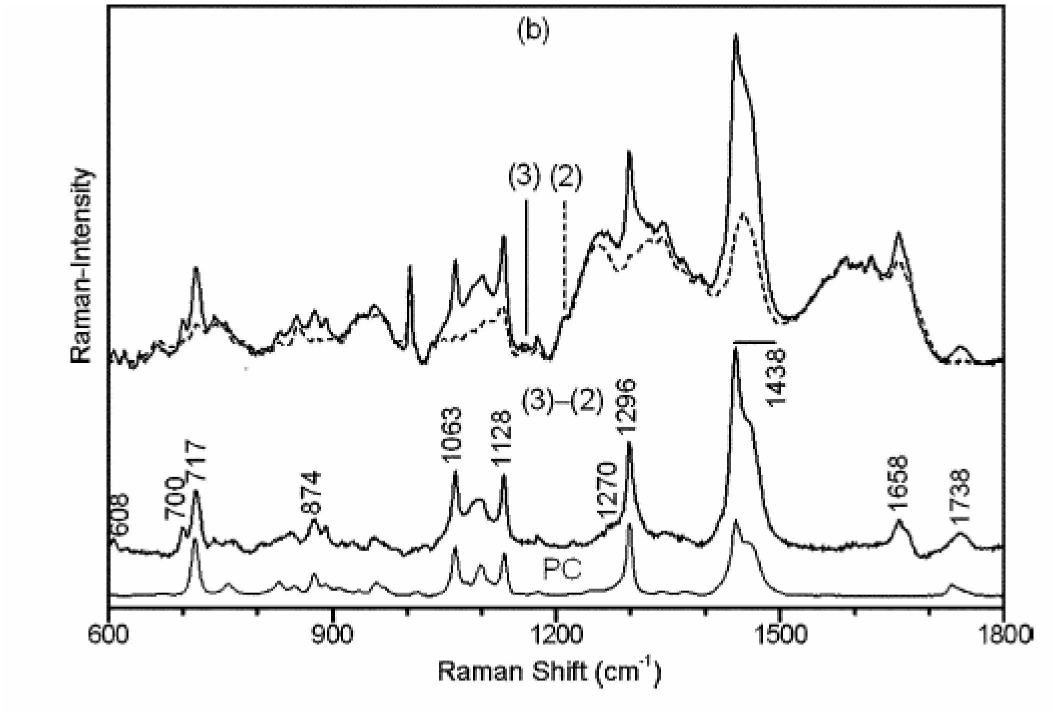

*Fig. 27**(a)**: Average Raman spectra from 600 to 1800 cm^{-1} from yellow cluster (trace 1). **(b)**: Average Raman spectra from 600 to 1800 cm^{-1} from black cluster (trace 3) of maps in Fig. 25 (g, h). Trace 2 represents a linear combination of red blood cells' spectrum and of the remaining components' spectrum. Difference spectra and spectra of reference compounds are included for comparison. PC= phosphatidylcholine*

The Raman spectra of normal lung tissue and of CCAM which represent the red, green and blue clusters in Raman microscopic maps in Fig. 25 contain the same spectral properties as the Raman spectra in Figs. 23-24. Therefore, they are not displayed. The Raman spectrum of the yellow cluster (trace 1) is overlaid with the linear combination $0.4\ H + 0.55\ R$ (trace 2) of the spectral contributions of hemoglobin H and of the remaining components R (Fig. 27a). The spectra H and R were similar as spectra (4) and (5) in Fig. 26(d). They were calculated from Raman spectra of the red, green and blue clusters of Fig. 25(g) because the yellow cluster is only present here. The difference between spectra (1) and (2) was included in Fig. 27(a). The absence of negative difference bands and minimal positive difference bands in the intervals 650-750 cm^{-1} and 1500-1600 cm^{-1} indicate that spectral contributions of lipids, DNA and hemoglobin are well compensated. The remaining protein bands closely resemble the spectral signature of collagen (Fig. 27a), which is characterized by marker bands at 814, 854, 873, 920, 937, 1244, 1638 and 1667 cm^{-1}[41].

The Raman spectrum of the black cluster (trace 3) is overlaid with the same linear combination $0.4\ H + 0.55\ R$ (trace 2) of the spectral contributions of hemoglobin H and the remaining components R (Fig. 27b). The difference spectrum between spectra (3) and (2) also contains no significant negative bands. The absence of positive differences near the prominent protein, hemoglobin and DNA bands indicate that these components did not change in spectra (3) and (2). The high similarity of the difference spectrum with a Raman spectrum of phosphatidylcholine (PC) in Fig. 27(b) suggests that this lipid constitutes the main difference. The choline head group is characterized by bands at 718 and 875 cm^{-1} and the fatty acid chains by bands at 1065, 1130, 1298 and 1440 cm^{-1}. The side chains of the synthetic PC (purchased from Sigma Aldrich, Germany) were derived from palmitic or hexadecanoic acid which are 16 residues long. Further difference bands at 608 and 700 cm^{-1} are assigned to cholesterol and difference bands at 1270 and 1660 cm^{-1} to unsaturated fatty acids. Phosphatidycholine, cholesterol and other phospholipids' spectra have been previously described by Krafft et al. [44].

These aggregates of lipids, which are inhomogenously distributed throughout the tissue sections, seem to be a peculiar feature of CCAM. Normal lung tissue did not show their presence even at microscopic imaging. The biochemical information obtained by Raman can be utilized by magnetic resonance (MR) spectroscopy. This modality has previously been used to detect increased contents of lipids and of choline in brain tumors [45] and choline-containing compounds in fetuses in vivo [46]. Based on the current results, MR spectroscopy might also detect these chemical changes in CCAM.

4.4. Lung malformations: Bronchopulmonary sequestrations[4]

Tissue specimens were obtained from two patients with intralobar BPS. Whereas a BPS sample and an additional tissue sample from the BPS macroscopically unaffected margin were obtained from patient 1 (12 months old), only BPS tissue was available for patient 2 (11 years old) because the whole lobe was affected and removed *en bloc*.

Raman spectra were collected at 785 nm laser excitation, by moving the sample with a motorized stage at a step size of 66, 75 or 100 µm.

4.4.1. Pseudo-color Raman maps

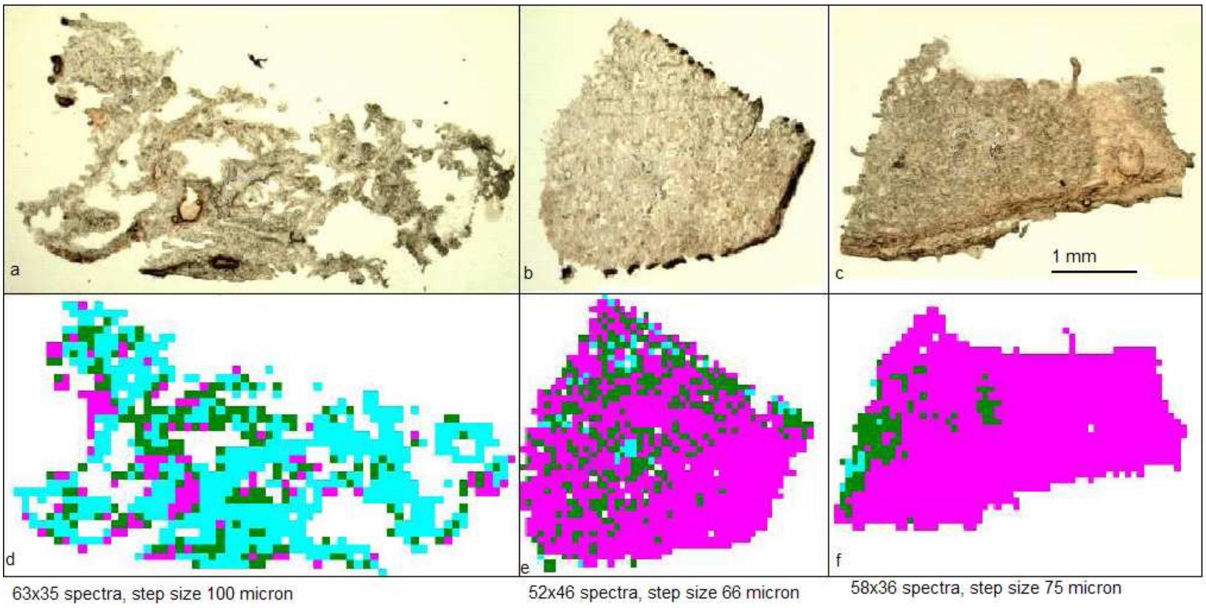

Fig. 28 ***(a, b, c)****: Photographs of native unstained lung tissue from the resection margin of patient 1 (a); from BPS of patient 1 (b); from BPS of patient 2 (c). Black boxes indicate areas of microscopic analyses presented later on in Fig. 29.* ***(d, e, f)****: Pseudo-color Raman maps of the same areas.*

[4] Results and pictures of Raman mapping of BPS have been submitted to the Journal of Biomedical Optics and are currently under revision. *Raman and FTIR Imaging of lung tissue: bronchopulmonary sequestration.* Christoph Krafft, Daniela Codrich, Gloria Pelizzo, Valter Sergo.

The step size was varied in order to obtain similar numbers of spectra per data sets (2205, 2392 and 2088) in spite of different sample areas. After pooling the three Raman images, a cluster analysis was performed in the spectral interval 1190-1750 cm^{-1}. In the Raman image of the marginal tissue sample (Fig. 28d), 64% of spectra were assigned to the cyan cluster, followed by the green cluster (22%) and the magenta cluster (14%). In the Raman images of BPS, most spectra were assigned to magenta clusters (73% in Fig. 28e and 91% in Fig. 28f), followed by green (24% and 8%) and the cyan (3% and 1%) clusters.

In summary, cluster analyses of Raman images gave evidence for two main classes of spectra which represent BPS (magenta) and tissue from BPS margin (cyan cluster).

4.4.2. Average Raman spectra

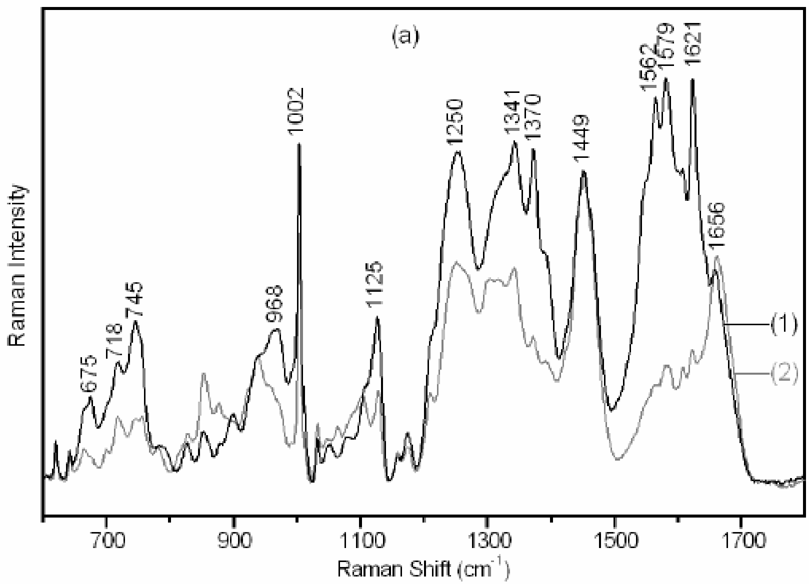

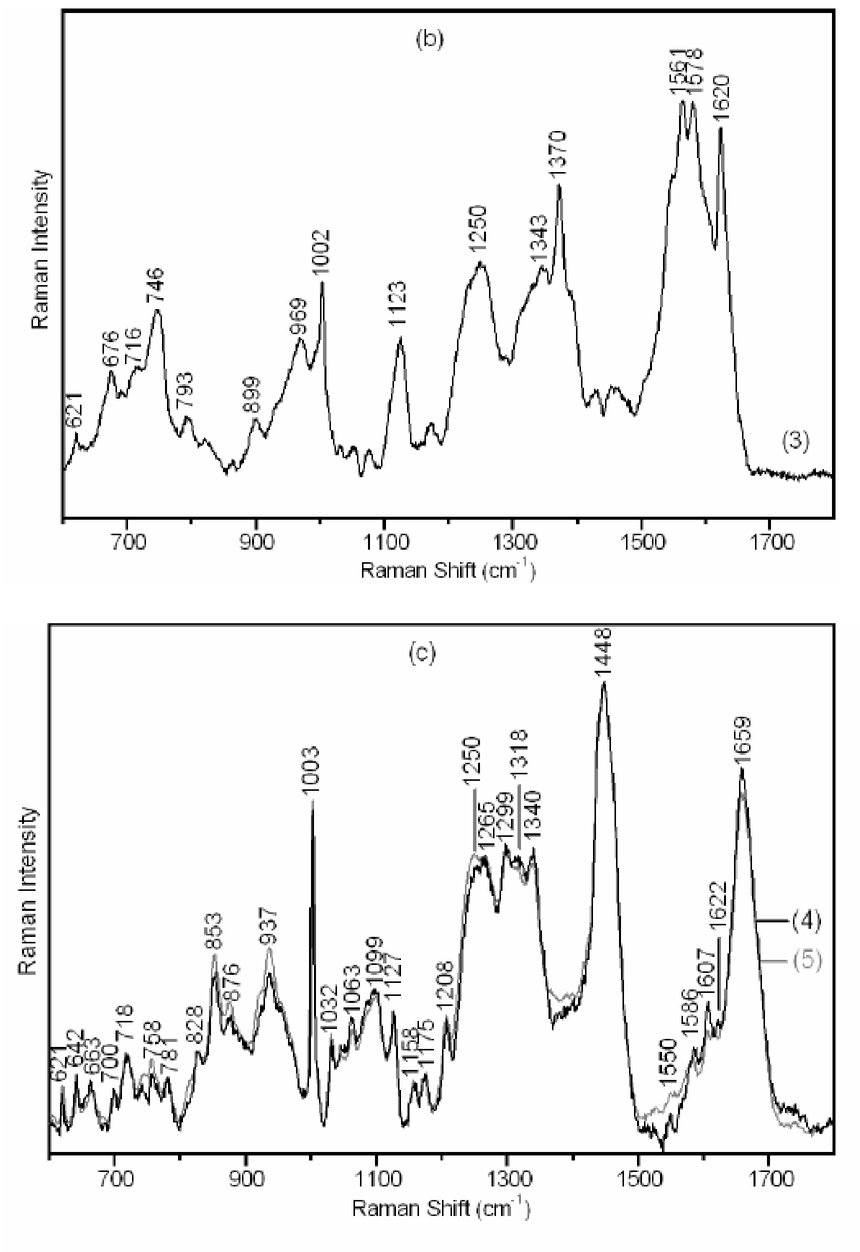

Fig. 29 ***(a)****: Average Raman spectra of BPS and marginal tissue representing the magenta (trace 1) and cyan (trace 2) clusters in Fig. 28 (d, e, f).* ***(b)****: Trace 3 was calculated from the differences of magenta, green and cyan clusters' average spectra and represent hemoglobin.* ***(c)****: Difference spectra calculated as follows: (trace 4)= (1)-(3); (trace 5)= (2)-(3).*

The Raman spectra in Fig. 29a which were averaged from the magenta and the cyan clusters in Figs. 28 (d, e, f) represent BPS (trace 1, black) and the marginal tissue sample (trace 2, gray), respectively. After normalization to equal intensities at 1449 cm^{-1}, numerous bands at 675, 718, 745, 968, 1125, 1250, 1341, 1370, 1562, 1579 and 1621 cm^{-1} were more intense for BPS. These spectral contributions are assigned to hemoglobin which is a major constituent of red blood cells [38,41]. It was described in sections 4.2 and 4.3, how a hemoglobin spectrum can be calculated from the variations of the hemoglobin content within a Raman image. Such a hemoglobin spectrum was included in Fig. 29b. This spectrum was subtracted from the Raman spectra in Fig. 29a in order to compensate the spectral contributions of hemoglobin. The resulting spectra are displayed for BPS (trace 4, black) and the marginal tissue sample (trace 5, gray). More bands are resolved in Fig. 30c which are assigned to lipids (700, 718, 1063, 1127, 1299 cm^{-1}), nucleic acids (663, 781, 1099 cm^{-1}) and proteins. The spectral contributions of proteins can be divided into bands due to phenylalanine (621, 1003, 1032, 1208, 1586 cm^{-1}), tyrosine (642, 828, 853, 1607 cm^{-1}), tryptophan (758, 876, 1550 cm^{-1}), aliphatic amino acids (1318, 1340, 1448 cm^{-1}) and the peptide backbone (937, 1265, 1659 cm^{-1}). After normalization to equal intensities at 1448 cm^{-1} more intense bands at 853, 937 and 1250 cm^{-1} point to higher collagen content in the marginal tissue sample. Other intensity differences between the spectra in Fig. 29c were small and could not be assigned to a component yet.

4.5 Comparison of average Raman spectra from normal, CCAM, BPS and marginal lung tissue

After obtaining average spectra from the most representative clusters of unaffected (red cluster in Figs. 23 (b, d)), CCAM (blue cluster in Figs.24 (b,d)), BPS (magenta cluster in Figs 28 (e, f)) and marginal tissue (cyan cluster in Fig. 28 (d)), we decided to compare them to verify if any similarity existed.

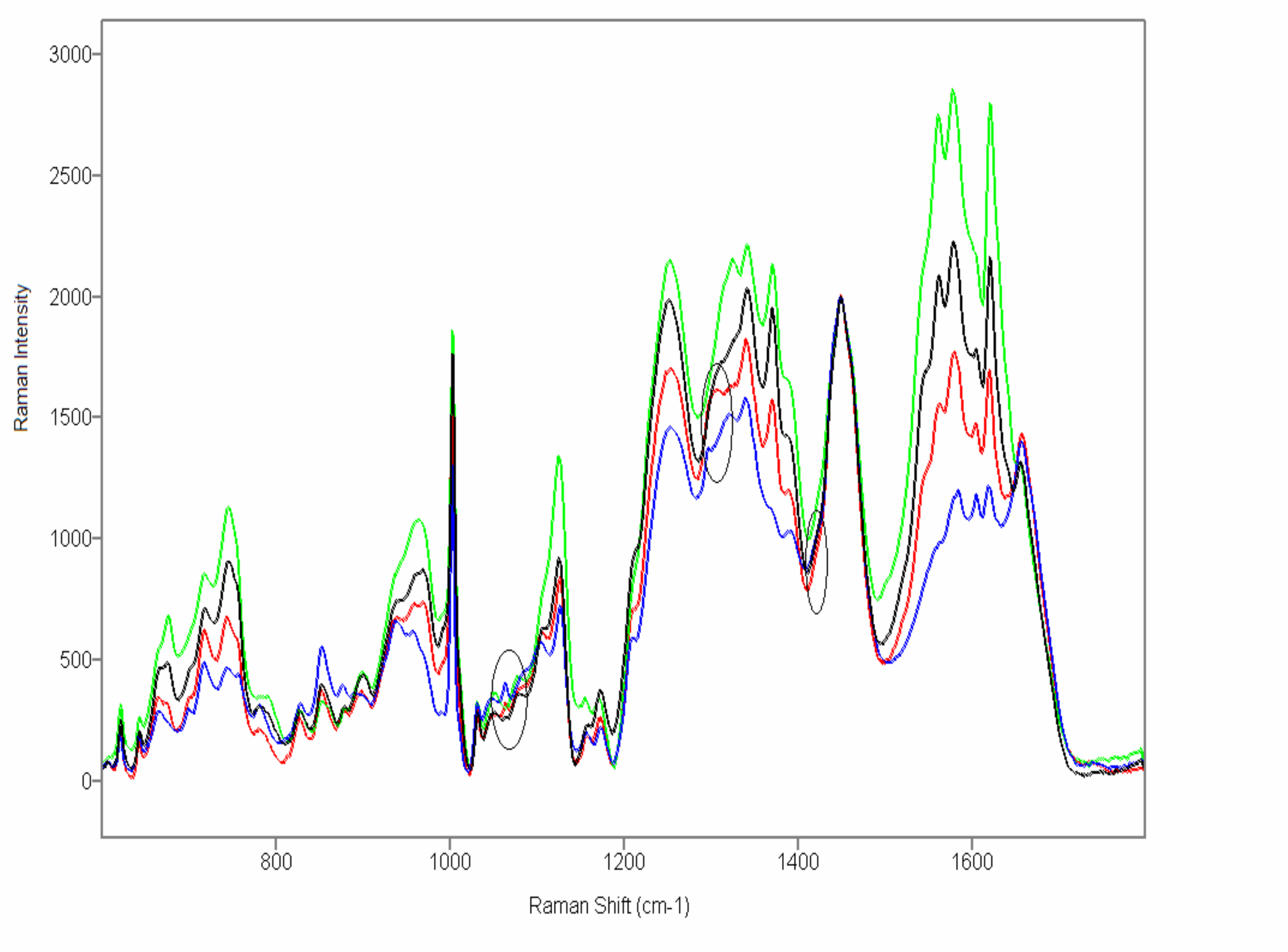

Fig. 30. The four average Raman spectra from 600 to 1800 cm^{-1} from normal lung parenchyma (green trace), sequestration (black trace), CCAM (blue trace) and marginal tissue (red trace) are shown overlaid after normalization at the 1460 cm^{-1} band for comparison.

According to the Raman spectra in Fig. 30, normal lung tissue (green trace) is characterized by intense spectral contributions of hemoglobin and low spectral contributions of other biomolecules such as lipids. The chemical compositions change in BPS and CCAM which is indicated by the Raman spectroscopic fingerprint. The most prominent changes in the Raman spectrum of BPS (black trace) are less intense spectral contributions of hemoglobin. The change in fingerprint seems to be particular successful in case of CCAM (blue trace) because the spectral changes are maximum compared with normal lung tissue and the spectra also differ from the spectra of BPS. At close inspection, band assigned to lipids at 1062, 1301 1442 cm^{-1} are evidenced in blue trace of CCAM and in red from the marginal tissue. These bands, in particular the 1062 and 1442 have been already described as peculiar of the choline aggregates found in the microscopic analysis of CCAM in section 4.3. Also hemoglobin contribution is much lower in the red spectrum than in the normal unaffected lung tissue of green trace. These findings have raised the idea that maybe the tissue from the resection margin was not completely free of disease. Stimulated by our request, the pathologist reviewed the histological sections of the sample and concluded that indeed BPS coexisted with microcystic CCAM and what we called “marginal tissue” was actually a CCAM type 2 area. This possible coexistence of CCAM and BPS has already been reported in section 2.6.

Chapter 5

Comparison of Raman and FTIR data on colon and lung tissue

Theory of Infrared spectroscopy, instrumentation and data acquisition, data processing, results and discussion

The same samples areas that have been submitted to Raman analysis, have been investigated with Fourier Transformed Infra Red (FTIR) spectroscopy, in order to compare the results obtained with two different vibrational spectroscopies. FTIR data have been kindly collected and granted by Prof. Christoph Krafft at Institute for Analytical Chemistry. Since it is not the purpose of the thesis a wide insight and discussion over the applications of FTIR spectroscopy, the introductory part of this chapter will be limited to a brief survey on the theory of IR and only details on instrumentations and data acquisition/processing used in our experiments will be given. IR data will be discussed in comparison with the Raman data for some of the maps presented in chapter 4.

5.1 Basic theory Infra Red (IR) spectroscopy

Infrared (IR) spectroscopy is one of the most common spectroscopic techniques used by organic and inorganic chemists. Simply, it is the absorption measurement of different IR frequencies by a sample positioned in the path of an IR beam. The main goal of IR spectroscopic analysis is to determine the chemical functional groups in the sample.

Infrared radiation spans a section of the electromagnetic spectrum having wavenumbers from roughly 13,000 to 10 cm $^{-1}$, or wavelengths from 0.70 to 1000 μm. It is bound by the red end of the visible region at high frequencies and the microwave region at low frequencies. Photon energies associated with the infrared region of the electromagnetic spectrum are not large enough to excite electrons, but may induce vibrational excitation of covalently bonded atoms and groups. At temperature above absolute zero, all the atoms in molecules are in continuous vibration with respect to each other. When the frequency of a specific vibration is equal to the frequency of the IR radiation directed on the molecule, the molecule absorbs the radiation. IR absorption information is generally presented in the form of a spectrum with wavenumbers at the x-axis and the absorption intensity or % transmittance as the y-axis. Transmittance, T, is the ratio of radiant power transmitted by the sample (I) to the radiant power incident on the sample (I_0). Absorbance (A) is the logarithm to the base 10 of the reciprocal of the transmittance (T).

$$A = \log_{10}\left(\frac{1}{T}\right) = -\log_{10}(T) = -\log 10\left(\frac{I}{I_0}\right) \qquad (1)$$

A molecule absorbs only those frequencies of IR light that match vibrations that cause a change in the dipole moment of the molecule. Bonds in symmetric N_2 and H_2 molecules do not absorb IR because stretching does not change the dipole moment, and bending cannot occur with only 2 atoms in the molecule. Any individual bond in an organic molecule with symmetric structures and identical groups at each end of the bond will not absorb in the IR range. In a complicated molecule many fundamental vibrations are possible, but not all are observed. Some motions do not change the dipole moment for the molecule; some are so much alike that they coalesce into one band (see section 2.3 for comparison with Raman selection rules). Examination of the transmitted light reveals how much energy was absorbed at each wavelength. This can be done with a monochromatic beam, which changes in wavelength over time, or by using a Fourier transform instrument to measure all wavelengths at once. In Fourier transform infrared (FTIR) spectroscopy the IR light is guided through an interferometer. After passing the sample the measured signal is the interferogram. Performing a mathematical Fourier transformation on this signal results in a spectrum identical to that from conventional (dispersive) infrared spectroscopy. Measurement of a single spectrum is faster for the FTIR technique because the information at all frequencies is collected simultaneously. This allows multiple samples to be collected and averaged together resulting in an improvement in sensitivity. Because of its various advantages, virtually all modern infrared spectrometers are FTIR instruments [3,47].

5.2 Samples, instrumentation and data acquisition

The same samples were used for Raman and Infrared analyses, therefore their preparation has already been discussed in section 3.2. For colon samples, FTIR images were recorded using a Bruker FTIR spectrometer Vertex 70 coupled to the microscope Hyperion 3000 which was equipped with a mercury cadmium telluride (MCT) based focal plane array (FPA) detector of 64×64 pixels (Bruker Optik, Germany). The field of view was 170×170 µm per image at 15× magnification and each pixel corresponded to an area of 2.6×2.6 µm. Images of 4096 IR spectra in the wavenumber range 900-3800 cm^{-1} at 4 cm^{-1} spectral resolution were acquired by coadding 25 interferograms using the OPUS software, version 6.0 (Bruker). Mosaics of multiple images were recorded by moving the sampling stage in increments of 170 µm. Acquisition of each image took 70 seconds.

For lung samples , FTIR images were recorded using a Bruker FTIR spectrometer IFS66/S equipped with a mercury cadmium telluride (MCT) focal plane array (FPA) detector of 64×64 pixels (Bruker Optik, Germany). Coupling to the macro chamber IMAC (Bruker) gave a field of view of 4×4 mm^2 and each pixel corresponded to an area of 63×63 μm^2. Using the microscope Hyperion with 15× magnification, the field of view was reduced to 270×270 μm^2 and each pixel corresponded to an area of 4.2×4.2 μm^2. Images of 4096 IR spectra in the wavenumber range 950-3900 cm^{-1} at 4 cm^{-1} spectral resolution were acquired by coadding 11 interferograms. Acquisition of each image took approximately 3 minutes.

5.3 Data processing

As for Raman data sets, FTIR data were imported in the Matlab platform to undergo some preprocessing steps and in Cytospec for further analyses. Preprocessing of the FTIR image involved three steps. First, a multipoint linear baseline was subtracted from each spectrum with baseline points set at minima near 950, 1180, 1480, 1750, 3700 and 3900 cm^{-1}. The baseline segments were obtained by linear interpolation between the selected points. Second, a scaled IR spectrum of water vapor was subtracted from each spectrum to correct spectral contributions of water vapor. Third, spectra with maximum intensities below a threshold were removed from the data sets. Before initialization of the cluster analysis algorithm, the selected spectral range was normalized by the function "multiplicative signal correction" (MSC) in order to separate the chemical information from physical effects, as explained in section 3.5. The preprocessed images were segmented by a k-means cluster analysis (KMC) with a Euclidean distance metric. The averaged spectrum of each cluster was calculated and imported to the program GRAMS (Thermo Fisher, USA) for analysis.

5.4 Results and discussion

5.4.1 Colon[5]

5.4.1.i Pseudo-color FTIR images

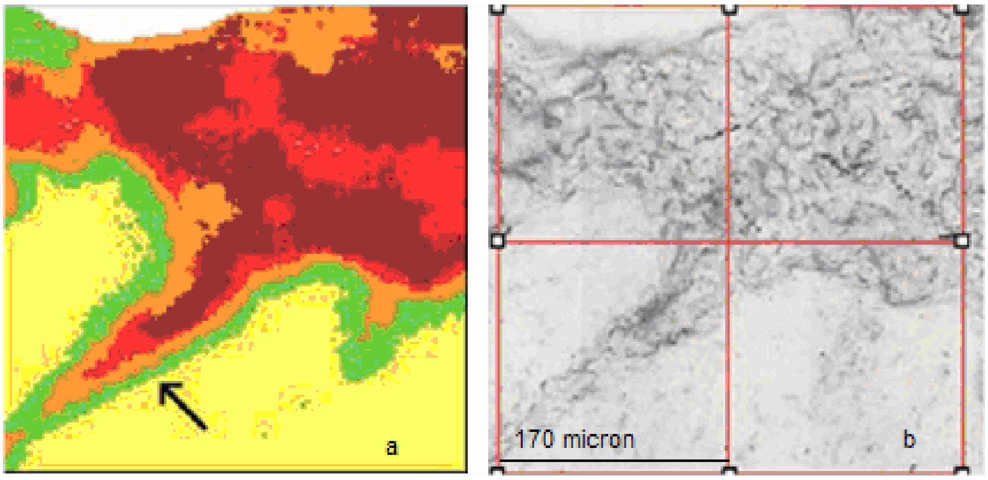

[5] Results and pictures of normal colon FTIR imaging have been accepted for publication in The Journal of Biophotonics: *Raman and FTIR microscopic imaging of colon tissue: a comparative study*. Krafft C, Codrich D, Pelizzo G, Sergo V. **DOI:10.1002/jbio.200710005**.

Fig. 31: 2x2 mosaic pseudo-color FTIR image (a) and photograph of native tissue (b) of area (1) of Fig. 10. Arrow points to a green cluster that has not been evidenced in the corresponding Raman map (see Fig. 11)

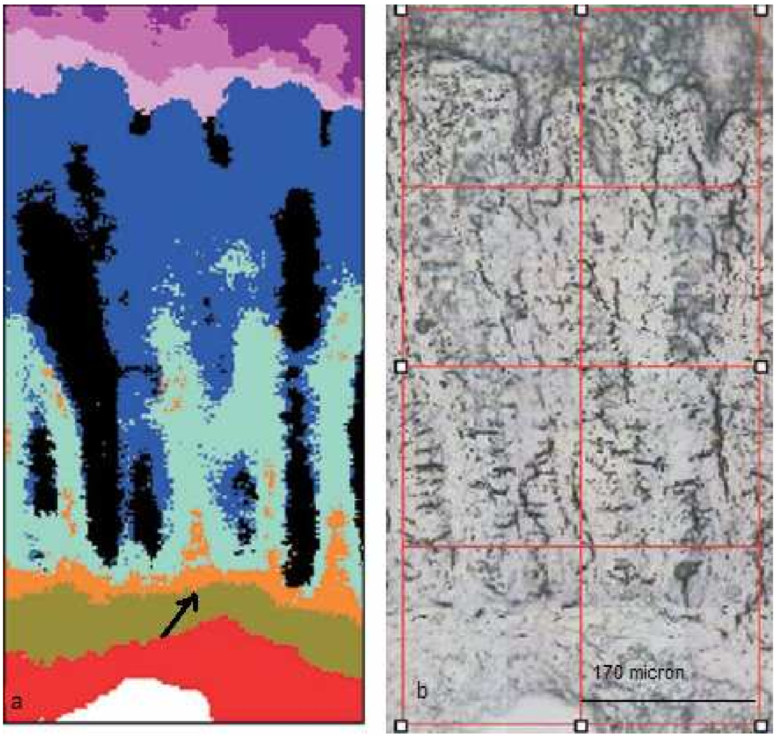

Fig. 32: 2x4 mosaic pseudo-color FTIR image (a) and photograph of native tissue (b) of area (3) of Fig. 10. Arrow points to a cluster that was not evidenced in the corresponding Raman map (see Fig. 11)

Cluster analyses of FTIR images were performed in the interval 1000-1480 cm^{-1} . The FTIR image of area (1) was segmented into five clusters (Fig. 31a). Three clusters (brown, red, orange) were assigned to connective tissue of the submucosa, one cluster to circular muscle (yellow) and one cluster to the transition between smooth muscle and connective tissue (green). The FTIR image of area (3) was segmented by two consecutive cluster analyses (Fig. 32a). The first cluster analysis of all IR spectra separated the clusters of mucus at the top (pink, magenta, violet) and of submucosa (red) and muscularis mucosae (olive) at the bottom from the epithelial tissues. The second cluster analysis segmented the IR spectra of the epithelial fraction into the following four clusters: three clusters of the inner part (cyan, blue, black) and one cluster at the bottom (orange) which is tentatively assigned to lamina propria.

Neither the green cluster in Fig. 31a nor the orange in Fig. 32a have a counterpart in the Raman maps. This can be explained by the fact that all spectroscopy experiments have a diffraction limited lateral resolution [(48)] . The diffraction limit was between 15 and 10 µm for the FTIR system using a Cassegrain objective with NA=0.4 and analyzing the wavenumber range 1000 to 1480 cm^{-1}.[6]. Although each pixel in the FTIR image represents an area of just 2.6×2.6 µm, the pixel contains spectral contributions from neighboring pixels which is a consequence of the diffraction limited lateral resolution. This effect might explain the artifact that additional, continuous clusters were assigned in FTIR images at the transition of two tissue types. The width of these clusters was approximately 10 µm (see arrows in Figs. 2a, d). Such clusters were not evident in the Raman images which were recorded with a step size of 10 µm and in which the diffraction limit using a 785 nm excitation laser and an objective with NA=0.85 was 0.6 µm.

5.4.1.ii IR spectra

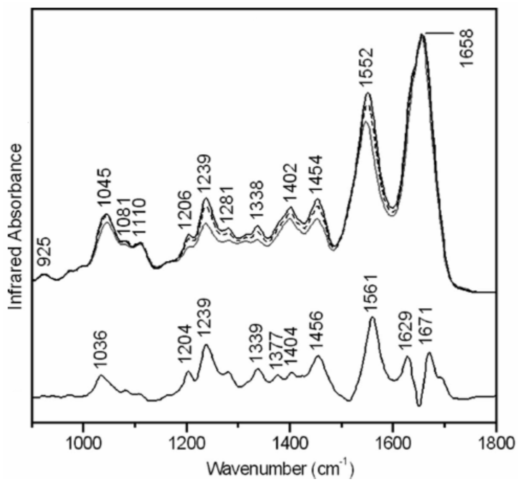

[6] The diffraction limit can be calculated according to Abbe's equation as the quotient 0.612 λ / NA with the wavelength λ and the numerical aperture NA.

Fig.33: IR spectra from 900 to 1800 cm^{-1} of connective tissue representing the brown (solid black), red (dashed) and orange (solid gray) clusters in Fig. 31a. Difference spectra = (solid black) minus (solid gray), displayed at a two fold magnification scale.

IR spectra were offset corrected and normalized to equal intensities of the amide I band at 1658 cm^{-1} for display. Overlay of the IR spectra revealed that the intensities in the interval 1000-1480 cm^{-1} decrease in the order brown>red>orange cluster. Whereas the IR and Raman spectra (see Fig. 16) significantly differ, the difference spectra share a number of similarities which are correlated with the coiled triple helix secondary structure and the unusual amino acid composition of collagen. Positive bands were identified in the Raman and IR difference spectra at the high (1671 cm^{1}) and the low (1629 cm^{-1}) wavenumber shoulder of the amide I band, at the amide III band (1239 cm^{-1}) and CH_3 deformation vibrations (1456 cm^{-1}). The amide II band and its difference band (1561 cm^{-1}) exist only in the IR spectrum. The C-C$_\alpha$ band and its difference band (938 cm^{-1}) are only Raman active. As the spectral range below 900 cm^{-1} could not be registered in the IR spectrum, the bands and its difference bands of proline and hydroxyproline (815, 854 cm^{-1}) were only found in the Raman spectrum.

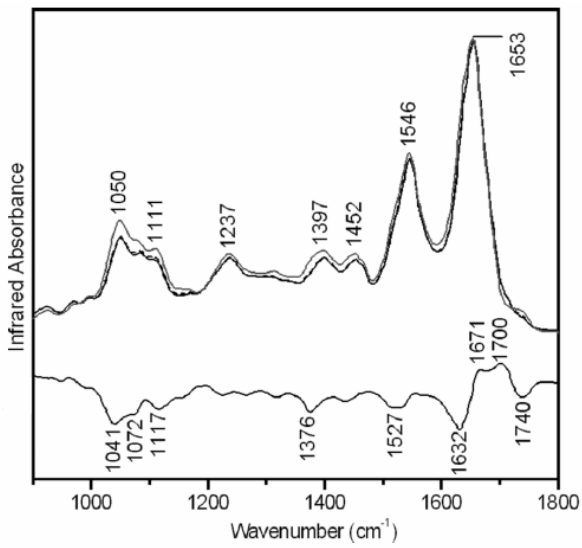

Fig. 34: Average IR spectra from 900 to 1800 cm^{-1} (b) of epithelial tissue representing the cyan (solid black), blue (dashed) and black (solid gray) clusters in Fig. 32a. Difference spectra = (solid black) minus (solid gray). The difference spectrum is displayed at twofold magnified scale.

Overlay of the normalized IR spectra revealed maximum intensities in the interval 1000-1480 cm^{-1} in the black cluster. Negative difference bands are assigned to C-O groups (1041, 1072, 1117 cm^{-1}), C=O groups (1740 cm^{-1}) and peptide groups (1527, 1632 cm^{-1}). These functional groups are consistent with polyglycosylated peptides in mucus which is typically produced by epithelial glands. Bands at similar positions (1044, 1079, 1121, 1373 and 1740 cm^{-1}) were also identified in crypts, which are tubular glands in colorectal mucosa [(22)]. In analogy to the Raman difference spectrum in Fig. 18, positive difference bands are expected to indicate higher DNA content in the cyan cluster. They were found for C=O groups of nucleotides (1700 cm^{-1}), but not for phosphate groups of the backbone near 1085 and 1240 cm^{-1}, which overlap with spectral contributions of secretion products.

Since biomolecules are mainly composed of C, H, O, N and P atoms, IR bands of the main functional groups are broad and most of them are located in a relative small wavenumber interval, the IR spectra of tissue constitute a complex overlap of numerous spectral contributions which are difficult to resolve and complicate to analyze. In order to subtract the constant portion of the spectrum, difference spectra were calculated which enabled inspecting spectral changes more accurately. Nevertheless, although the morphological features in epithelial tissue were well resolved in the FTIR image (Fig. 32), it was problematic to recognize the simultaneous decrease of the DNA content and the increase of the polyglycosylated peptide in the underlying IR spectra. (Fig. 34). Raman bands are usually narrower and they overlap less, in particular in the wavenumber range from 600 to

1000 cm^{-1}. As much as 28 bands were resolved in the Raman spectra of epithelial tissue itself, and further bands were identified in the difference spectrum. Therefore, it was possible to recognize the simultaneous decrease of the DNA content and the increase of the polyglycosilated peptides in the Raman spectra (Fig. 18).

5.4.2 Normal lung[7]

5.4.2.i Pseudo-color IR maps

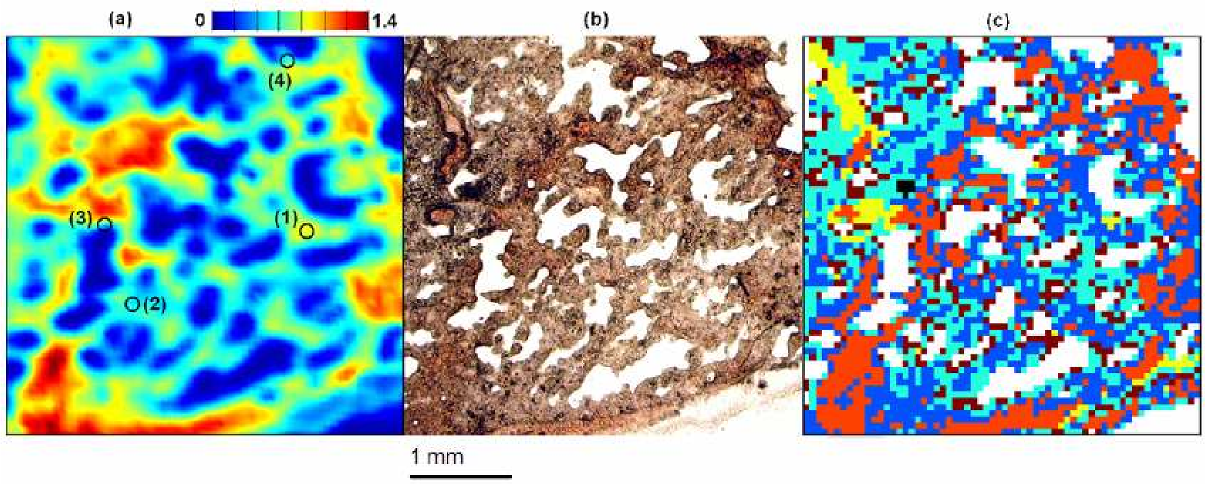

*Fig. 35: Chemical map at 1657 cm^{-1} **(a)**, photograph **(b)** and color coded segmentation by cluster analysis **(c)** of a 64×64 FTIR image obtained from a 4×4 mm^2 lung tissue section. Color code in (c): Lung tissue of high (orange), medium (blue) and low (cyan) content of red blood cells, lung tissue with mucus (black), marginal lung tissue with mucus (brown) and blood vessels (yellow). White regions correspond to spectra which were removed before cluster analysis.*

KMC segmented the FTIR image into five groups of similar IR spectra. White regions represent IR spectra which were removed before KMC because their intensities were below the threshold of 0.15 absorbance units. The majority of spectra were assigned to the orange (21%), blue (34%) and cyan (30%) clusters. The IR spectra (4) of the yellow cluster (4%) mainly correspond to features in the upper left part of the tissue section. The IR spectra (5) of the brown cluster (11%) are found mainly at the tissue margins.

5.4.2.ii IR spectra

[7] Results and pictures of normal lung FTIR mapping have been published in Vibrational Spectroscopy. *Raman and FTIR imaging of lung tissue:methodology for control samples.* C Krafft, D Codrich, G Pelizzo,V Sergo. **46 (2008) 141-149**

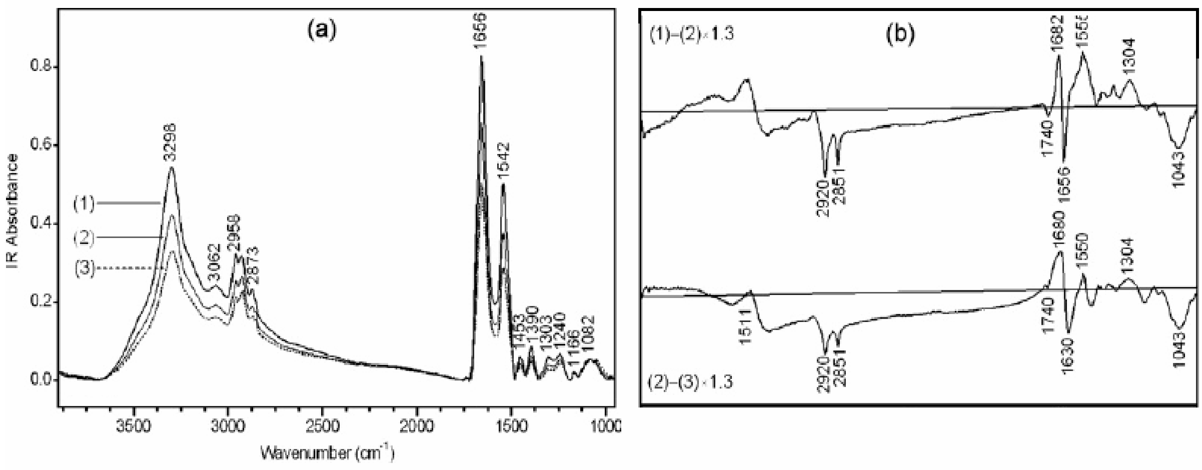

Fig. 36 ***(a)*** *: IR spectra from 3900 to 950 cm^{-1} representing the average of the orange (1), blue (2), cyan (3), clusters of Fig. 35(c). Difference spectra were calculated for comparison* ***(b)****.*

Fig. 36(a) compares IR spectra (1), (2) and (3). Their total intensities decrease in the order 1>2>3. This is consistent with the intensity distribution in Fig. 35(a) because the orange cluster (=spectra (1)) in Fig. 35(c) roughly matches the red and yellow regions in Fig. 35(a), whereas the blue and cyan clusters (=spectra (2) and (3)) correspond to green and cyan regions. Bands can be assigned according to the literature [49] to phosphate groups (1082, 1240 cm^{-1}), to peptide groups (amide III at 1303, amide II at 1542, amide I at 1656, amide B at 3062, amide A at 3298 cm^{-1}) and to aliphatic C-H_2 / C-H_3 groups (1453, 2873, 2958 cm^{-1}) with overlapping contributions form the various biomolecules proteins, lipids, nucleic acids and carbohydrates. Most band positions agree within 1 cm^{-1}. The difference spectra in Fig. 3(b) permit an accurate determination of the spectral changes. Before calculating the difference spectrum, the spectra were normalized to equal amide I intensities near 1656 cm^{-1}. It is remarkable that the normalization factors are 1.3 for both difference spectra showing that the Euclidian distances between the cluster averaged spectra (1), (2) and (3) are equally distributed. As already reported earlier in FTIR images of primary and secondary brain tumors [41], positive difference bands near 1304 and 1555 cm^{-1} in difference spectra (1)-(2) and (2)-(3) indicate an increase of hemorrhage or red blood cells. Negative difference bands at 1043, 1740, 2851 and 2920 cm^{-1} indicate a new tissue component whose concentration increase in the order $1<2<3$. The new component is tentatively assigned to mucus [50] which typically contains bands of C-O groups near 1040 cm^{-1}, C=O groups near 1740 cm^{-1}, and $C\text{-}H_2$ groups near 2851 and 2920 cm^{-1} due to highly glycosilated peptides of its main constituent mucin.In contrast to mucus, spectral contributions of red blood cells were more intense in Raman spectra than in IR spectra due to a resonance effect [38]. This shows that the combined application of Raman and FTIR imaging is particularly useful to study the molecular composition of lung tissue because both methods complement each other.

5.4.3. CCAM[8]

5.4.3.i Pseudo-color IR maps

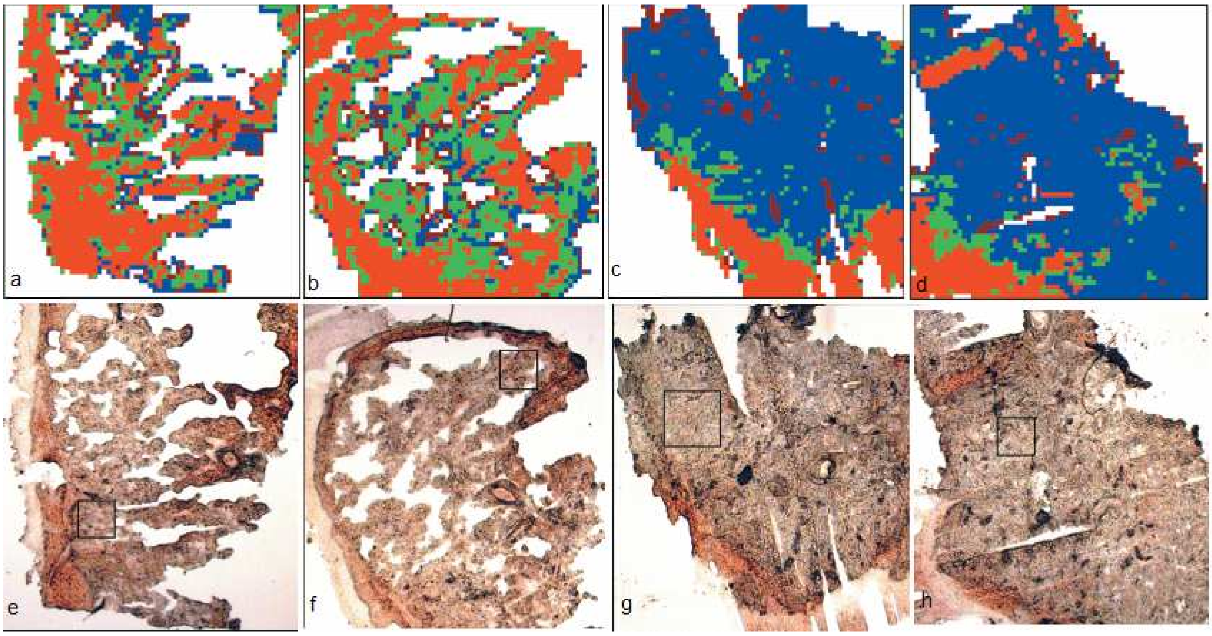

*Fig. 37 FTIR images **(a-d)**, photographs **(e-h)** of lung tissue sections. Data of the first (a, e) and second (b, f) columns were obtained from normal samples of patient 1 and 2, respectively. Data of the third (c, g) and forth (d, h) columns were obtained from CCAM of patient 1 and 2, respectively.*

A cluster analysis of the combined FTIR images was performed in the interval 950-1480 cm^{-1}. The color code in Figs. 37(a-d) represents the segmentation into four classes or clusters. Regions appear white where spectra were removed before at positions without tissue. In Figs. 37 (a) and (b) most spectra were assigned to the red cluster (49% and 46%, respectively), followed by the green cluster (24% and 34%), the blue cluster (19% and 12%) and the brown cluster (7% and 7%). Spectra of the brown cluster are mainly located at the margins. Figs. 1(c) and (d) are dominated by the blue cluster (70% and 74%, respectively).

---

[8] Results and pictures of CCAM FTIR imaging have been published in The Analyst. *Raman mapping and FTIR imaging of lung tissue: congenital cystic adenomatoid malformation*. Krafft C, Codrich D, Pelizzo G, Sergo V. **(2008) 133: 361-371.**

Here, spectra of the red clusters (17% and 15%) are located mainly near the dried liquid film. Spectra of the green clusters (8% and 8%) are found at the transition between the red and the blue clusters. The percentages of the spectra in the brown cluster are reduced to 5% and 3%. In the Raman maps, the brown cluster was not identified (see Figs.23 (b, d) and 24 (b, d)).

5.4.3.ii IR spectra

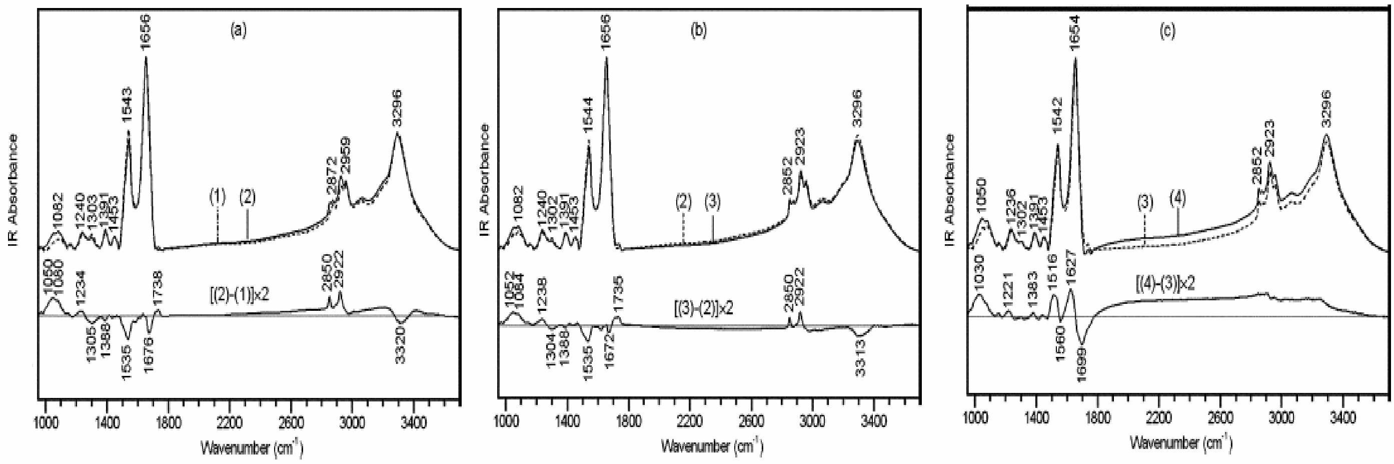

Fig.38: IR spectra from 950 to 3700 cm^{-1} averaged from the red (trace 1), green (trace 2), blue (trace 3) and brown (trace 4) clusters of the FTIR image in Fig. 37(c). Difference spectra were calculated for comparison. Spectra were baseline corrected and normalized for display.

As biomolecules are mainly composed of similar functional groups with C, H, O, N and P atoms and most IR absorption bands are broad, they strongly overlap and it is difficult to resolve each individual band. However, instead of determining the composition or structure of tissues by IR spectra, it is usually sufficient to analyze the spectral changes in most applications. In order to assess the small differences between traces (1) and (2), a difference spectrum was calculated and included in Fig. 38(a) at a two times amplified scale. All positive difference bands at 1050 (vibration of C-O), 1080 and 1234 (symmetric and antisymmetric stretch vibrations of PO_2), 1738 (vibration of C=O), 2850 and 2922 cm^{-1} (symmetric and antisymmetric stretch vibrations of CH_2) are assigned to lipids, in particular phospholipids. All negative difference bands at 1305, 1388, 1535, 1676 and 3320 cm^{-1} are assigned to proteins. In particular, the bands at 1305 and 1535 were reported to correlate with hemoglobin [41, 50].The IR spectra of the green (trace 2) and the blue clusters (trace 3) are overlaid in Fig. 38(b). The band positions largely agree with Fig. 38(a). The difference spectrum between traces (3) and (2) contains the same bands as in Fig. 38(a), however, with slightly different relative intensities. This observation of qualitative similar difference spectra indicates that the lipid content successively increases in the order trace (1)<(2)<(3), whereas the hemoglobin content successively decreases in the order trace (1)>(2)>(3). As the red and green clusters which are represented by traces (1) and (2) are more abundant in FTIR images of normal lung tissue and the blue cluster which is represented by trace (3) is more abundant in FTIR images of CCAM, the total lipid content is higher in CCAM whereas the total hemoglobin content is higher in normal lung tissue.

The IR spectra of the blue (trace 3) and the brown (trace 4) clusters are overlaid in Fig. 38(c). The difference band near 1030 cm^{-1} is assigned to the carbohydrate moiety of mucus [50]. The absence of differences near lipid and hemoglobin bands indicates that these constituents did not change between traces (3) and (4). FTIR imaging was more sensitive to detect lipids and mucus in macroscopic images of CCAM rather than Raman imaging. These components are characterized by a high content of polar C-O, O-H and C-H groups which show usually stronger IR bands than Raman bands. Raman spectroscopy was more sensitive to detect hemoglobin (see section 4.3.2) because Raman spectral contributions of hemoglobin are enhanced by a resonance effect. However, the increase in sensitivity is connected with a decrease in specificity because the enhanced hemoglobin bands partly masked the Raman bands of the other, non-enhanced constituents.

5.4.4 BPS[9]

5.4.4.1. Pseudo-color IR maps

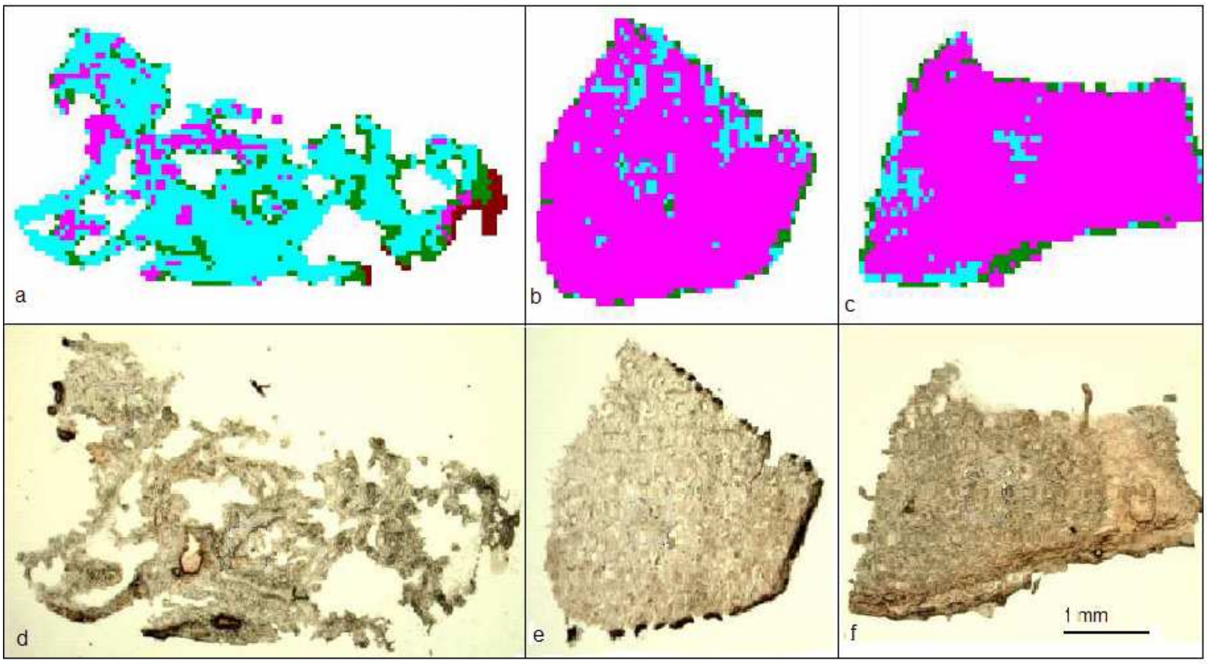

Fig. 39 FTIR images ***(a, b, c)*** *and photographs* ***(d, e, f)*** *of lung tissue. (a, d) were obtained from the resection margin of the BPS sample of patient 1; (b, d) correspond to the BPS of patient 1; (c, f) represent the BPS of patient 2. The color code reflects the segmentation into 4 groups after cluster analysis.*

The FTIR image in Fig. 39(a) was composed of two individual images because the width of the tissue section exceeded the 4×4 mm field of view of the FPA detector. FTIR images in Figs. 39 (b, c) could be assessed by one image each. After pooling the four images, a cluster analysis of the combined data set was performed in the interval 950-1480 cm^{-1}. The color code represents the segmentation into four classes of clusters. Regions appear white where spectra were removed at positions without tissue. In the FTIR image of marginal tissue (Fig.

[9]Results and pictures of Raman mapping of BPS have been submitted to the Journal of Biomedical Optics and are currently under revision. *Raman and FTIR Imaging of lung tissue: bronchopulmonary sequestration***.** Christoph Krafft, Daniela Codrich, Gloria Pelizzo, Valter Sergo.

.

39a), 71% of the spectra were assigned to the cyan cluster. Magenta (15%), green (12%) and brown clusters (2%) were found mainly near the margins. FTIR images of BPS were dominated by magenta clusters (85% in Fig. 39b, and 86% in Fig. 39c). Fewer spectra were assigned to cyan (11 and 8%) and green clusters (4 and 6%), and a brown cluster could not be identified. The brown cluster could not be identified neither in the Raman maps of marginal tissue, nor in the ones of BPS (see Figs. 28 (d, e, f)).

5.4.4.2 IR spectra.

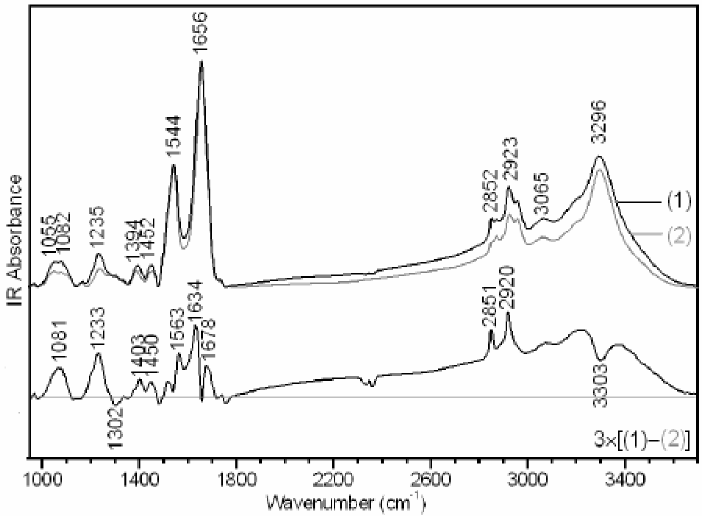

Fig. 40: Average IR spectra of marginal and BPS tissue representing the cyan (trace 1) and magenta (trace 2) clusters in Figs. 39 (a, b, c). The difference spectrum (trace 1 minus trace 2) is displayed at a threefold magnified scale.

The IR spectra were normalized to the amide I band of proteins at 1656 cm^{-1}. Other amide bands are identified at 1235 (amide III), 1544 (amide II), 3065 (amide B) and 3296 cm^{-1} (amide A). The amide bands are due to vibrations of the peptide groups which are present in all proteins. Because the geometry of the peptide groups depends on the secondary structure, these bands are considered as markers for protein structures. Bands at 1394 (COO) and 1452 cm^{-1} (CH_3) are assigned to amino acids side chains. Bands at 1055 (CC and CO), 1082 (PO_2), 1235 (PO_2), 2852 (CH_2) and 2923 cm^{-1} (CH_2) belong to other biomolecules such as lipids and carbohydrates. Bands were assigned according to the literature [49]. The overlay of spectra indicates that some bands are more intense for marginal tissue than for BPS. The difference spectrum at a threefold magnified scale enables to determine the changes more accurately. Whereas the positive difference bands at 1233, 1450 and 1563 cm^{-1} point to an increase of collagen, the positive difference bands at 1081, 1233, 2851 and 2920 cm^{-1} point to an increase of phospholipids in marginal tissue.

5.4.4.2.i Comparison of IR spectra of normal, CCAM, BPS and marginal tissue.

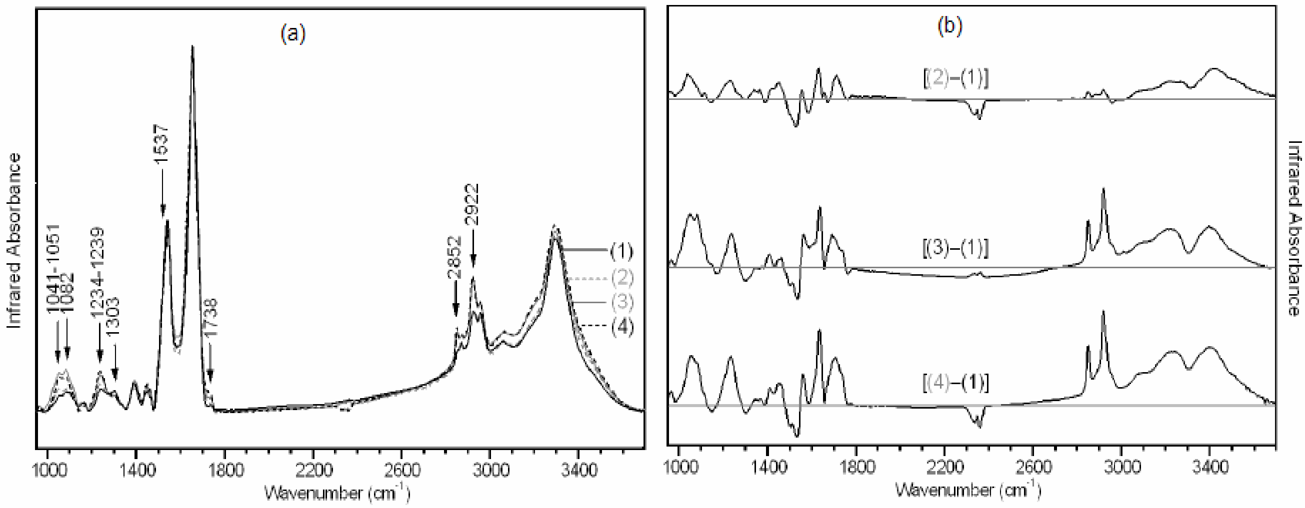

Fig. 41 ***(a)*** *Average IR spectra of normal lung tissue (trace 1), BPS (trace 2), CCAM (trace 3) and marginal tissue (trace 4).* ***(b)****: IR difference spectra for BPS minus normal tissue, CCAM minus normal tissue and the marginal tissue minus normal tissue.*

The IR difference spectrum between trace 2 and 1 in Fig. 41b reveals mainly positive and few negative difference bands after normalization to equal amide 1 intensities. The key marker bands of fatty acids in lipids at 2852 and 2922 cm^{-1} are almost unchanged. Positive difference bands near 1040, 1710 and 3400 cm^{-1} point to constituents with CC, CO and OH functional groups such as carbohydrates. However, the exact band assignment is not important in order to develop supervised, spectroscopy-based classification models. It is more important that the vibrational spectroscopic fingerprints define the specific tissue classes. This seems to be particular successful in case of CCAM (traces 3, gray) because the spectral changes are maximum compared with normal lung tissue and the spectra also differ from the spectra of BPS. The lipid associated bands have highest intensities in the IR spectrum which are indicated by arrows and by positive bands in the difference spectrum. As already noted with the Raman spectra, IR and IR difference spectra of the marginal tissue sample share many similarities with the CCAM spectra: on these bases we prompted a new histopathological evaluation of the sample (see section 4.5).

Chapter 6

Conclusions

Our project has led to a new set-up of the laboratory, switching from inorganic material study, to biological samples, starting a new research field in the Department. Raman has proven to be a valuable tool in analysing human tissue.

Procedures for samples preservation and management have been reviewed from literature and optimized during the studies. Also data processing have been standardized. Raman signals of biological samples are inherently weak without utilizing enhancement effects. Single Raman spectra which were recorded under the applied experimental conditions had typical signal to noise ratios (SNR) of 34 as determined from the band near 1450 cm^{-1} and the baseline corrected standard deviation from 1720 to 1800 cm^{-1}. Multiple Raman spectra of a Raman image were averaged in order to improve SNR up to 850. Before averaging, Raman spectra with similar signatures were identified by k-means cluster analysis combined with a multiplicative signal correction procedure which was able to segment even spectra with low SNR. Even though hierarchical clustering has shown in literature to yield the best segmentation [(22)], k-means clustering has less computational requirements and better suited our large data sets.

The colon tissue has been a good model for soft tissue analyses because it is a stratified tissue and our analysis was able to identify muscular layers, submucosal, epithelial components and neural elements such as ganglia. The latter were analyzed up to a subcellular level, which is a prerequisite for the study of Hirschsprung's disease. Even though a complete and precise assignment of bands to a particular molecular group is not always possible, the most important feature of the vibrational spectroscopies discussed in this thesis is that they define the specific tissue classes by spectral fingerprints.

Also more homogeneous tissues such as lung tissue can be investigated by Raman spectroscopy. Our results permitted to recognize and differentiate normal lung and tissue affected by malformations such as CCAM and BPS. One remarkable result was that our analyses permitted to re-classify a specimen which was considered macroscopically normal (the marginal tissue) as a pathological area of CCAM type 2. This is an example of the advantage of knowing the molecular composition of a tissue, besides its morphological appearance: these information are not dependent from the eye and experience of the pathologists. However, in this study almost only intra-sample spectral variance has been investigated, validation of inter-samples variances recognition requires more samples.

As far as comparison between Raman and FTIR spectroscopy is concerned, FTIR images have the advantage of shorter acquisition times: data acquisition by FTIR imaging is more rapid and yields spectra with higher signal noise ratios because the tissue sections are globally illuminated and the spectra are registered in parallel by a multichannel detector. In contrast, the laser is focused onto a small spot in Raman mapping and the spectra are sequentially registered, which is a more time-consuming procedure. Total acquisition time in Raman mapping is determined by the product of the number of spectra and the time per spectrum. However, lateral and spectral resolutions of FTIR are inferior to Raman. Water is also very IR-active and this could be a problem in examining fresh (and not dried) tissue. Some moieties are better recognized by IR (lipids and mucus and other components which are characterized by a high content of polar C-O, O-H and C-H groups that show stronger IR bands than Raman bands) and other are better evidenced by Raman, i.e. hemoglobin, DNA, the phosphate groups in phospholipids. In the lung section, we suggested a method to compensate the enhanced Raman signal of hemoglobin which masks other molecular groups.

Altogether, Raman and FTIR spectroscopies seem to be complementary techniques rather than alternatives. We also demonstrated that vibrational spectroscopies are able to distinguish not only neoplastic and normal tissue, but also normal and malformed tissue.

Although our study, as the majority of studies on the application of Raman spectroscopy for the investigation of tissues are exploratory in nature, the clear message is that clinical diagnostic tools might be successfully developed from the spectroscopic fingerprint of tissues. However, before a clinical diagnostic application of Raman spectroscopy can be imagined, a comprehensive spectral database containing Raman spectra of tissue that are labeled by histology (still the gold standard up to now) must be created. If the aim is to distinguish for example between healthy tissue and grades of disease, the database should represent the variance in the molecular composition of tissue within each classification group. The database can then be used in combination with multivariate statistical analyses and/or artificial neural network analyses to construct automated pattern recognition algorithms for the non subjective discrimination of the different tissue types.

Another issue for future applications of Raman spectroscopy to clinical in vivo diagnostic problem is the development of appropriate fiber optic devices. Koljenovic(17) suggested the use of an unfiltered fiber-optic probe and collection of spectral information in the high-wavenumber region from 2400 to 3800 cm^{-1} because the core material low OH silica shows only low spectral contributions in that region, but recently this approach has been questioned in another paper, in which for the first time a Raman map from brain tissue was collected using a filtered fiber-optic probe by Inphotonics™ connected to a spectroghraph.(51) Quite encouraging results have been obtained in the latter paper.

Therefore, other steps must be taken before Raman spectroscopy can be proposed to clinicians. An important requisite for success is that it should be doctor and patient friendly and yield answers (yes/no) instead of spectra. Once the technology will be in place, clinical trials will be required to explore the potential of the technique.

References

1. Turrel G, Corset J. *Raman microscopy. Developments and applications*. 1996. Academic Press. ISBN 0-12-189690-0.

2. Ferraro JR, Nakamoto K,Brown CW. Chapter 1 and Chapter 2. In *Introductory Raman Spectroscopy*, second edition. 1994. Elsevier Science. ISBN 0-12-254105-7.

3. Siebert F, Hildebrandt P. Chapter 1. In *Vibrational spectroscopy in life science*. 2008 Wiley-VCH. ISBN 978-3-527-40506-0.

4. O'Neill JA, Rowe MI, Grosfeld JL, Fonkalsrud EW, Coran AG. Chapter 94. In *Pediatric Surgery*. Fifth Edition, Mosby, 1998. ISBN 0-8151-6518-8.

5. Rolle U, Piaseczna Piotrowska A, Nemeth L, Puri P. *Altered distribution of Interstitial Cells of Cajal in Hirschsprung disease*. Arch Pathol Lab Med. 126:928-933, 2002.

6. Dasgupta R, Langer JC. *Hirschsprung disease*. Current Probl Surg. 41:949-988, 2004.

7. Moore SW, Johnson G. *Acetylcholinesterase in Hirschsprung disease*. Ped Surg Int. 21:255-263, 2005.

8. Mendeloff EN. *Sequestration, Congenital Cystic adenomatoid malformations and Congenital Lobar Emphysema*. Semin Thoracic Cardiovasc Surg, 16:209-214, 2004

9. Langston C. *New concepts in the pathology of Congenital Lung Malformations*. Semin Ped Surg, 12(1):17-37, 2003.

10. Laberge JM, Bratu I, Flageole H. *The management of asymptomatic congenital lung malformations.* Ped Res Rev, 5(suppA): S305-S312, 2004.

11. Bush A. *Congenital Lung Disease: a plea for clear thinking and clear nomenclature*. Pediatr Pulmon, 32:328-337, 2001.

12. Davenport M, Warne SA, Cacciaguerra S, Patel S, Greenough A, Nicolaides K. *Current outcome of antenatally diagnosed cystic lung disease*. J Ped Surg, 39:549-556, 2004.

13. Calvert JK, Lakhoo K, *Antenatally suspected congenital cystic adenomatoid malformation of the lung: postnatal investigation and timing of surgery*. J Ped Surg, 42: 411-414, 2007.

14. Choo-Smith LP, Edwards HGM, Endtz HP, Kros JM, Heule F, Barr H, Robinson JS, Bruining HA, Puppels GJ. *Medical application of Raman spectroscopy: from proof of principle to clinical implementation.* Biopolymers, 67:1-9, 2002.

15. Owen CA, Notingher I, Hill R, Stevens M, Hench LL. *Progress in Raman spectroscopy in the fields of tissue engineering, diagnostics and toxicological testing.* J Mater Sci, 17: 1019-1023, 2006.

16. C. Krafft and V. Sergo, *Biomedical applications of Raman and infrared spectroscopy to diagnose tissue,* Spectrosc. Int. J. vol 20(5-6), 195-218, 2006.

17. Koljenovic S, Bakker Shut TC, Wolthius R, de Jong B, Santos L, Casper PJ, Kros JM, Puppels GJ. *Tissue characterization using high wave number Raman spectroscopy*. J Biomed Optics, 10(3):031116 , 2005.

18. Motz JT, Gandhi SJ, Scepanovic OR, Haka AS, Kramer JR, Dasari RR, Feld MS. *Real time Raman system for in vivo disease diagnosis*. J. Biomed. Optics 10, 031113, 2005.

19. Buschmann HP, Marple ET, Wach ML, Bennet B, Bakker Schut TC, Bruining HA, Bruschke AV, van der Laarse A, Puppels GJ. *In vivo determination of the molecular composition of artery wall by intravascular Raman spectroscopy*. Anal. Chem. 72: 3771-3775, 2000.

20. Boere IA, Bakker Schut TC, van den Boogert J, de Bruin RWF , Puppels GJ. *Use of fibre optic probes for detection of Barrett's epithelium in the rat oesophagus by Raman spectroscopy.* Vib. Spectrosc. 32: 47-55, 2003.

21. Wang TD, Van Dam J. *Optical biopsy: a new frontier in endoscopic detection and diagnosis*. Clin Gastroenterol Hepatol , 2(9):744-753, 2004.

22. Lasch P, Haensch W, Naumann D, Diem M. *Imaging of colorectal adenocarcinoma using*

FTIR microspectroscopy and cluster analysis. Biochim. Biophys. Acta 1688: 176-186, 2004.

23. Andrade PO, Bitar RA, Yassoyama K, Martino H, Santo AME, Bruno PM, Martin AA, *Study of normal colorectal tissue by FT-Raman spectroscopy*. Anal Bioanal Chem. 387(5):1643-8, 2007.

24. Shim MG, Wong Kee Song LM, Marcon NE and Wilson BC. *In vivo near-infrared Raman spectroscopy: demonstration of feasibility during clinical gastrointestinal endoscopy*. Photochem. Photobiol. (72) 146-150, 2000.

25. Molckovsky A, Wong Kee Song LM, Shim MG, Marcon NE, Wilson BC. *Diagnostic potential of near-infrared Raman spectroscopy in the colon: differentiating adenomatous from hyperplastic polyps*. Gastrointest. Endosc. 57:396-402, 2003.

26. Stone N, Kendall C, Smith J, Crow P. Barr H. *Raman spectroscopy for identification of epithelial cancers*. Faraday Discuss., 126:141-157, 2004.

27. Huang Z., McWilliams A., Lur H., McLean D.I., Lam and H. Zeng S. *Near infrared Raman spectroscopy for optical diagnosis of lung cancer*. Int. J. Cancer 107:1047-1052, 2003.

28. Yamazaki H, Kaminaka S, Kohda E, Mukai M, Hamaguchi H. *The diagnosis of lung cancer using 1064-nm excited near infrared multichannel Raman spectroscopy*. Radiation Med. 21(1):1-6, 2003

29. Koljenovic S., Bakker Schut T.C., van Meerbeeck J.P., Maat A.P., Burgers S.A., Zondervan P.E., Kros J.M., Puppels G.J. *Raman microspectroscopic mapping studies of human bronchial tissue*. J. Biomed. Opt. 9:1187-1197, 2004.

30. Krishna CM, Sockalingum GD, Venteo L, Bhat RA, Kushtagi P, Pluot M, Manfait M. *Evaluation of the suitability of ex vivo handled ovarian tissues for optical diagnosis by Raman microspectroscopy*. Biopolymers, 79:269-276, 2005.

31. Krishna CM, Sockalingum GD,Vadhiraja BM, Maheedhar K, Rao ACK, Venteo L, Pluot

M, Fernandes DJ, Vidyasagar MS, Kartha VB, Manfait M. *Vibrational spectroscopy studies of formalin –fixed cervix tissue.* Biopolymers, 85:214-221, 2007.

32.Huang Z, McWilliams A, Lam S, English J, McLean DI, Lui H, Zeng H. *Effect of formalin fixation on the near-infrared Raman spectroscopy of normal and cancerous human bronchial tissue*. Int J Oncol, 23:649-655, 2003.

33. Cytospec website: http://www.cytospec.com

34. Martens H, Pram Nielsen J, Balling Engelsen S. *Light scattering and light Absorbance separated by extended multiplicative signal correction. Application to near-infrared transmission analysis of powder mixtures.* Anal Chem, 75:394-404, 2003.

35.Chen ZP, Morris J, Martin E. *Extracting chemical information from spectral data with multiplicative light scattering effects by optical path-length estimation and correction.* Anal Chem 78:7674-7681,2006.

36. Lasch P, Haensch W, Naumann D, Diem M. *Imaging of colorectal adenocarcinoma using FT-IR microspectroscopy and cluster analysis.* Bioch Bioph Acta 1688:176-186, 2004.

37. McQueen, JB. *Some methods of classification and analysis of multivariate observations*. In LeCam LM, Neymann J (Eds). Proceedings of Fifth Berkley Symposiun on mathematical statistics and probability, University of California, Berkeley, pp.281-297, 1967.

38. Wood BR, Caspers P, Puppels GJ, Pandiancherri S, McNaughton D. *Resonance Raman spectroscopy of red blood cells using near infra-red laser excitation.* Anal Bioanal Chem 387:1691-1703, 2007.

39. Peticolas WL. *Raman spectroscopy of DNA and proteins*.Methods Enzymol 246: 389-416, 1995.

40. Krafft C, Knetschke T, Siegner A, Funk RHW, Salzer R. *Mapping of single cells by near infrared Raman microspectroscopy*. Vib Spectrosc 32: 75-83, 2003.

41. Krafft C, Sobottka SB, Schackert G, Salzer R. *Raman and infrared spectroscopic mapping of human primary intracranial tumors: a comparative study*. J Raman Spectrosc 37: 367-375, 2006.

42. Madsen PL, Secher NH. *Near-infrared oximetry of the brain*. Prog Neurobiol 58:541-560, 1999.

43. Reich G. *Near-infrared spectroscopy and imaging: basic principles and pharmaceutical applications.* Adv Drug Deliv Rev. 57: 1109-1143, 2005.

44. Krafft C, Neudert L, Simat T, Valzer R. *Near infrared Raman spectra of human brain lipids.* Spectrochim. Acta A, 61:1529-1535, 2005.

45. Sijens PE, Levendag PC, Vecht CJ, van Dijk P, OudkerkM. *1H MR spectroscopy detection of lipids and lactate in metastatic brain tumors.* NMR Biomed. 9: 65–71, 1996.

46. Clifton MS, Joe BN, Zektzer AS, Kurhanewicz J, Vigneron DB, Coakley FV, Nobuhara KK, Swanson MG. *Feasibility of magnetic resonance spectroscopy for evaluating fetal lung maturity*. J Ped Surg, 41(4): 768-773, 2006.

47. Sherman Hsu CP. Infra Red spectroscopy. In Handbook of instrumental techniques for analytical chemistry. Chapter 15. F. Settle Editor, Prentice Hall Inc., pp 247-283, 1997.

48. Lasch P, Naumann D. *Spatial resolution in infrared microspectroscopic imaging of tissues*. Biochim Biophys Acta 1758: 814-829, 2006.

49. Naumann D. *Infrared spectroscopy in microbiology*. In: Encyclopedia of Analytical Chemistry. R.A. Meyers (Ed.) John Wiley and Sons, Chichester ,pp. 102-131, 2000.

50. Chiriboga L, Xie P, Vigorita V, Zarou D, Zakim D, Diem M. *Infrared spectroscopy of human tissue. II. A comparative study of spectra of biopsies of cervical squamous epithelium and of exfoliated cervical cells.*Biospectrosc, 4: 55-59, 1998.

51. Krafft C, Kirsch M, Beleites C, Schackert G, Salzer R. *Methodology for fiber-optic Raman mapping and FTIR imaging of metastases in mouse brains.* Anal Bioanal Chem, 389:1133-1142, 2007.

52. Stone N, Kendall C, Smith J, Crow P, Barr H. *Raman spectroscopy for identification of epithelial cancers*. Faraday Discuss, 126:141-157, 2004.

Appendix

MAJOR ASSIGNMENTS OF RAMAN BANDS [52]	
Peak position/cm^{-1}	*Assignment*
621	C-C twisting mode of Phenylalanine
643	C-C twisting mode of Thyrosine
669	C-S stretching mode of Cystine
679	Guanine ring breathing
700	Cholesterol
717-719	Phospholipids head/adenine
747	Haemoglobin
755	Symmetric breathing of Tryptophan
759	Tryptophan
781	Cytosine/uracile ring breathing
786	DNA: O-P-O , cytosine, uracile, thimine
826	DNA: O-P-O stretch
853	Ring breathing mode of thyrosine and C-C stretch of proline ring/collagen
859	Thyrosine/collagen
869	Proline
876	Hydroxyproline, collagene
920	C-C stretch of proline
935	C-C stretch of proline and valine, α-helix conformation of protein backbone
938	C-C stretch of protein backbone
1001-1004	Symmetric ring breathing mode of phenylalanine
1031	C-H in-plane bending mode of phenylalanine
1062-1064	Skeletal C-C stretch lipids
1078	C-C or C-O stretch (lipids), C-C or PO_2 stretch 8nucleic acids)
1083	C-N stretching mode of proteins (and lipid mode to lesser degree)
1087-1090	C-C stretch, O-P-O stretch
1117-1119	C-C stretch
1123	C-C stretching mode of lipids/proteins, C-N stretch/ glucose
1155	C-C (& C-N) stretching of proteins
1170	C-H in-plane bending mode of tyrosine
1180-1184	Cytosine, guanine, adenine
1206	Hydroxyproline, tyrosine
1209	Trypthophan and phenylalanine
1220-1221	Amide III: β-sheet
1243	Amide III: collagene (CH_2 wag, C-N stretch)
1258	Amide III/ adenine/cytosine
1260	Amide III
1264	-C-H in-plane bending (lipid)
1240-1265	Amide III (C-N stretching mode of proteins, indicating mainly α-helix conformation)
1279	Amide III: α-helix
1299-1300	CH_2 deformation (lipids)
1302-1304	CH_2 deformation (lipids-phospholipids)/ adenine, cytosine

CONTINUED	
1313	CH_3CH_2 twisting mode of collagene/lipids
1335-1345	CH_3CH_2 wagging mode of collagene
1336	Polynucleotide chain (DNA-purine bases)
1369	Guanine, porphyrins (haemoglobin), lipids
1386	CH_3 bend
1437	CH_2 deformation (lipids), cholesterol
1443	CH_2 deformation (lipids and proteins)
1446	CH_2 bending mode of proteins
1485	Nucleic acids purine bases (guanine and adenine)
1520-1538	-C-C- carotenoid
1548	Tryptophan
1560	Hemoglobin
1573	Guanine, adenine
1577-1579	Pyrimiine ring (nucleic acids) and heme proteins (haemoglobin)
1603	C-C in plane bending mode of phenylalanine and tyrosine
1616	C-C stretching mode of tyrosine and tryptophan
1638	Intermolecular bending mode of water
1645	Amide I: α-helix
1652-1653	Lipid (C-C stretch)
1654-1655	Amide I (C-O stretching mode of proteins, α-helix conformation)/ C-C lipid stretch
1738-1746	C-O stretch (lipids)

MAJOR ASSIGNMENTS OF INFRARED BANDS [49,50]	
Peak/ cm^{-1}	*Assignment*
969	Phosphatidylcholine
1026	glycogen
1030	mucus
1060	Glycolipids (stretching mode C-O-C), cholesterol
1080	O-P-O stretching mode, phospholipids, glycogen
1153	glycogen
1234	O-P-O stretching mode, phospholipids, collagen
1303	Amide III: proteins
1391	O-C-O stretching mode, proteins, cholesterol
1453	CH_3 deformation, proteins, collagen
1467	CH_2 deformation, lipids
1543	Amide II: proteins
1656	Amide I: proteins
1738	C=O stretching mode, lipids
2850	CH_2 stretching, lipid
2872	CH_3 stretching, proteins
2922	CH_2 stretching, lipid
2959	CH_3 stretching, proteins
3296	Amide A, proteins